Neutron and X-Ray Diffraction of Glass

Laurent Cormier

Neutron and x-ray diffraction

Laurent Cormier

Author portrait Laurent CORMIER

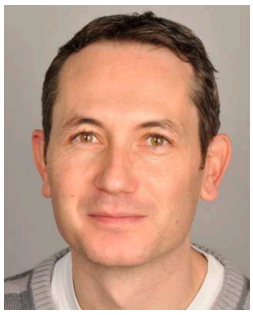

Laurent Cormier obtained his PhD from the University Pierre and Marie Curie – Paris 6 (France) in 1997 and worked at the Cavendish Laboratory, Cambridge University (UK). He enters at CNRS in 1999. His research focuses on understanding the glass structure at short and medium range order in relation with transport, nucleation and crystallization properties, using experimental and modelling techniques. He received the Gottardi prize by the ICG.

Please supply the link to your personal homepage:

http://www.impmc.upmc.fr/~cormier

Your work/ affiliation address: Institute of Mineralogy, Materials Physics and Cosmochemistry

Title(s): Dr.

First and last name: Laurent CORMIER

University/Company: Sorbonne University

Street & number /P.O.Box: 4 place Jussieu

City & ZIP: 75005 Paris

Country: France

Telephone: +33143275239

E-Mail: Laurent.cormier@ upmc.fr

Table of contents

Abstract

A basic characterization of amorphous materials is usually obtained using diffraction measurements. Indeed, amorphicity is revealed by the absence of sharp Bragg peaks in the angular diffraction pattern, signaling the lack of long-range order and periodicity. However, diffraction patterns obtained by scattering from x-rays, electrons or neutrons contain much more structural information, often overlooked, about the atomic organization of disordered materials. x-ray and neutron diffraction are pioneering tools to get information on the atomic arrangements of non-crystalline materials and, still the earlier x-ray diffraction investigations [1][2][3], are still routinely used structural experimental techniques.

The success of diffraction methods is partly due to the fact that they give the most direct access to the atomic structure; in particular interatomic distances and coordination numbers, and diffraction data can be easily compared to simulations, which is widely used to validate interatomic potentials in Molecular Dynamics. Another advantage of this technique is to probe both the short and intermediate range order, being very sensitive to the nature and extent of disorder in glasses and liquids and an essential probe to understand the structural differences between glasses and their crystalline counterparts. Finally, various environments have been developed allowing high temperature and/or high pressure measurements to be carried out.

1. Diffraction by non-crystalline materials

1.1 Scattering of neutrons and x-ray

The fundamental aspects of the scattering processes have been completely described elsewhere [4][5][6][7] and we will propose only a brief outline of the theory.

In a conventional diffraction experiments (figure 1.a), the quantity measured by the detector into the small solid angle $d\Omega$ at the scattering angle 2θ is the *differential cross section* $d\sigma/d\Omega$ (in barns/steradian), defined as:

$$\frac{1}{N}\frac{d\sigma}{d\Omega} = \frac{number\ \ of\ \ quanta\ \ of\ \ wavelength\ \ \lambda\ \ scattered\ \ per\ \ unit\ \ time\ \ \mathrm{int}o\ \ d\Omega}{N\Phi(\lambda)d\Omega} = I(Q) \qquad (1)$$

with N the number of scattering units in the sample and $\Phi(\lambda)$ the incident flux of quanta at wavelength λ. Q (in $Å^{-1}$) is the magnitude of the *scattering vector* (figure 1.b) for an elastic scattering, *i.e.* $k_i = k_f$ (or in the static approximation, $k_i \approx k_f$, see below):

$$Q = \frac{4\pi \sin\theta}{\lambda} \qquad (2).$$

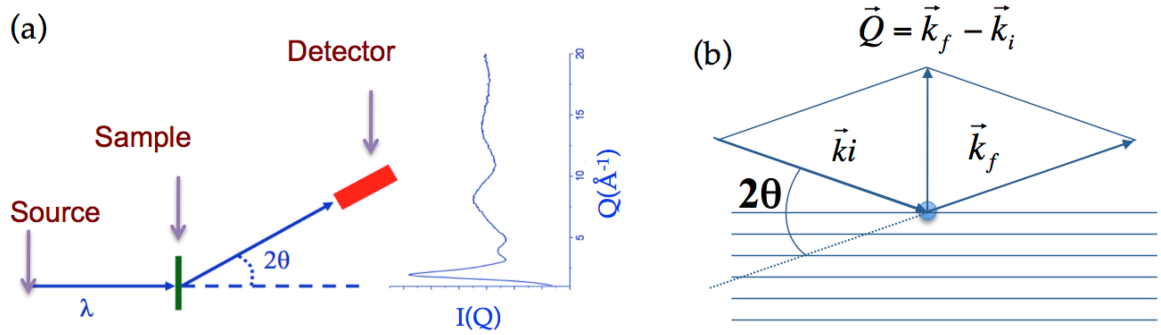

Figure 1: *(a) Conventional setup for a diffraction experiment. A monochromator can be placed between the source and sample, which is the case for synchrotrons or steady state reactors. To obtain true elastic scattering, a monochromator should also be placed between the sample and the detector. (b) Scattering from a single atom by an incoming radiation with wavevector* $\mathbf{k}_i$ *of magnitude* $2\pi/\lambda$*, and a scattered wavevector* $\mathbf{k}_f$*.*

The differential cross-section may be separated as a 'distinct' term and a 'self' term [8]:

$$I(Q) = F(Q) + \sum_{\alpha}^{n} c_\alpha \overline{b_\alpha^2} \qquad (3)$$

with $F(Q)$ the *total interference function,* c_α and b_α are the atomic concentration and scattering length of the chemical species α, respectively. The *neutron scattering length*, b, measured the strength of the interaction between the neutron and the nucleus, can be positive or negative and is expressed in fm (10^{-15} m). All the structural information is contained in the interference function that is simply related to a *structure factor* $S(Q)$ by the relation:

$$S(Q) = \frac{F(Q)}{\left(\sum_{\alpha} c_\alpha b_\alpha\right)^2} + 1 = \frac{F(Q)}{\overline{b}^2} + 1 \qquad (4)$$

with $S(Q \rightarrow \infty) = 1$ and $S(Q) \geq 0$.

The Fourier transform of the structure factor gives a *pair distribution (correlation) function,* $g(r)$, describing interatomic interactions in real space [5]:

$$g(r) - 1 = \frac{1}{2\pi^2 r \rho_0} \int_0^\infty Q\big(S(Q) - 1\big)\sin(Qr)\,dQ \qquad (5)$$

where r is the interatomic distance, ρ_0 (atoms Å^{-3}) is the *atomic number density* expressed as a function of the macroscopic density, d (g cm^{-3}):

$$\rho_0 = \frac{N_A d}{A \ 10^{24}} \tag{6}$$

N_A being the Avogadro number and A the atomic weight of the sample.

1.2 The static approximation

In a diffraction experiment, the x-ray or neutron is usually detected without a monochromator being placed between the sample and the detector. In such a case, the experiment is not exactly elastic (as it would be if $k_i = k_f$ in figure 1.b) and energy exchange could occur within the sample due to interactions of neutrons or x-ray photons with thermal vibrations. The static approximation consider that such energy transfers is negligible compared to the incident energy ($k_i \approx k_f$). This approximation works well for x-ray diffraction due to the energy of the incident photon but is not a valid assumption for neutron diffraction so that, in practice, inelasticity corrections have to be taken into account [9][8]. This approximation allows a decoupling between structural and dynamical information [5].

The static approximation considers that the energy exchange $\hbar\omega$ is small compared to the incident energy E_0. The $\hbar\omega$ energy corresponds a characteristic time, τ, so that the condition $\hbar\omega \ll E_0$ corresponds to the condition $\tau \ll t_0$, with t_0 the time characteristic for vibrations or relaxations [6]. It implies that the time taken by the neutron (or x-ray photon) to pass from one atom to the next is small compared to an atomic motion. Therefore, a scattering event probes only the static structure of the specimen giving an instantaneous 'snapshot' of the structure. A neutron or x-ray elastic diffraction measurement consists in time-averaging snapshots taken by each incident neutron or x-ray photon.

1.3 The Faber-Ziman formalism

For polyatomic materials, the total structure factor is a weighted sum of all *partial structure factors* $S_{\alpha\beta}(Q)$ in the Faber-Ziman formalism [10]:

$$S(Q) = \sum_{\alpha,\beta} W_{\alpha\beta} S_{\alpha\beta}(Q) \tag{7}$$

where $W_{\alpha\beta}$ are the weighting factors and $S_{\alpha\beta}(Q \rightarrow \infty) = 1$. The partial structure factors are identical for x-ray and neutron since they only depend on the structure. On the contrary, the weighting factors are independent of the structure but are different when considering diffraction by x-ray photons or neutrons. As a result, the total structure factors, $S(Q)$, have significant differences in peak positions and intensities between the two diffraction methods (figure 2).

At this point, it is necessary to distinguish the diffraction process between x-ray and neutron. For x-rays, the quantity equivalent to the neutron scattering length is the *atomic form factor*, $f(Q,E)$, which is dependent on both the energy of the incident photon and Q. $f(Q,E)$ correspond to the scattering by the electron cloud (while the neutron scattering length b indicates scattering by the nucleus) and its amplitude increases with atomic number Z (while b can be considered usually as a constant). b and f are tabulated in references [11][12][13][14]. Due to the Q-dependence of the form factors, the expression for the weighting factors is slightly different:

$$W_{\alpha\beta}^{neutron} = \frac{c_\alpha c_\beta b_\alpha b_\beta \left(2-\delta_{\alpha\beta}\right)}{\left(\sum_\alpha c_\alpha b_\alpha\right)^2}$$

$$W_{\alpha\beta}^{X-ray}(Q,E) = \frac{c_\alpha c_\beta f_\alpha(Q,E) f_\beta(Q,E)\left(2-\delta_{\alpha\beta}\right)}{\left(\sum_\alpha c_\alpha f_\alpha(Q,E)\right)^2} \qquad (8).$$

where the Kronecker delta ($\delta_{\alpha\beta}$) takes into account that $S_{\alpha\beta}(Q) = S_{\beta\alpha}(Q)$.

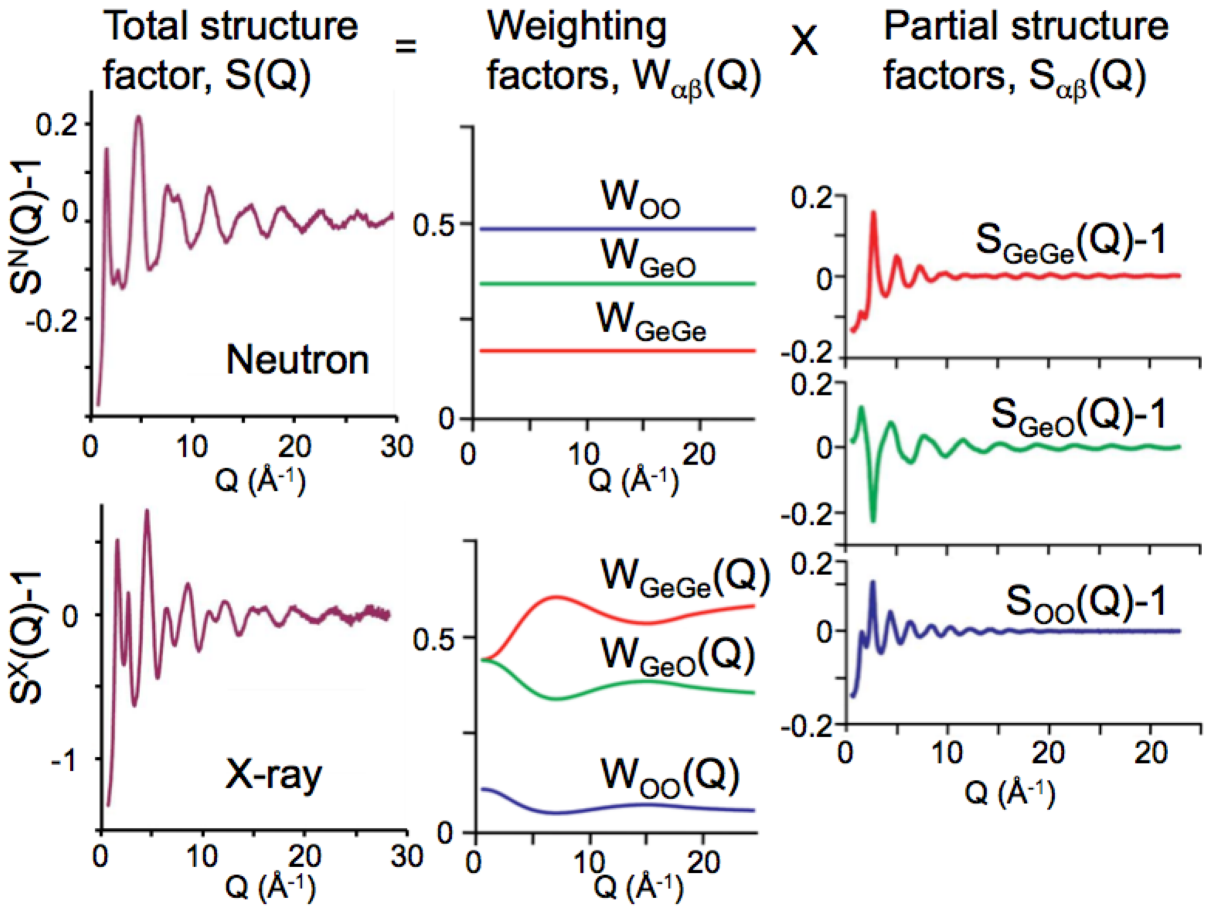

Figure 2: *(right) For GeO_2 glass, the three partial functions $S_{\alpha\beta}(Q)$ contain the structural information. (middle) Each partial structure factor can be multiplied by their respective neutron weighting factors (top) which are constant or by their respective x-ray weighting factors (bottom) which are Q dependent. (left) The sum of all $S_{\alpha\beta}(Q)$ multiplied by their weighting factors give the total structure factor for neutron (top) or x-ray (bottom). Due to the different weighting factors, the total structure factors are different, though the structural information (contained in the $S_{\alpha\beta}(Q)$ functions) is the same. The figure is adapted from [15].*

In the case of the neutron, the Fourier transform in equation (5) is straightforward while, for x-rays, it is the Fourier transform of a product of two functions that gives in real space the convolution of the Fourier transforms of each function:

$$g^{neutron}(r) = \sum_{\alpha,\beta} W_{\alpha\beta}^{neutron} g_{\alpha\beta}(r)$$
$$g^{X-ray}(r) = FT\left(W_{\alpha\beta}^{X-ray}\right) \otimes g_{\alpha\beta}(r) \quad (9).$$

where $\otimes$ is the convolution sign between two functions. To avoid the complex definition of $g^{x\text{-}ray}(r)$, the weighting factors can be simplified:

$$W'^{x-ray}_{\alpha\beta} = \frac{c_\alpha c_\beta K_\alpha K_\beta (2-\delta_{\alpha\beta})}{(\sum_\alpha c_\alpha K_\alpha)^2} \quad (10)$$

with K_α the effective number of electrons for species α. With this simplification, the weighting factor is a constant and the pair distribution function has a simpler formulation $g^{X-ray}(r) = \sum_{\alpha,\beta} W'^{X-ray}_{\alpha\beta} g_{\alpha\beta}(r)$

.

The *partial pair distribution function*, $g_{\alpha\beta}(r)$, gives the probability of finding an atom of type *β* at distance *r* from an atom of type *α* taken at the origin (average distribution of atoms *β* around an atom *α* at the origin) and vice-versa since $g_{\alpha\beta}(r) = g_{\beta\alpha}(r)$.

For a system with *n* components, there are *n(n+1)/2* independent partial structure factors (or partial pair distribution functions, PPDFs). A detailed understanding of the structure requires the complete determination of the set of partial structure factors (or PPDFs) that describe the environment of each atomic species.

1.4 The Bathia-Thornton formalism

An alternative formalism for the partial structure factors has been proposed by Bhatia and Thornton for a binary system based on the local density and concentration [16]. These partial functions correspond to the density fluctuations (topological contribution), $S_{NN}(Q)$, the concentration fluctuations (chemical contribution), $S_{CC}(Q)$, and the correlations between the two, $S_{NC}(Q)$:

$$S(Q) = S_{NN}(Q) + 2\frac{\Delta b}{\langle b \rangle} S_{NC}(Q) + \left(\frac{\Delta b}{\langle b \rangle}\right)^2 S_{CC}(Q) \quad (11)$$

where $\langle b \rangle = c_\alpha b_\alpha + c_\beta b_\beta$ and $\Delta b = \left| b_\alpha - b_\beta \right|$.

These functions are related to the Faber-Ziman partial ones by simple linear combinations, but they emphasize different aspects of the atomic structure as they separate information on the topological order ($S_{NN}(Q)$) from information on the chemical order ($S_{CC}(Q)$):

$$\begin{aligned} S_{NN}(Q) &= c_\alpha^2 S_{\alpha\alpha}(Q) + 2c_\alpha c_\beta S_{\alpha\beta}(Q) + c_\beta^2 S_{\beta\beta}(Q) \\ S_{NC}(Q) &= c_\alpha c_\beta \left[c_\alpha S_{\alpha\alpha}(Q) - \left(c_\alpha - c_\beta\right) S_{\alpha\beta}(Q) - c_\beta S_{\beta\beta}(Q) \right] \\ S_{CC}(Q) &= c_\alpha c_\beta \left[c_\alpha c_\beta \left\{ S_{\alpha\alpha}(Q) + S_{\beta\beta}(Q) - 2S_{\alpha\beta}(Q) \right\} + 1 \right] \end{aligned} \quad (12).$$

Their use is limited, as restricted to binary materials, but several examples can be founded in Salmon's works [17][18][19].

1.5 The Debye equation

For a set of *N* identical atoms in an isotropic specimen, Debye has shown that the structure factor can be simplified as [20]:

$$S(Q) = 1 + \frac{1}{N} \sum_{\alpha=1}^{N} \sum_{\beta \neq \alpha} \frac{\sin Q r_{\alpha\beta}}{Q r_{\alpha\beta}} \quad (13).$$

Each characteristic interatomic distance $r_{\alpha\beta}$ in the sample corresponds in $S(Q)$ to a damped sine wave of period $\Delta Q = 2\pi / r_{\alpha\beta}$. Long period fluctuations in Q-space give rise to short range distances and vice-versa [21].

1.6 Real space functions

Different functions (figure 3) can be used in real space which are all related to the pair distribution function $g(r)$, describing the local fluctuations in density around the unit:

$$g(r) = \frac{\rho(r)}{\rho_0} \quad (14)$$

where $\rho(r)$ is the *r*-dependent atomic density ($g(r \to \infty) = 1$ and $g(r \to 0) = 0$), defining the number of atoms within a sphere or radius *r* [21]. For a polyatomic specimen, the partial pair distribution function $g_{\alpha\beta}(r)$ is the number of atoms of type β between distances *r* and *r* + *dr* from an atom α:

$$g_{\alpha\beta}(r) = \frac{n_{\alpha\beta}(r)}{c_\beta \rho_0 4\pi r^2 dr} \qquad (15).$$

Another commonly used function is the *differential (or reduced) correlation function D(r)* ($D(r \to \infty) = 0$):

$$D(r) = 4\pi r \bar{b}^2 \rho_0 \left[g(r) - 1 \right] \qquad (16).$$

In this function, only deviations from the average atomic density ρ_0 are considered.

The (*total*) *radial distribution function RDF*(*r*) or the *total distribution function T*(*r*) are also used:

$$\begin{aligned} RDF(r) &= 4\pi r^2 \bar{b}^2 \rho_0 g(r) \\ T(r) &= RDF(r)/r = 4\pi r \bar{b}^2 \rho_0 g(r) \end{aligned} \qquad (17).$$

An excellent account of these different definitions is given by Keen [22].

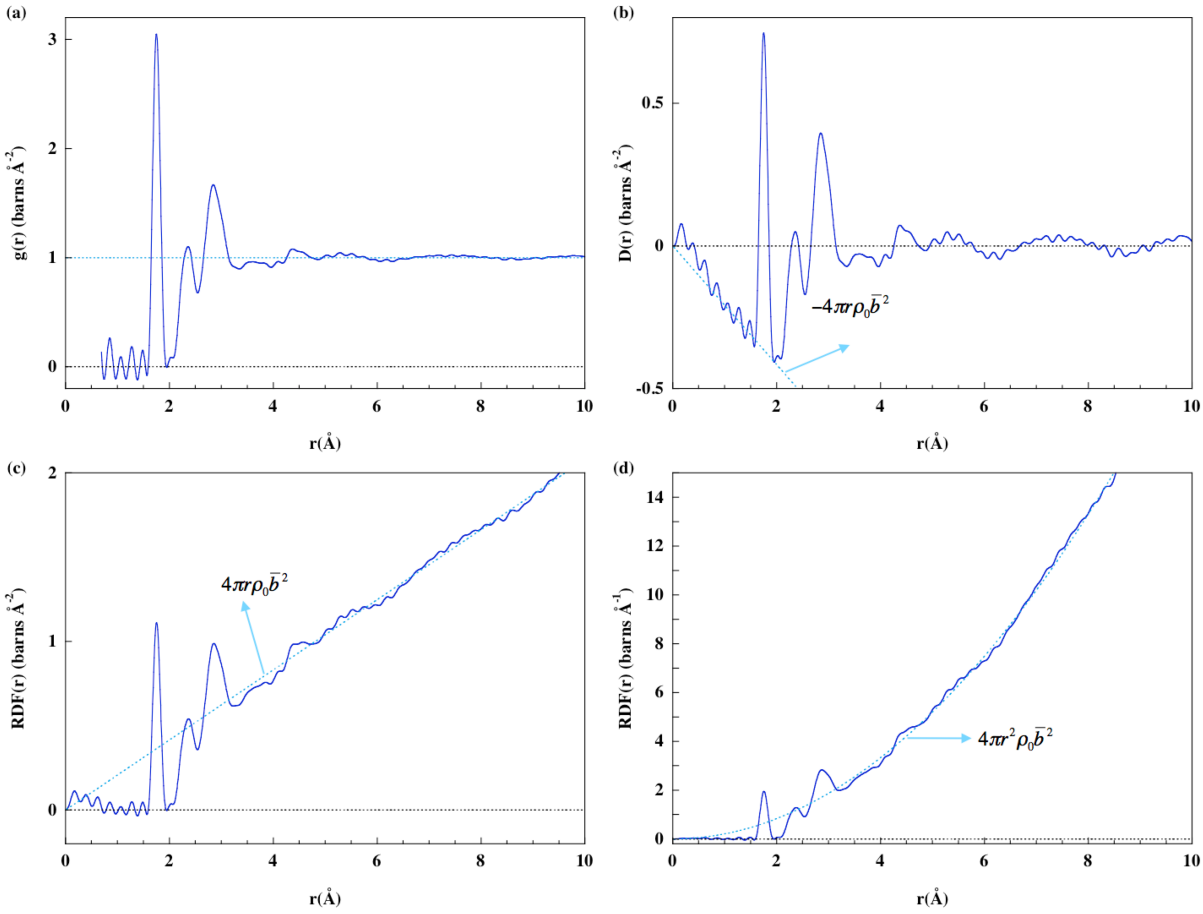

Figure 3: *Relation between the different real space functions (see text) for a 61CaO-39Al₂O₃ glass [23]: (a) the pair distribution function, g(r); (b) the differential correlation function D(r): (c) the total distribution function T(r); (d) the radial distribution function RDF(r).*

1.7 Fourier transformation

1.7.1 Effect of Q range

As shown in figure 4.a, access to high-*Q* values (*i.e*. high Q_{max}) is required to achieve high real space resolution. With a small Q_{max} value, the dramatic peak broadening results in an overlapping of atom-atom contributions. A high Q_{max} value allows us to resolve two close interatomic distances.

The *Q*-range accessible experimentally is determined by equation (2). The values of θ are restricted to $2\theta = \pi$ in a scattering measurement. The possibility to increase the *Q*-range is thus achieved essentially by using high incident energy (short incident wavelength λ) either from synchrotron sources for x-rays or from spallation sources for neutrons.

An example is provided by Petkov *et al*. that used high energy x-ray diffraction (HE-XRD) with Q_{max} = 40 $Å^{-1}$ in aluminosilicate glasses [24]. The Si-O and Al-O distances, only separated by 0.15 Å, can be clearly differentiated. Using a neutron spallation source, similar Q_{max} values can be reached. With such diffraction experiment, the two P-O distances existing within a PO_4 tetrahedra can be resolved [25]. The two P-O components at 1.43 Å and 1.58 Å correspond to the terminal and to the bridging oxygen atoms, respectively.

Finally, we should note that increasing the upper-*Q* limit increases the noise in real space so that sufficient counting statistics at large-*Q* values is needed, which increases the time for measurement.

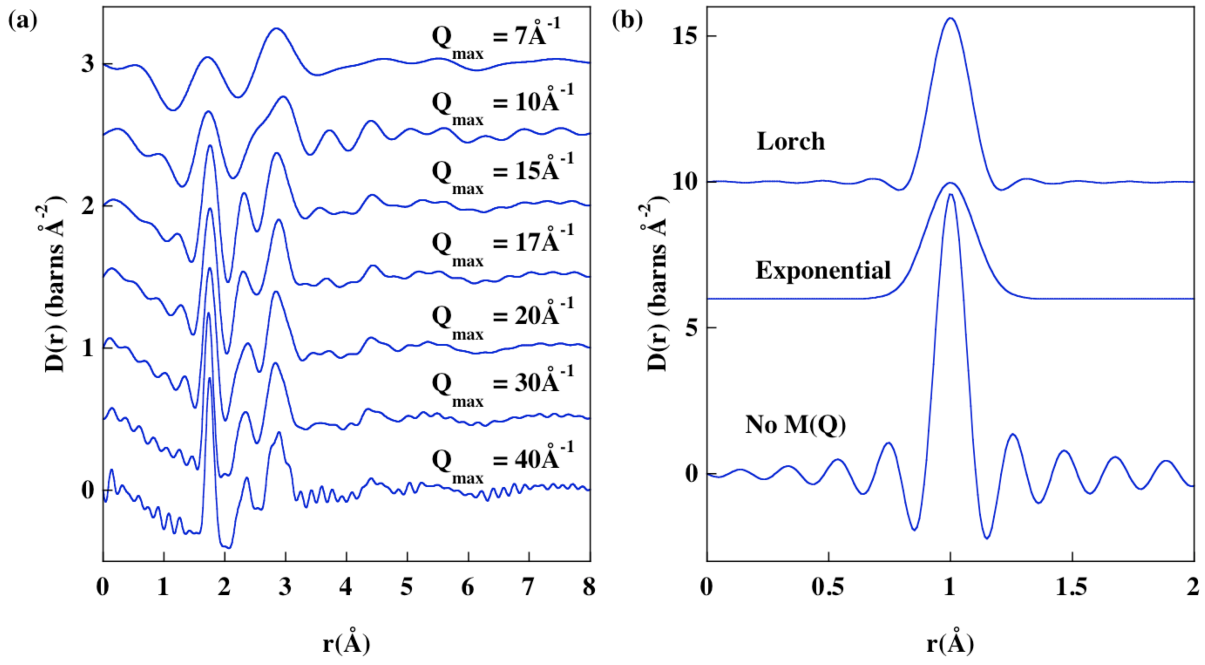

Figure 4: *(a) Example showing how the Q_{max} limit in the Fourier transform of the structure factor affects the resolution in real space for a 61CaO-39Al_2O_3 glass [23]. (b) Influence of the data truncation without modification function and with two modification functions (exponential and Lorch).*

1.7.2 Effect of truncation

The data accessible in diffraction experiments are limited in *Q:* $Q_{min} \leq Q \leq Q_{max}$. The Q_{min} limit does not affect the Fourier transform since low values can be access experimentally and since the structure factor is multiplied by *Q* in the Fourier-sine transform. However, the fact that the Fourier transform cannot be integrated to infinite *Q* results in the appearance of peak broadening and parasitic lobes around the peaks in *D(r)*, particularly at low *r* values. This truncation of the upper-*Q* limit is equivalent to multiplying the interference function $F(Q) = Q(S(Q) - 1)$ by a modified $M(Q)$ function:

$$D(r) = \frac{2}{\pi}\int_0^{\infty} M(Q)F(Q)\sin(rQ)dQ \qquad (18)$$

with $M(Q)\begin{cases} = 1 \;\; when \;\; Q \leq Q_{\max} \\ = 0 \;\; when \;\; Q > Q_{\max} \end{cases}$.

The introduction of $M(Q)$ is equivalent to a convolution of the correlation function with a peak shape function, $P(r)$, which is the cosine transform of $M(Q)$ [26]:

$$D'(r) = \int_0^{\infty} D(r)P(r-u)du \qquad (19)$$

with $P(r) = \frac{2}{\pi}\int_0^{\infty} M(Q)\cos(rQ)dQ$.

If $M(Q)$ is a step function, $P(r)$ is a SINC function, giving important termination ripples. The effect of truncation can be partly suppressed by using different $M(Q)$ functions damping the data cut-off at Q_{max}. This effect is illustrated in figure 4.b.

The primary modification function is a Lorch function [27]:

$$M(Q)\begin{cases} = \dfrac{\sin(\Delta rQ)}{\Delta rQ} \;\; when \;\; Q \leq Q_{\max} \\ = 0 \;\; when \;\; Q > Q_{\max} \end{cases} \qquad (20)$$

with $\Delta r = \pi / Q_{max}$, corresponding to a resolution length in real space.

These smoothly decaying functions reduce unphysical oscillations, but at the expense of further broadening of the peaks in $D(r)$. More sophisticated functions using *r*-dependent real space broadening were recently proposed in order to minimize the broadening near the first peak [28][29].

The *Q* resolution of the instrument adds another exponential dampening effect to the real space information [30]. This has no effect at short *r* distance but prevent extraction of pair correlation information beyond ~50 Å [31]. For glasses and liquids, structural fluctuations are not discernible at large *r* (isotropic medium) and the atomic density $\rho(r)$ tends to ρ_0 at large *r* so that integration can be truncated safely at $r \gtrsim 2$ nm.

1.8 Data processing

The purpose of a diffraction experiment is to measure *I*(*Q*) and makes all the necessary corrections to extract *S*(*Q*). The data treatment has been described in numerous papers for neutron [4][32][7] or x-rays [7][4][28][33]. Absolute intensities can be determined for neutrons thanks to the measurement of standard references with known scattering cross-section, such as vanadium. However, for materials with a high inelasticity or major absorption corrections (for example, Li or H), care is necessary in the analysis of neutron diffraction data. The normalization is not straightforward for x-rays and can lead to uncertainties in the determination of the coordination numbers. All sources have adequate codes to correct the data and we could cite mainly *GUDRUN* for neutron spallation sources [34], *CORRECT* for steady-state neutron reactors [35], *GUDRUNX* [28] or *PDFgetX3* [36] for x-ray sources.

Once *S*(*Q*) is correctly obtained, the Fourier transformation allows us to obtain real space information.

2. Complementarity of Neutron and x-ray

Neutron and x-ray diffraction techniques are often associated to provide additional information on the structure of disordered materials (Table 1). These two methods allow access to wide *Q*-range domains and thus offer a good resolution of bond lengths and numbers of first neighbors. Neutron diffraction has significant differences with x-ray diffraction [7]. While an x-ray photon is scattered by the atomic electron density, the uncharged neutron interacts directly with the (small) atomic nucleus. As a result, neutrons can be used to study the structural position of light elements such as H or Li and are thus well suited to study aqueous solutions, glassy ices or glass electrolytes for solid-state batteries. Conversely x-ray diffraction is sensitive to high-*Z* elements. These two techniques are thus complementary because they are sensitive to different elements (figure 2).

Neutron scattering lengths exhibit a non-monotonous evolution as a function of the atomic number, Z, and are *Q*-independent, while x-ray atomic form factors directly depend on Z and decrease to zero at large-*Q* values (figure 5). This will limit Q_{max} values that are obtainable, particularly for

samples containing low *Z*-elements. Neutron interaction with a given atom nucleus varies not straightforwardly with Z, as it does in the case for x-ray, but may be very different between two neighboring elements and even between isotopes of the same element. This last property is at the basis of the isotopic substitution method (part 4.1). For x-rays, the possibility that the atomic form factor varies close to the absorption edge of a specific element allowed the development of the anomalous scattering method (part 4.2).

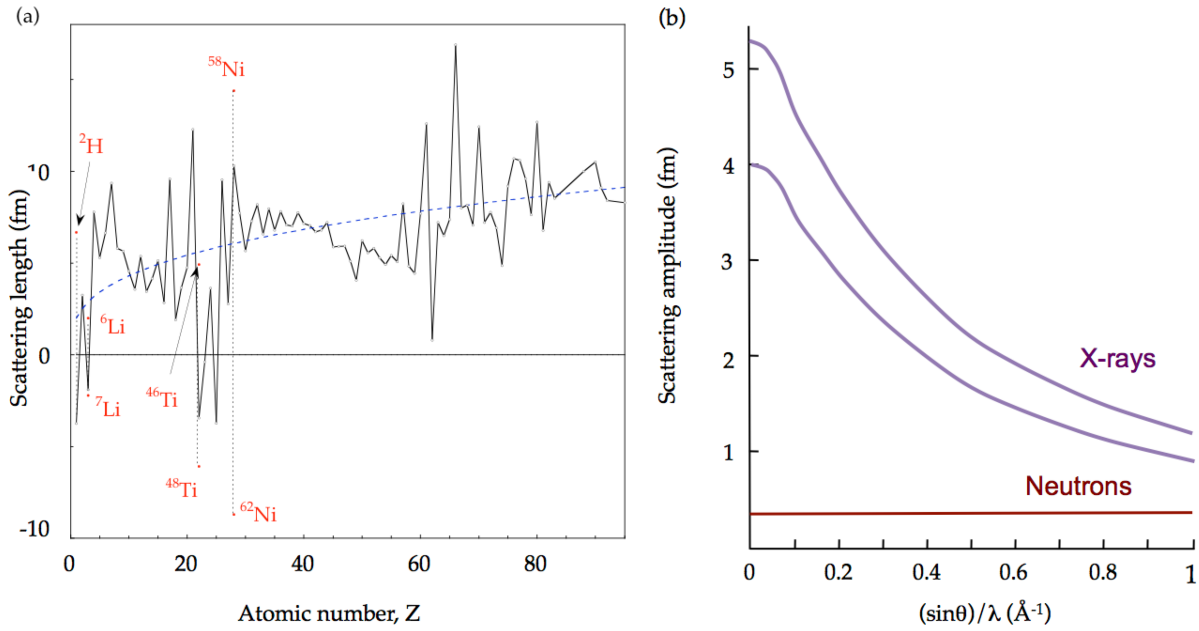

Figure 5: *(a) Erractic evolution of neutron scattering lengths as a function of the atomic number, Z (solid curve), with the slowing increasing potential scattering (dashed curve). (b) Evolution of the x-ray and neutron scattering amplitudes as a function of sin(θ)/λ.*

The coupling of the two diffraction methods was widely used to study borate or phosphate glasses with high ionic conduction. The glassy borate or phosphate networks could be studied more specifically with the neutron diffraction results, while the organization of the elements responsible for the ionic conduction (alkali oxides or salts) can be investigated by x-ray diffraction [25][37][38][39][40][41].

Table 1. *Comparison of neutron and x-ray diffraction*

x-ray	Neutron
Interaction with electronic cloud	Interaction with the nucleus

f(*Q*,*E*) atomic form factor strong variation of scattered intensity with θ information on high-Z elements weak scattering for low-Z elements weak contrast for elements with close Z *f* varies with the energy ⇒ anomalous scattering	*b* neutron scattering length constant, independent of θ not a monotonous function of Z light elements are visible (H, Li, N, O, etc) possibility to distinguish elements with close Z *b* can vary at some energies for some elements ⇒ anomalous scattering limited *b* varies among isotopes of the same element => isotopic substitution
Small samples	Large samples
Radiation can cause damage	Radiation can cause activation
No magnetic information	Magnetic information is possible

3. Determination of the structural parameters

Structural information is easier to visualize and extract in real space (figure 6). The peak position gives directly the average interatomic bond length, $r_{\alpha\beta}$, between an atom α taken at the origin and an atom β at the distance $r_{\alpha\beta}$. Provided that there is limited overlap with other interatomic contributions, a great precision can be achieved: the Si-O bond length has been determined at 1.605 ± 0.003 Å using neutron diffraction [42].

The coordination number, $N_{\alpha\beta}$, defines the average number of neighbors β around an atom α, and it can be calculated by integrating the area under the α–β peak:

$$N_{\alpha\beta} = 4\pi\rho_0 c_\beta \int_{r_1}^{r_2} g_{\alpha\beta}(r) r^2 dr \qquad (21)$$

where the integration limits (r_1-r_2) define the coordination shell. These limits are not always well-defined, in particular in case of partial overlap with another contribution, which affect the accuracy.

The width of the peak $\sigma_{\alpha\beta}$ gives a measure of the distribution of interatomic distances due to both static structural and thermal disorder. However, the determination of $\sigma_{\alpha\beta}$ is not direct since a peak

broadening results from the limited-*Q* integration of the structure factor giving the correlation function.

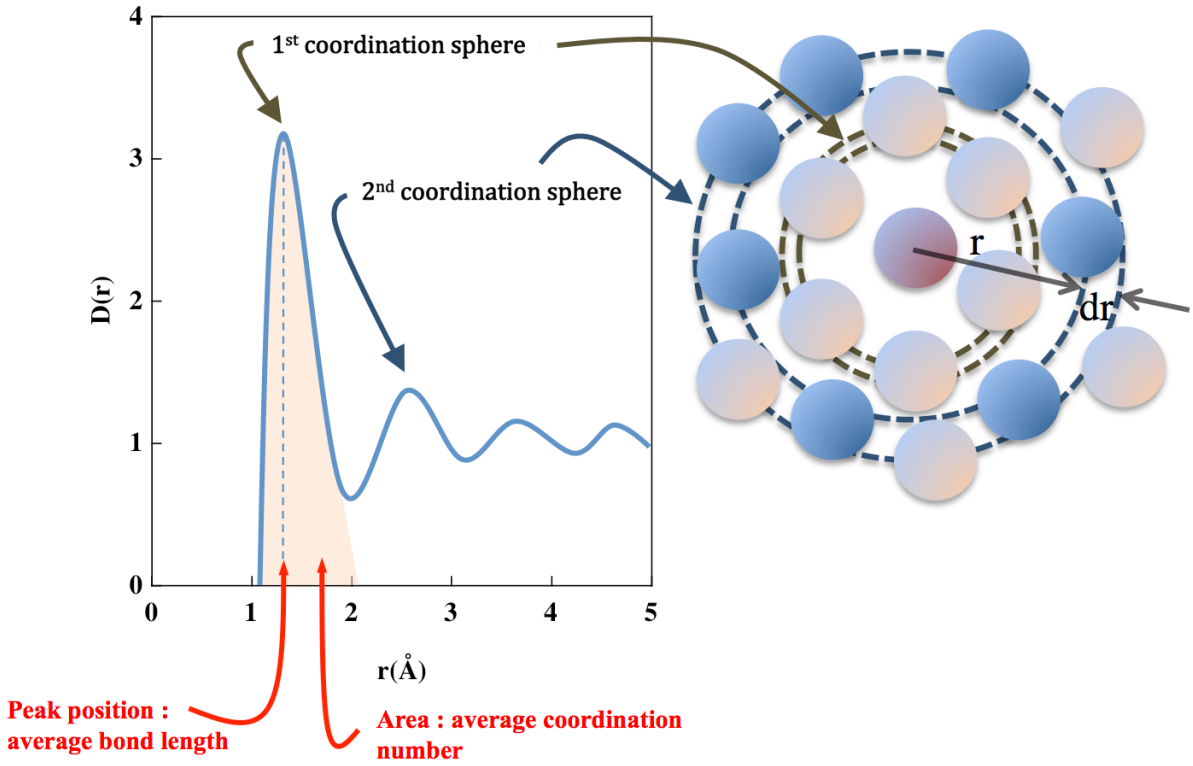

Figure 6: *Correlation function and real space information.*

$N_{\alpha\beta}$ and $\sigma_{\alpha\beta}$ factors are closely correlated and subject to more uncertainties. The coordination number is the least accurate parameter because it varies strongly with the slope at the origin or the *Q*-range, and the accuracy decreases in case of overlapping peaks. The ability to use different functions (total or partial), that must give the same information, can provide guidance on the accuracy of the values.

These three parameters are often obtained by performing a Gaussian fit of the peak, allowing $r_{\alpha\beta}$, $N_{\alpha\beta}$ and $\sigma_{\alpha\beta}$ to vary.

$$g_{\alpha\beta}(r) = \frac{W_{\alpha\beta}N_{\alpha\beta}}{c_\beta r\sqrt{2\pi\sigma_{\alpha\beta}^2}}\exp\left(-\left(r-r_{\alpha\beta}\right)^2 \Big/ 2\sigma_{\alpha\beta}^2\right) \quad (22).$$

The weighting factors $W_{\alpha\beta}$ are calculated from tabulation of *b* and *f* [11][12][13][14] and the atomic fraction, *c*, is provided by the chemical analysis of the samples.

The $D(r)$ and $T(r)$ functions should be preferred as the finite Q_{max} results in a symmetric peak broadening for these functions [43]. To take into account the Q_{max} truncation, Gaussian functions have to be convoluted by a resolution function in real space given by the Fourier transform of the Lorch function [44].

4. Difference methods

The $D(r)$ function is informative but dominated by the correlations having large weighting factors, *e.g*. usually Si-O, O-O and Si-Si in silicate glasses for neutron diffraction measurements. On the other hand, above 3 Å, the various contributions are superimposed, the contributions with small weighting factors being overlapped by those having large weighting factors. It becomes extremely difficult above 3 Å to deconvolute the various contributions for a multicomponent material. The use of structural models can offer an interpretation of $D(r)$ but this is of course not unequivocal.

For a system with n-component, there are $n(n+1)/2$ partial structure factors (or PPDFs) that one wants to retrieve to describe the structure. The detailed understanding of the atomic structure requires the complete determination of the set of partial structure factors, which means that $n(n+1)/2$ distinct experiments are required. In simple systems, this can be obtained by applying different contrast variation methods. For multicomponent glasses or liquids, these techniques allow the extraction of structural information for one specific element that is otherwise buried beneath other contributions with strong weighting factors.

The only element in $S(Q)$ that is not structure or composition dependent is the neutron scattering length, b, or the atomic form factor, $f(Q,E)$. b can vary significantly in amplitude or sign from one element to another or between isotopes of the same element. The first property is used in isomorphic substitutions (exchange of elements playing an identical role in the structure [45]) while the second led to a more rigorous method of contrast, that of isotopic substitution. f can change close to the absorption edge characteristic of a given element due to anomalous dispersion. The contrast variation is thus the possibility to modify the scattering power (b or f) of a specific element to extract the partial functions associated to this element. The higher the contrast variation, the higher the reliability of the results.

4.1 Neutron diffraction with isotopic substitution (NDIS)

The isotopic substitution method was used for the first time by Enderby to retrieve the three partial structure factors of liquid Cu-Sn alloy [46]. This technique is based on the measurement of the neutron

diffraction (ND) by two samples, prepared rigorously identically (thus assuming the same structure, *i.e*. same c_α, c_β and $g_{\alpha\beta}(r)$) but with different isotopic concentrations for one species, here called *M*. One can measure two total structure factors from these two samples, where only the weight of the partial structure factors involving *M* can vary:

$$S(Q) = \sum_{\alpha,\beta\neq M} c_\alpha c_\beta b_\alpha b_\beta \left(S_{\alpha\beta}(Q)-1\right) + \sum_{\substack{\alpha \\ \alpha\neq M}} c_\alpha c_M b_\alpha b_M \left(S_{\alpha M}(Q)-1\right) + c_M^2 b_M^2 \left(S_{MM}(Q)-1\right)$$
$$S'(Q) = \sum_{\alpha,\beta\neq M} c_\alpha c_\beta b_\alpha b_\beta \left(S_{\alpha\beta}(Q)-1\right) + \sum_{\substack{\alpha \\ \alpha\neq M}} c_\alpha c_M b_\alpha b'_M \left(S_{\alpha M}(Q)-1\right) + c_M^2 b'^2_M \left(S_{MM}(Q)-1\right) \quad (23).$$

The difference technique consists to subtract these two quantities and therefore to eliminate all terms not involving *M* since they are identical. The subtraction gives the first difference function, $\Delta_M(Q)$, which is the sum of the partial structure factors centered on the element *M*. After Fourier transformation, the *M*-centered pair correlation function is obtained:

$$G_{M\alpha}(r) = \frac{2}{\pi}\int \Delta_M(Q) Q sin(Q) dQ$$
$$= 2\sum_{\alpha\neq M} c_\alpha c_M b_\alpha (b_M - b'_M) g_{M\alpha}(r) + c_M^2 \left(b_M^2 - b'^2_M\right) g_{MM}(r) \quad (24).$$

We have thus a chemically selective probe. The resulting function is analogous to the difference calculated by anomalous x-ray diffraction (part 4.2) or to the Fourier transformation of the EXAFS signal obtained by x-ray absorption spectroscopy.

Additionally, it is possible to measure three samples and thus to obtain two first differences, $\Delta_M(Q)$ and $\Delta'_M(Q)$:

$$\Delta_M(Q) = 2\sum_{\alpha\neq M} c_\alpha c_M b_\alpha \left(b_M - b'_M\right)\left(S_{M\alpha}(Q)-1\right) + c_M^2 \left(b_M^2 - b'^2_M\right)\left(S_{MM}(Q)-1\right)$$
$$\Delta'_M(Q) = 2\sum_{\alpha\neq M} c_\alpha c_M b_\alpha \left(b'_M - b''_M\right)\left(S_{M\alpha}(Q)-1\right) + c_M^2 \left(b'^2_M - b''^2_M\right)\left(S_{MM}(Q)-1\right) \quad (25).$$

The weighting factors depend on the difference of the scattering lengths of *M* for the terms *M*-α ($\alpha \neq M$) while the term *M*-*M* depends on the difference of the square of the scattering lengths. Therefore, a judicious choice of the isotopic composition of the three glasses allows us to equalize the quantity $\Delta b = b_M - b'_M$ and $\Delta' b = b'_M - b''_M$. This condition is easily obtained:

$$b' = \frac{b + b''}{2} \quad (26).$$

The subtraction of these two functions in equation (25) gives the second difference function, $\Delta(\Delta_M)(Q)$, in which only the *M*-*M* correlation is present:

$$\Delta\left(\Delta_M\right)(Q) = \frac{1}{2} c_M^2 \left(b_M - b_M''\right)^2 \left(S_{MM}(Q) - 1\right) \quad (27).$$

This function is of course related to a pair correlation function that directly describes the distribution of the element *M* within the structure:

$$\begin{aligned} G_{MM}(r) &= \frac{2}{\pi} \int \Delta\left(\Delta_M\right)(Q) Q \sin(rQ) dQ \\ &= c_M^2 \frac{\left(b_M - b_M''\right)^2}{2} g_{MM}(r) \end{aligned} \quad (28).$$

The limits of NDIS are firstly the small number of elements with isotopes that are suitable. x-rays (with anomalous diffraction) allow access to more elements but they cannot probe light ones such as hydrogen or lithium. These isotopes should be stable and must not be too absorbent. It is necessary that the difference between the scattering lengths of isotopes is large enough, typically Δb > 3 fm, to get a first and a second difference. A lower Δb may give access only to a first difference, especially for atomic concentrations lesser than 3 at%. A recent study has demonstrated that oxygen isotope substitution method can be carried out using O^{16} and O^{18} isotopes with a Δb of only 0.142 fm [47]. In their experiments, they found a 0.5% difference between the O-H and O-D bond lengths in water, supporting a competing quantum effects model.

Many errors can seriously limit the accuracy (and even correctness) of the difference functions. This method, in contrast to anomalous x-ray diffraction, uses several specimens synthesized under the same conditions and assumed that they have the same structure. Each sample should be identical with the exception of the isotopic composition of *M*. This means that the concentration of each element must be perfectly known. The isotopic ratios of *M* must also be determined to be able to properly assess b_M for each sample (although the scattering lengths are not always known precisely). Errors can therefore quickly accumulate and seriously contaminate the second difference, making its extraction delicate.

The first difference has the advantage of reducing the problems associated with systematic errors: corrections of inelasticity and multiple-scattering are largely eliminated in the subtraction. However, we must be aware that those terms reappear in the second difference.

For a binary system, the treatment can be summarized in matrix form:

$$\begin{bmatrix} S_1(Q) \\ S_2(Q) \\ S_3(Q) \end{bmatrix} = \begin{bmatrix} c_\alpha^2 b_\alpha^2 & c_M^2 b_M^2 & 2c_\alpha c_M b_\alpha b_M \\ c_\alpha^2 b_\alpha^2 & c_M^2 b_M'^2 & 2c_\alpha c_M b_\alpha b_M' \\ c_\alpha^2 b_\alpha^2 & c_M^2 b_M''^2 & 2c_\alpha c_M b_\alpha b_M'' \end{bmatrix} \begin{bmatrix} S_{\alpha\alpha}(Q) \\ S_{\alpha\beta}(Q) \\ S_{\beta\beta}(Q) \end{bmatrix} \quad (29)$$

$$\left[S(Q)\right] = \left[A\right]\left[X(Q)\right]$$

with $S_1(Q)$, $S_2(Q)$ and $S_3(Q)$ the three distinct measurements and changing the isotopic state of the element *M*. The formal solution consists in obtaining the partial functions by matrix inversion:

$$\left[X(Q)\right] = \left[A\right]^{-1}\left[S(Q)\right] \quad (30).$$

A few elements (H, Li, Ti, Ni, Cr, Dy) have isotopes with both positive and negative scattering lengths, so that an isotopic mixture can be prepared with a null average scattering length. For a binary system having an element with a zero scattering length, the partial structure factor for the other element is directly measured in a single experiment. This null isotopic substitution technique has been used in several cases: for Dy and Ni in a Dy_7Ni_3 metallic glass allowing the separation of all partial functions [48] or in liquid $NiSe_2$ to isolate the Se-Se partial structure factor [49].

4.2 Anomalous x-ray diffraction (AXRD)

x-ray diffraction (XRD) is widely used as a complementary technique to neutron diffraction (part 2) and can also allow the determination of partial functions through a difference method. The structure factor determined by XRD is the sum of all the partial structure factors as shown in equation (7) but, contrary to *b*, the atomic form factors *f* depend upon Q and the incident energy, E. It is possible to change $f(Q,E)$ at the absorption edge energy, E_{edge}, of a specific element, leading to the technique of anomalous x-ray diffraction [50][51].

The atomic form factor has a complex nature:

$$f(Q,E) = f_0(Q) + f'(E) + if''(E) \quad (31).$$

$f_0(Q)$ is the usual energy-independent term that controls the *Q*-dependence. $f'(E)$ and $f''(E)$ are the real and imaginary parts corresponding to the anomalous term. Near an absorption edge, they change drastically giving different scattering.

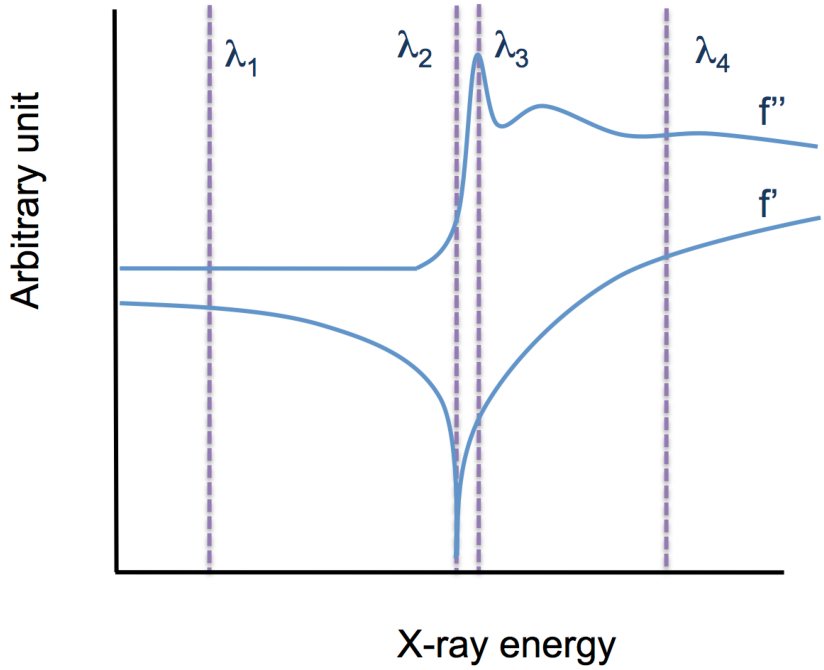

Figure 7: *Variation of f' and f'' near an absorption edge energy E_{edge} (λ_2, λ_3). AXRD usually considers two experiments at the edge (λ_2 or λ_3) and far below the edge (λ_1) where f' and f'' are almost constant, rather than above the edge (λ_4) due to oscillations in f''.*

In an AXRD experiment, the scattering intensities for a same sample are measured at two different energies (figure 7), one close to the absorption edge E_{edge} (where the variation of f is the highest) and another one several hundred eV below E_{edge} (to avoid problems of absorption and fluorescence above E_{edge}). The subtraction of the two measured intensities gives a first difference function:

$$\Delta_M(Q) = \sum_{\substack{\alpha \\ \alpha \neq M}} DW_{\alpha M}\left(S_{\alpha M}(Q) - 1\right) \tag{32}$$

with $DW_{\alpha M}(Q)$ the differential weighting factor for the pair α-M:

$$DW_{\alpha M} = \frac{c_\alpha c_M D\left(f_M f_\alpha^* + f_M^* f_\alpha\right)}{D\left(\left|\langle f \rangle\right|^2\right)} \tag{33}.$$

The difference function limits information to the environment around the specific element, M, but this limitation is not a handicap because it allows us to isolate a signal which is overlapped in the total distribution function by stronger correlations. Though AXRD can be obtained at three different energies allowing the extraction of a second difference function, the contrast to retrieve a partial function *M-M* is low and this method has been little used. An example is the study of the distribution of Ba in silicate glasses [52]. Anomalous diffraction can also be obtained for certain energies using neutrons [53], but this is restricted to a limited number of elements (*e.g.* Sm).

An advantage of AXRD is that a large number of elements are available, especially considering the possibility of using K or L absorption edges for low- and high-Z elements, respectively. The major limitation concerns the accessible Q range that is limited by the choice of the absorption edge energy, $E_{edge} = hc / \lambda_{edge}$. Given this wavelength λ_{edge}, a maximum momentum transfer of $Q_{max} = 4\pi \sin\theta_{max} / \lambda_{edge}$ can be obtained. In practice, a minimum E_{edge} of 10 eV is necessary, to get a Q_{max} ~10 $Å^{-1}$. Therefore, AXRD is suited for elements of $Z \geq 26$ (iron K-edge absorption).

As an example, this technique has been applied to Ge_xSe_{1-x} glasses at energies close to the Ge and Se K-edges absorption. The partial functions show a gradual change with x but intermediate-range structure probed by pre-peak position in the $S_{SeSe}(Q)$ partial structure factor indicates that the stiffness transition at $x = 0.20$ can be observed [54].

4.3 Coupling x-ray and neutron diffraction

One possibility of determining the difference function is by combining neutron and x-ray data, which can be realized on the same sample [4]. A first order difference function can be obtained, though the sources of errors are important due to different experimental set-ups and resolutions and due to the Q-dependence of the form factors.

5. RMC and related methods

Despite the development of experimental techniques, our representation of the glass structure remains partial. The use of simulations can help to better constrain structural models. Since correlation functions are one-dimensional, the construction of three-dimensional structural models can be used to describe the isotropic 3-D arrangements characteristic of glass structure. Different modeling techniques associated with fitting of the experimental diffraction data have been developed, in particular Reverse Monte Carlo (RMC) and Empirical Potential Structure Refinement (EPSR). There are analogs for disordered materials to the Rietveld refinement methods for crystalline powder patterns.

An analogy can be pointed out between the $g(r)$ and the pair potential $V(r)$ (figure 8). The low-r part represents the repulsion of two neighboring atoms defining the distance of closest approach between atoms. This mimics the coulombic repulsive term in V(r) that hinders the particles from colliding. The peak position and width between two neighboring atoms in $g(r)$ mimics the form of the pair potential (energy position and depth of the potential well), *i.e*. the attractive term of the potential.

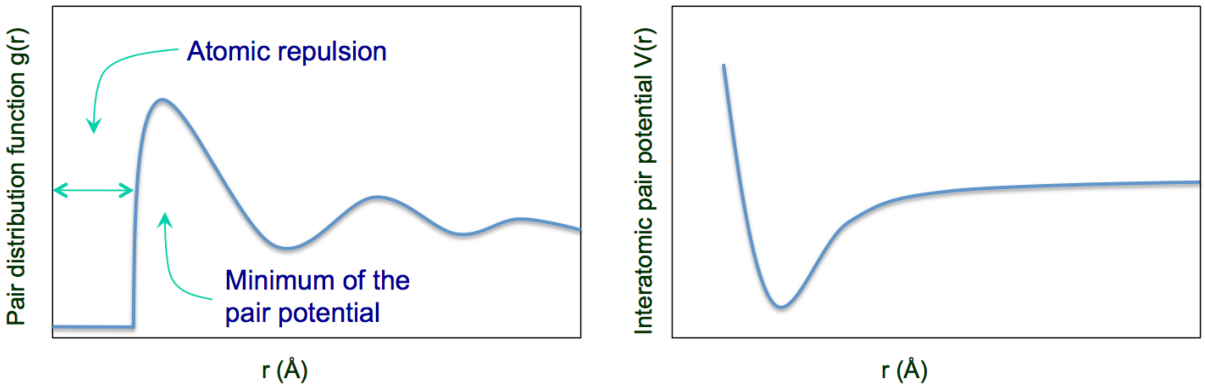

Figure 8: *Analogy between the pair distribution function and the interatomic pair potential (see text).*

Molecular dynamics and Monte Carlo techniques have been more widely used. Molecular Dynamics (MD) allows tracking the movements of a set of atoms interacting within a given potential force field as a function of time and also of the temperature/pressure. Information on the liquid dynamics behavior at the glass transition temperature or on the glass structure can be obtained. This method has been applied to a large number of oxide glasses [55][56]. However, for reasons of computational time, quenching rates are significantly higher than those obtained experimentally [57]. In addition, the determination of potential correctly representing the atomic interactions is difficult. As an alternative to this approach, the Monte Carlo method use potentials and move randomly atoms to minimize the energy of the system [58].

These models can be compared to experimental data to test the validity of simulations over different length scales or to improve the pair potentials. The evaluation of the (dis)agreement between simulation and experiment should require a factor of goodness of fit, such as the one proposed by Wright [59]:

$$R_\chi \left(\frac{\sum_i \left[T_{\exp}(r_i) - T_{sim}(r_i) \right]^2}{\sum_i T_{\exp}^2(r_i)} \right)^{1/2} \quad (34).$$

with T_{exp} and T_{sim} the experimental and simulation total distribution functions

If the agreement is not satisfactory, other techniques can be used for elucidating the detailed atomic structure based on fitting the experimental diffraction data (and possibly additional structural information). The Reverse Monte Carlo (RMC) method involves iteratively moving a set of atoms randomly to reproduce the experimental data, without recourse to interatomic potentials [60][61][61]. After each random move, the difference between experiment and model is calculated and, if the move improves the agreement, the atomic displacement is accepted, otherwise the structure change is

allowed with some probability to avoid local minima. This procedure is repeated until a satisfactory refinement of the experimental data is achieved. Additional constraints such as the density, know coordination numbers, etc, can greatly improve the final RMC model. RMC allows the generation of atomistic models in quantitative agreement with diffraction data and structural information extracted from these models can improve our understanding of the glass structure.

The initial model is a key parameter in RMC modeling. Large atomic boxes are required, containing several thousands of atoms. Random configurations are usually chosen but, after RMC fitting, such structures yield models with important and unrealistic entropic energies. Indeed, RMC is a maximum entropy approach giving the most disordered structure that is in accord with the experimental data. MD simulations offer more realistic starting models if interatomic potentials are available [62]. Even with the best current MD simulations, differences in peak positions and intensities exist with the experimental data. We present in figure 9.a a comparison between neutron data and MD simulations obtained on a $MgSiO_3$ glass with pair interaction potentials [63], showing small discrepancies in the structure factors between experiments and MD. These models can therefore be adjusted by using the RMC method to obtain atomistic structures in agreement with the experimental data (figure 9.b).

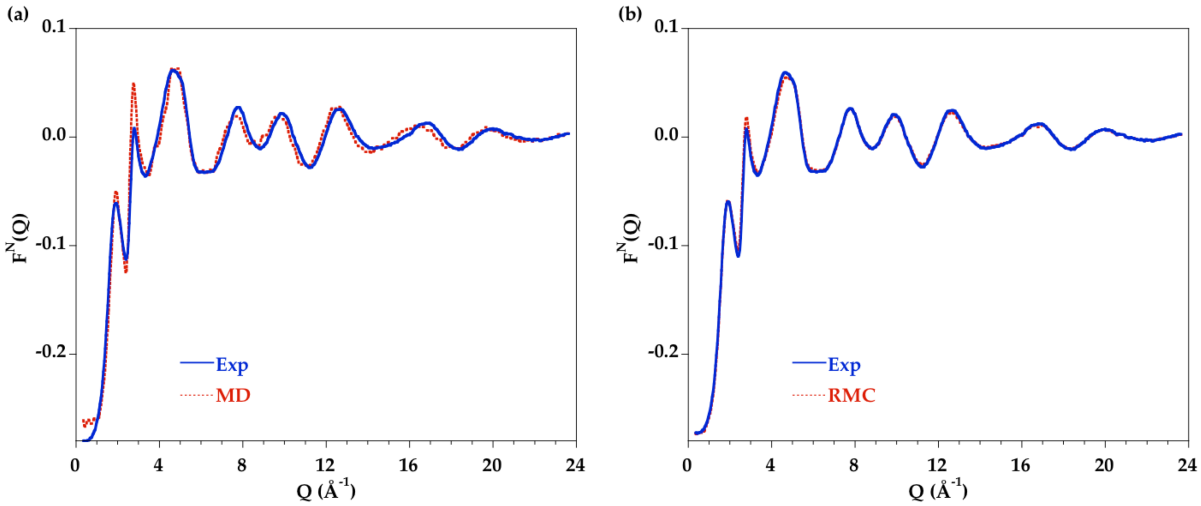

Figure 9: *(a) Comparison between neutron structure factors obtained experimentally (solid line) and by MD simulations for a $MgSiO_3$ glass. (b) Comparison between neutron structure factors obtained experimentally (solid line) and after running RMC starting with the MD simulations.*

Several software packages can be used to realize this RMC fitting process: *RMC++* [64], *RMC_POT* [65] or *RMCProfile* [66], all available at http://wwwisis2.isis.rl.ac.uk/rmc/. Some of these programs now incorporate an extensive use of interatomic potential functions.

The coupling between experiments and RMC allows a better interpretation of the experimental data obtained on multicomponent glasses, since different partial structure factors or partial pair distribution can be extracted. Figure 10 shows the results obtained on a $SrSiO_3$ glass by refining simultaneously ND (figure 10.a) and AXRD at the Sr K-edge (figure 10.b), allowing to obtain a first difference function centered on Sr (figure 10.c). This example shows the interest of coupling the two diffraction techniques due to different weighting factors: ND is most sensitive to the pairs associated with the silicate network and XRD will be heavily weighted by the pairs associated with strontium. This study allowed understanding the arrangements of the Sr cations in glasses and the similarities with crystals of equivalent composition [41].The analysis of correlation functions reveals that strontium has a different environment and a different distribution within the structure if it acts as modifier or charge compensator.

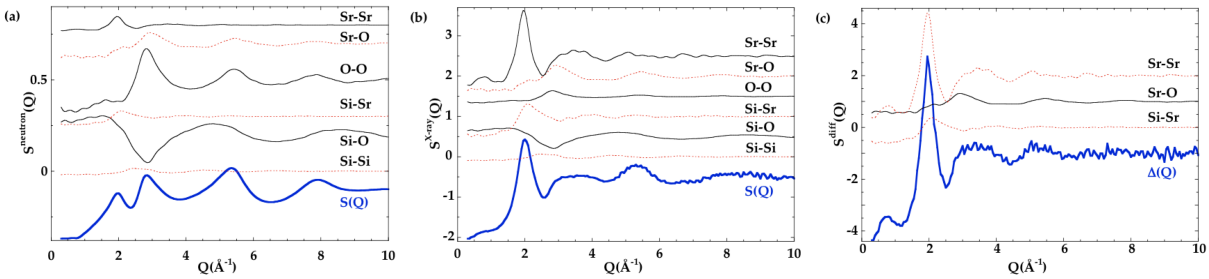

Figure 10: *Total structure factors obtained by (a) neutron diffraction, (b) x-ray diffraction and (c) structure factor of first difference determined by anomalous x-ray diffraction at the Sr K-edge for a $SrSiO_3$ glass, compared with the weighted partial structure factors determined by RMC modeling.*

A RMC development is to improve interatomic pair potentials used in classical MD simulations. Indeed, by calculating partial pairs distributions before and after the RMC procedure, it is possible to determine the pairs that have varied the most and require an optimization of their potential parameters. Figure 11 compares the Ca-O pair before and after the RMC adjustment, which highlights the need for a lower Ca-O bond length to achieve a good agreement with the experimental data. This type of approach allowed the modification of the Ca-O pair potential [67].

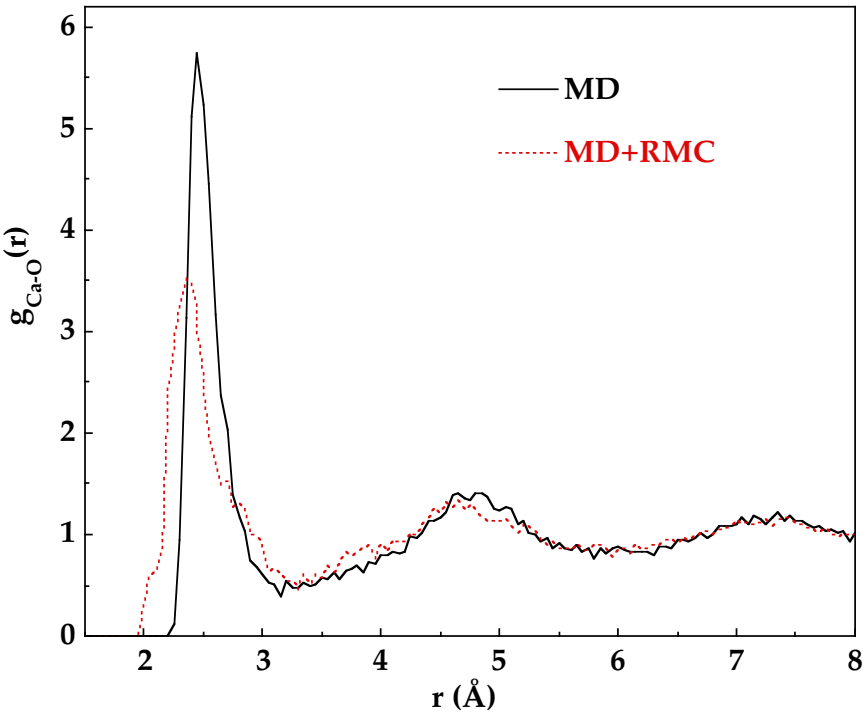

Figure 11: *The Ca-O pair distribution function calculated by molecular dynamics (full curve) and adjusted by RMC (dotted curve) for a 61CaO-39Al_2O_3 glass. There is a displacement of the first peak at 2.44 Å in the MD model to 2.35 Å after RMC. The figure is adapted from [68].*

Much of our existing knowledge about the atomic structure of metallic glasses is based on RMC and diffraction measurements (as well as MD simulations) [69][70][71]. Efficient atomic packing is a fundamental principle underlying the formation and stability in such systems. RMC structural models for binary nickel-based and zirconium-based metallic glasses were obtained [70], enabling knowledge of the three-dimensional positioning of the atoms. The short-range order (SRO) is characterized by solute-centered clusters (various polyhedra of around 9 to 13 atoms) each of which is made up of a solute atom surrounded by a majority of solvent atoms. The intermediate range order (IRO) is constructed by packing of these polyhedral clusters with appreciable icosahedral medium-range order (figure 12), regardless of the short-range order within the clusters. Icosahedral order has a fivefold rotational symmetry that is incompatible with translational symmetry and favor glass forming ability.

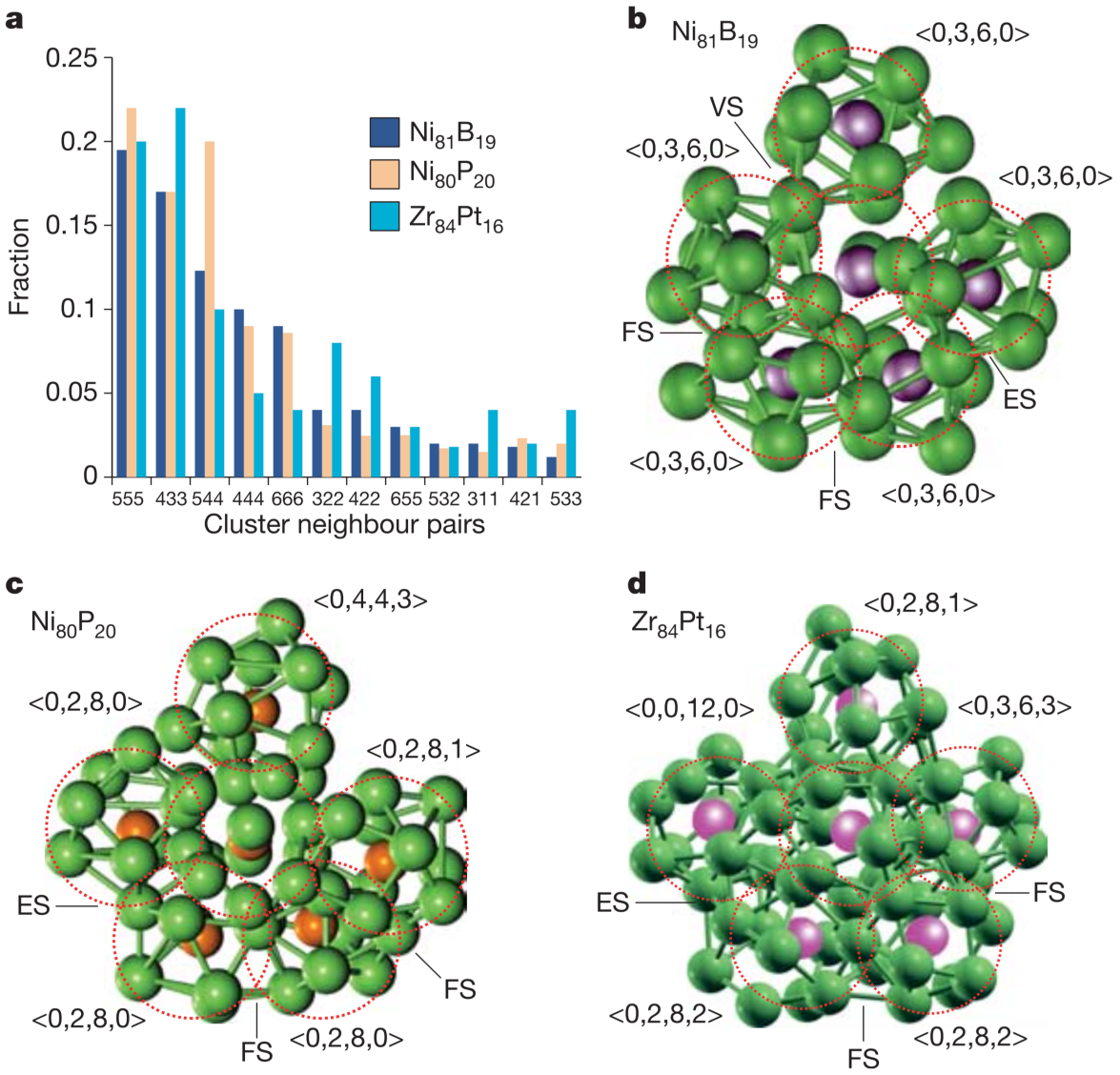

Figure 12: *(a) Cluster neighbor analysis showing that the local clusters (solute-centered polyhedra) exhibit icosahedral order. (b), (c) and (d) Typical packing of clusters showing fivefold symmetry detailed for $Ni_{81}B_{19}$, $Ni_{80}P_{20}$ and $Zr_{84}Pt_{16}$ metallic glasses, respectively. FS, ES and VS stand for face-sharing, edge-sharing and vertex-sharing, respectively. Reprinted by permission from Macmillan Publishers Ltd: Nature ([70]), copyright (2006).*

Another method based on the refinement of diffraction data is Empirical Potential Structural Refinement (EPSR) modeling [72]. This tool uses realistic intra- and inter-molecular potentials that constrain the atomic positions in the simulation box. An empirical potential is introduced as a perturbation to the arbitrary potential functions, generated from the difference between measured and calculated structure factors or radial distribution functions. A Monte Carlo refinement of this empirical potential is successively obtained as the atoms or molecules are move, enabling the best possible agreement with the experimental data. As for RMC, a 3D atomic model is obtained, consistent with the measured diffraction data. This method has been particularly developed for molecular systems, such as water (figure 13).

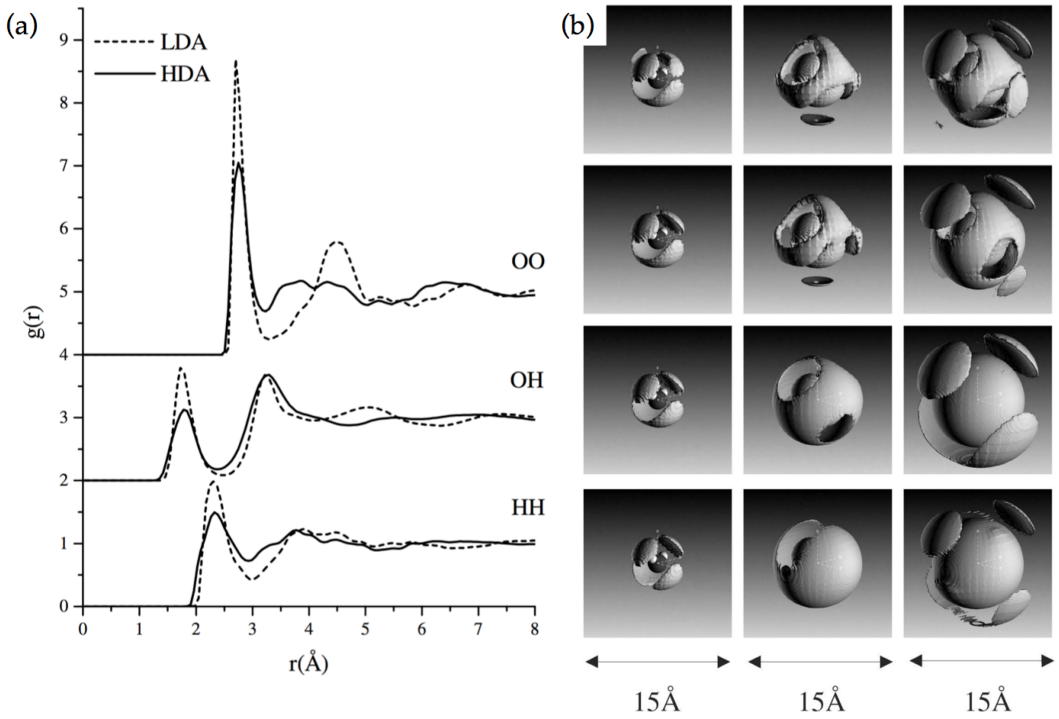

Figure 13: *(a) Inter-molecular PPDFs of high-density (HDA) and low-density (LDA) amorphous water (see section 7.4.1) at 80 K. (b) Three dimensional arrangement of the oxygen atoms around a water molecule (spatial distribution function) showing the first, second and third O neighbors (from left to right) for crystalline ice at 220 K, LDA at 80 K, liquid water at 298 K [24], and HDA at 80 K. Reprinted with permission from [73]. Copyright (2002) by the American Physical Society.*

6. Case studies of glass investigation by neutron and x-ray diffraction

6.1 The low-Q features

In the structure factors, it is often useful to consider the domain at low-Q values. For simple glasses, three peaks Q_1, Q_2 and Q_3 are characteristic features that scale roughly with the interatomic distance d (figure 14): $Q_1.d \simeq$ 2-3, $Q_2.d \simeq$ 4.6-4.9, $Q_3.d \simeq$ 7.7-8.9 [74]. At these peak positions correspond ordering at different length scales: nearest-neighbor separation for Q_3, size of the local network-forming motifs for Q_2 and arrangements of these motifs on an intermediate range for Q_1. Note that some low-Q features are not present for some classes of glasses (*e.g.* Q_1 and Q_2 are absent in metallic glasses) or are not observable for some diffraction methods (*e.g.* Q_2 is present in neutron diffraction data for SiO_2 but absent in the x-ray diffraction data).

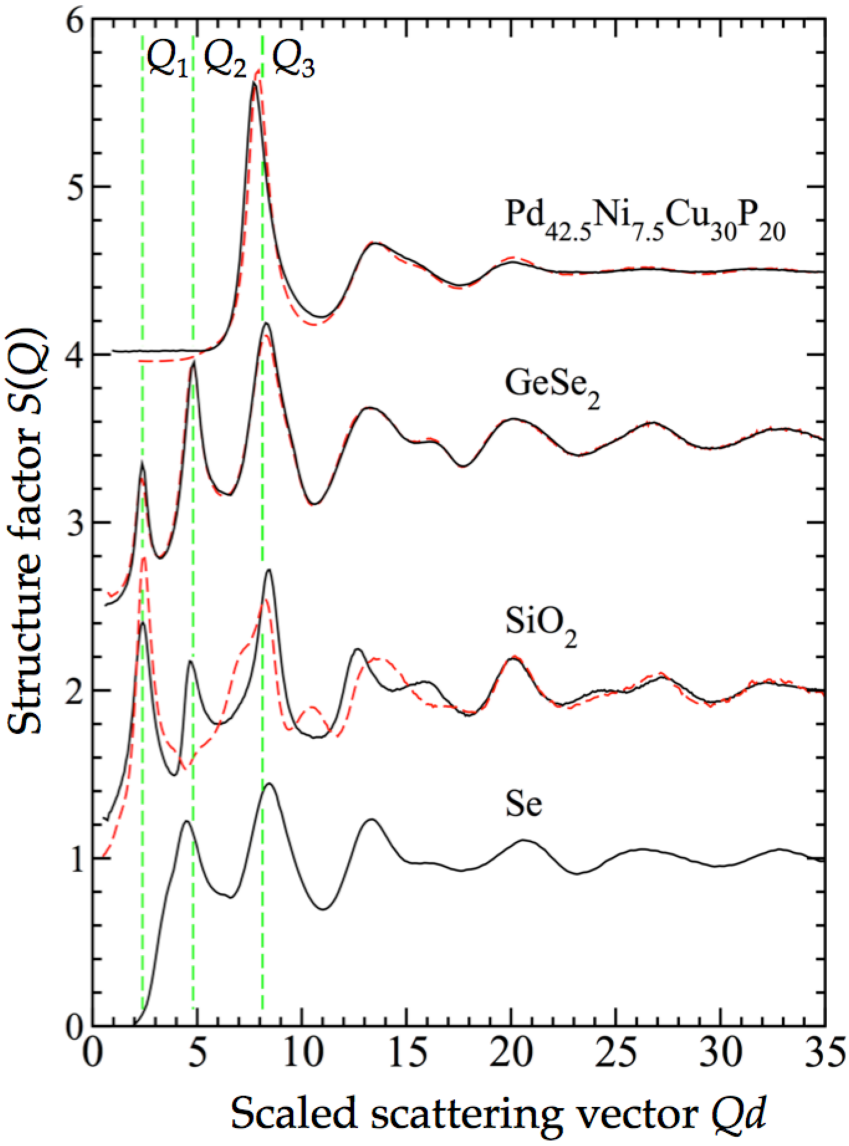

Figure 14: *Typical structure factors obtained by neutron diffraction (solid curves) or x-ray diffraction (broken curves) for various glasses as a function of the scaled scattering vector Q.d. The figure is adapted from [74].*

The low-*Q* region is usually dominated by the peak Q_1, referred to as "First Sharp Diffraction Peak" (FSDP), but several peaks or shoulders can coexist in chemically complex glasses. The features at low-*Q* values have attracted considerable attention as they are a characteristic of topological organization at the IRO (figure 15). If the low-*Q* feature at position Q_1 is isolated and Fourier transformed, it gives in *r*-space a decaying sine function with periodicity 2π / Q_1. The correlation length in real space of the decaying oscillations corresponds to the full half width maximum (FHWM) of the Q_1 peak, 2π / *FHWM,* giving typical values of 15-25 Å [75].

This feature is seen in a wide range of disordered systems, persisting even into the liquid state. Its intensity is highly sensitive to disorder (*e.g.*, in neutron bombarded SiO_2, the peak becomes weaker)

and exhibits anomalous behavior with pressure [76][77][78][79], temperature [80][81][82][83], pressure/temperature [84][85][86] and composition [87][88][89][90][91][92]. For instance, the peak intensity decreases with *P* and increases with *T* unlike the normal behavior of the other peaks. This anomalous *T*-dependence suggests a similar origin with the anomalous low-frequency, low-*T* vibrational properties. Relationships with system dynamics or fragility have been suggested [93].

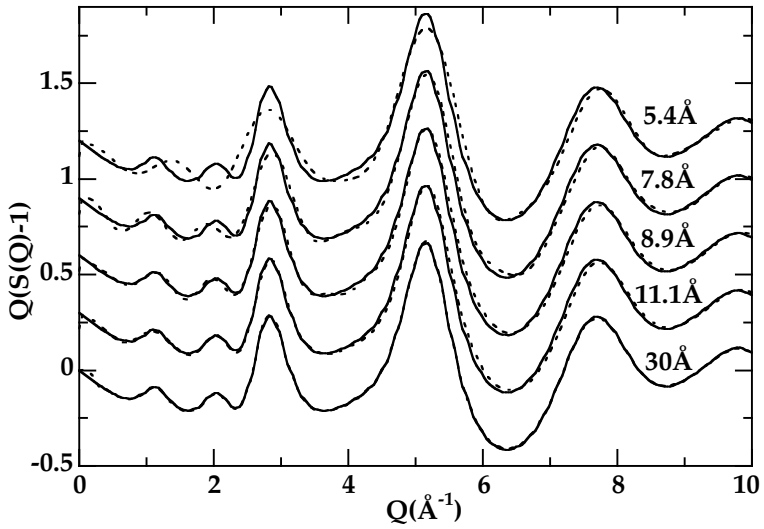

Figure 15: *Interference function, Q(S(Q)-1) of a $K_2TiSi_2O_7$ glass obtained by Fourier transformation of D(r) truncated at different values of r (dashed curves), chosen as even nodes of D(r). The experimental interference function (solid curve) is show as comparison. A value of r = 8.9 Å is necessary to fully reproduced the peaks, particularly the one at ~1.12 $Å^{-1}$.*

Whether included or not in the Fourier transformation, the low-*Q* feature is not related to a well-localized real-space feature in the correlation function, indicating that it corresponds to subtle organization at intermediate range. Difference function indicates that the main contribution usually comes from cation-cation correlation in the materials [80][94][50][95] though other authors suggest that the low-*Q* features appear primarily from density fluctuations and not concentration fluctuations [96].

Although essential to the understanding of IRO, the origin of the peaks present in this region remains controversial [97][98][99][100]. Several general explanations have been proposed for the universal origin of this peak.

6.1.1 Quasi-crystalline organization, quasi-Bragg peak or quasi-periodic arrangement

The position of these low-*Q* features in glasses, melts and simple liquids often appears at similar scattering vectors than strong Bragg peaks in compositionally equivalent crystals, suggesting a general correspondence. It was proposed that these peaks result from a broadening of the Bragg reflections corresponding to periodic anisotropic spacing of limited coherence length in real space [99][101][102][103], as structures in layers existing in chalcogenide glasses [81][82][77]. Liquids can also present these structures with intensities sometimes greater than in glasses. As it seems improbable that the liquid is more organized than the glass, the stronger intensity seems an indication that the layer models do not work [98]. However this intensity increase is not inevitably related with a more ordered structure [101][102][103]. It was suggested that, with the temperature increase, a relaxation of the constraints of the arrangements provokes an increase of the intra-layer correlations [81][82]. It was also considered that in glasses such as SiO_2, layer structure is improbable. Gaskell and Wallis [100] used various models developed for silica glass to show that they contain planar corrugated sheet structures associated with reasonably well-defined interplanar spacings similar to {111} planes of ß-cristobalite. They interpret these quasi-Bragg planes as the origin of the low-*Q* peak in SiO_2 glass. Since, in most glasses, the low-*Q* peak position corresponds closely to the position of a strong diffraction peak (often the lowest *Q* feature) of a corresponding crystalline phase, these similarities suggest a general explanation: the remaining of quasi-Bragg planes (distorted, imperfect and not necessarily “plane”) in the glasses similar to those presents in the related crystalline phases (figure 16). This model does not imply a layer glass structure and has connections with the Elliott’s model of interferences between the network and voids [104]. On the other hand, this model received the support of modeling [105] and is connected with liquid models [106][107]. Although not indicating a microcrystallite model, this interpretation emphasizes the important similarities between glasses and crystals in the organization at intermediate distances, which is also seen in the analysis of the first difference functions (see sections 6.4 & 6.5).

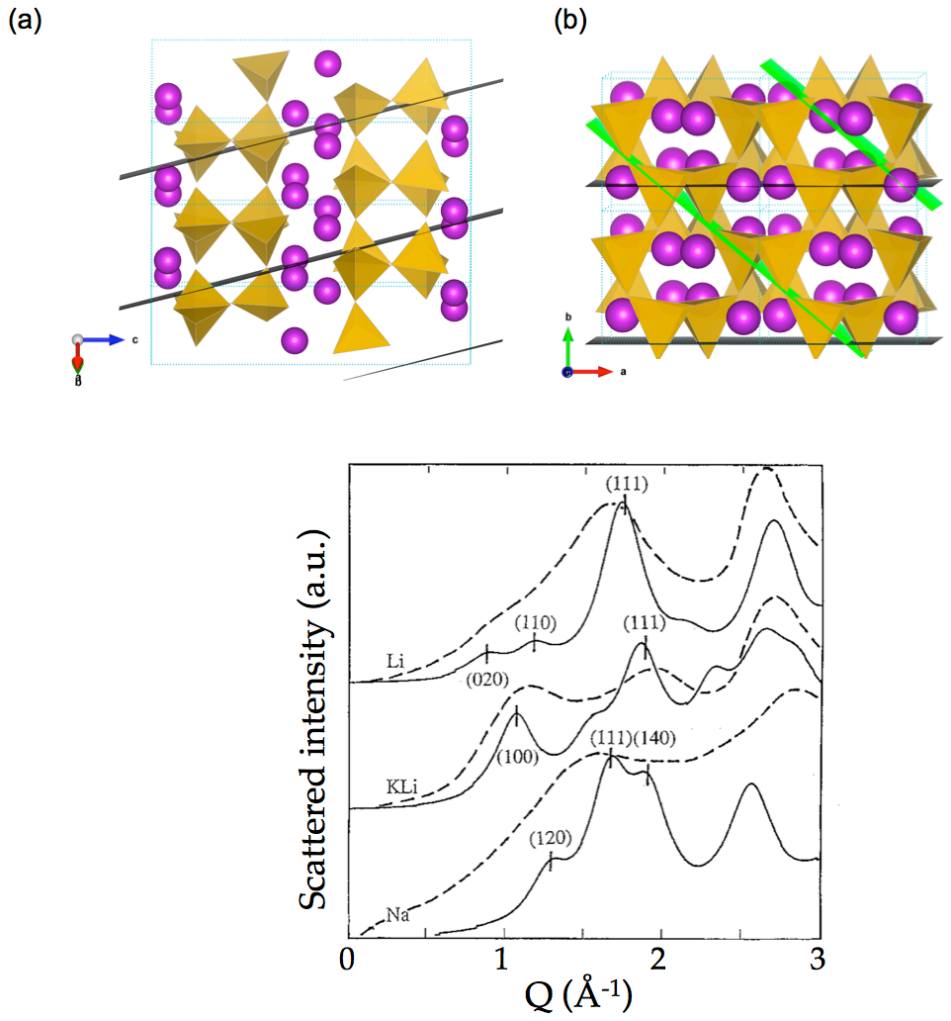

Figure 16: *(a) The structure of c-$Li_2Si_2O_5$ showing planes parallel to (111) in c-$Li_2Si_2O_5$ which are associated with the strong peak at 1.7-1.8 $Å^{-1}$ in (c), and can be associated with a similar feature in the corresponding glasses. (b) Projection of the structure along [100] showing corrugated planes of Si_2O_5 units. Planes parallel to (020) (horizontal, black) and (110) (inclined, green) are shown and are associated with the weak features at ~1 $Å^{-1}$ in (c). (c) Experimental neutron diffraction data (dashed curves) for disilicate glasses containing Li, K/Li and Na compared with simulated neutron diffraction calculated from the crystal structures (solid curves). The disorder is simulated by considering crystallites with 2 nm in size (not meaning a microcrystallite model). The figure is adapted from [108].*

6.1.2 Correlations between clusters and voids

Price and Moss [97] have suggested an explanation based on the packing of the basic structural or molecular units, which are observed in some tetrahedral molecular compounds [109]. One problem is that these clusters are ill-defined and the structure between these clusters is not specified. For liquids like CCl_4, the diffracted intensity is a sum of inter- and intra-molecular terms. The low-*Q* peak appears as a combination of a strongly *Q*-dependent intermolecular term (decreasing with *Q*) and the wing of the first "normal" diffraction peak (increasing with *Q*).

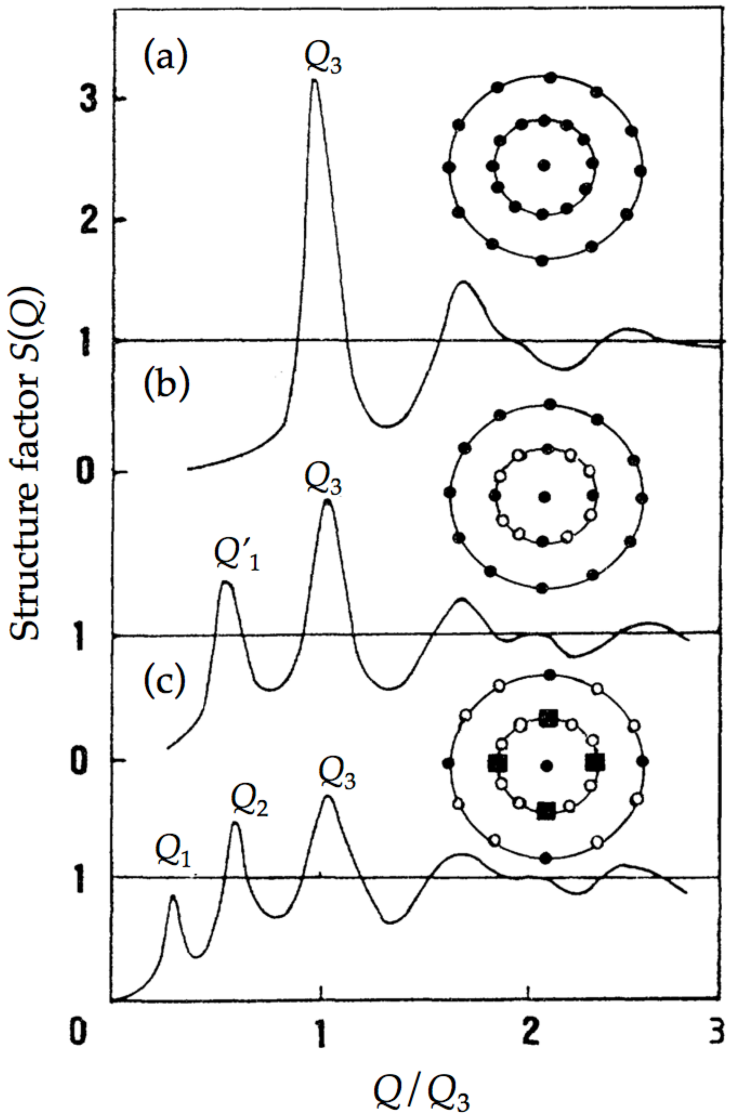

Figure 17: *Structure factors calculated for different models and normalized in Q to the position of the principal peak Q_3 determined by the nearest-neighbor distance. (a) A dense random packing structure (typical to metallic glasses), (b) a tetravalent structure (e.g. a-Si), and (c) a 4:2 structure (e.g., a-$GeSe_2$). Q_1 and Q'_1 correspond to FSDP and Q_2 to a second sharp diffraction peak with the same origin but different length scales. Filled circles in (b) and (c) are four-coordinated atoms, filled squares are two-coordinated atoms, and open circles are voids. The figure is adapted from [110][111]).*

Dixmier and Blétry [110][112][110] emphasized the role of holes for tetravalent vitreous structures which has been used by Elliott for a broader interpretation [98][113]. Elliott considers that these low-Q features derive from the chemical organization at short distance of the interstitial voids around cation-centered clusters which can be for example the SiO_4 tetrahedra in silicates (figure 17). It was shown that the lowest-*Q* and most intense peak originates from a rapidly decaying inter-cluster structure factor, *i.e*. simply an artifact resulting from the addition of a rapidly decreasing intra-

molecular form factor and the increasing inter-cluster structure factor at small Q [98]. It can be noted that, in the correlation functions, low atomic occupation zones around 5 Å are present [114]. The behavior in pressure, temperature and composition can be qualitatively explained by this model. For instance, the empty space within the structure reduces in volume as pressure is applied [113][115].

6.1.3 Correlations between, Q_1 and the reduced volume

Simplifying the Debye formula in equation (13) for a diatomic gas composed of two atoms of scattering power b, at a distance d from each other (figure 18.a), we obtain [116]:

$$S(Q) \propto \sum_{\alpha\beta} b_\alpha b_\beta \frac{\sin Qr_{\alpha\beta}}{Qr_{\alpha\beta}} = 2b^2\left(1+\frac{\sin Qd}{Qd}\right) \quad (35).$$

For $Q = 0$, the intensity is equal to $4b^2$ and after several oscillations tends to $2b^2$, i.e. the sum of the intensities diffracted by the two atoms of the molecule (figure 18.b). The function presents a succession of maxima and the first and highest diffraction maximum is obtained by setting the derivative of equation (35) with respect to ($Q.d$) to zero, which gives the Ehrenfest relation [117][116]:

$$Q = \frac{4\pi \sin\theta_m}{\lambda} = 1.23\left(\frac{2\pi}{d}\right) \quad (36).$$

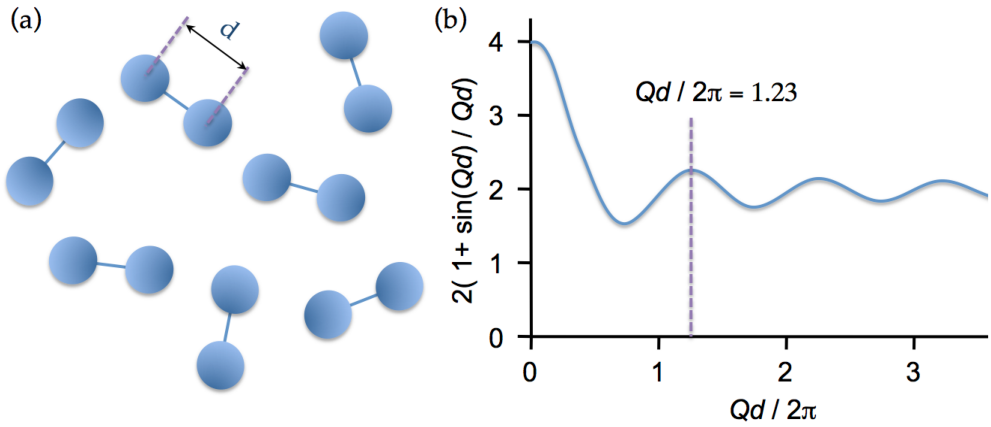

Figure 18: *(a) Representation of a gas composed of a diatomic molecule with an interatomic distance d. (b) The scattering power per molecule of a diatomic gas showing successive maxima.*

The position of this peak is associated with the principal diffraction peak (Q_3). As a consequence, the position Q_3 is inversely proportional to the mean atomic spacing and the third power of Q_3 scales inversely with the volume. In metallic glasses, it was used to determine the thermal expansion

coefficient by following the variation of Q_3 with temperature [118]. A power law relationship is proposed between the reverse of the principal peak position, $2\pi/Q_3$, and the glass volume $V_a = \rho_0 / (N_A M)$ for various metallic glasses [119]. The following relationship corresponds to the plot in figure 19:

$$Q_3 . V_a^{0.433} = 9.3 \pm 0.2 \quad (37).$$

The power of 0.433 is significantly different to 1/3 that would be expected for crystals and this has been interpreted as indicative of a fractal network with a fractal dimensionality of $(0.433)^{-1} = 2.31$ [119]. This correlation is convenient to understand the relative volume (density) change with pressure (see section 7.4.5).

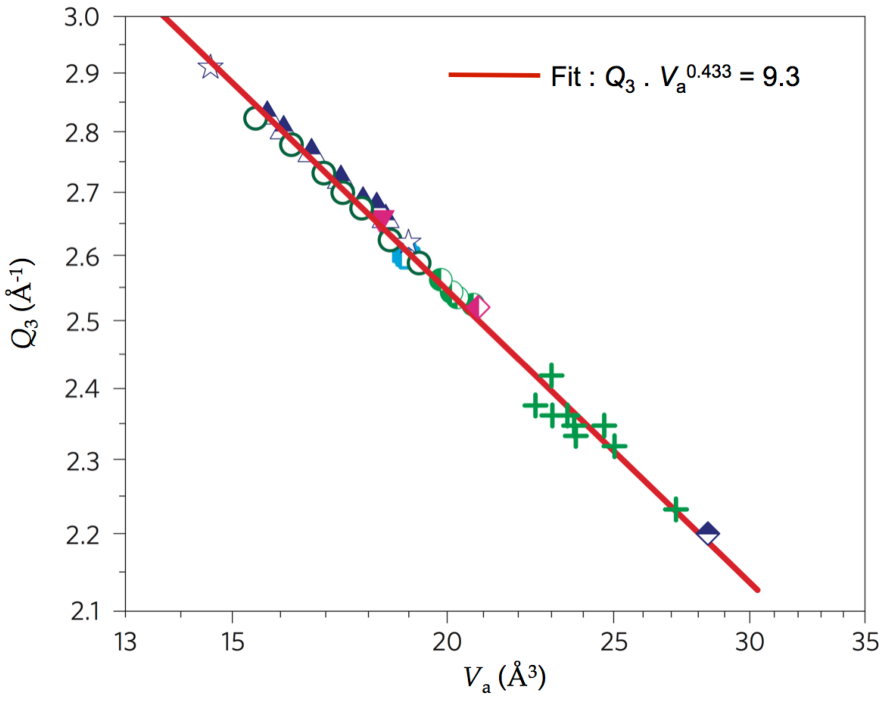

Figure 19: *Power law scaling of the peak Q_3 as a function of the atomic volume V_a. Both axis are in a logarithmic scale. The symbols represent the experimental points for various metallic glasses. The figure is adapted from [119].*

6.2 The polymeric network

Neutron diffraction is one of the most widely used methods to study the glass structure. In particular, the quantitative structural information on network formers and on the polymeric network can be obtained through the total correlation functions, in which the pairs associated with the glassy matrix are dominant. Pure silica and boron glasses have been widely studied by this method [42][120][121].

In phosphate glasses, it was possible to separate the contributions between the bridging oxygen anions and non-bridging oxygen anions around a phosphorus atom [25]. Such data provide constraints on the polymerization of the chains of PO_4 tetrahedra according to modifier oxide contents. Coupling ND and XRD with RMC allowed building structural models. These models showed for example that two alkalis present in glasses were distributed homogeneously [37]. The addition of salts in these glasses (for instance AgI [122]) leads to the expansion of the network, which promotes the formation of paths for ionic diffusion.

In borate glasses, large-*Q* values enable discrimination of two distances corresponding to three-fold coordinated boron (BO_3) boron and four-fold coordinated boron (BO_4) [39]. The BO_3/BO_4 ratio can be tracked according to the composition and excellent agreement is obtained with RMC experiments. Various studies have been conducted on borate or phosphate ionic glasses combining often ND, XRD and RMC modeling. It has been shown that IRO of the borate network decreases with an increase in doping salt concentration, and that the borate network forms a chain structure with AgI salt ions cross-linking these chains, while (Li, Na))(Cl,Br) salt ions enter the structural free volume and dilates the borate network [40].

NDIS was also used to extract the different PPDFs in the glassy network. In particular, in a $GeSe_2$ glass [94] [123], all pairs have been determined. The basic structural units are $GeSe_4$ tetrahedra arranged with both edge- and corner-sharing. The chemical order existing in oxide glasses is broken as homo-nuclear (homopolar) bonds have been evidenced by NDIS. Ion conductive chalcogenide glasses have been also extensively studied by this method to determine the interaction between the network and the added salts [124][125][126][127].

6.3 Cation sites in glasses

AXRD and NDIS are chemically selective methods, similar to EXAFS, but they have the advantage of being able to probe the structure with better accuracy [128] and larger distances (typically 10 Å). The use of materials isotopically substituted gives similar information to AXRD but for different elements, with a better experimental counting statistics and the ability to directly extract the cation-cation distances and coordination numbers.

The interest of the first difference function (see section 4.1) can be understood in figure 20 that shows the correlation functions determined in a complete study on a $K_2TiSi_2O_7$ glass with isotopic substitution of Ti [129]. In the first difference function, $G_{Ti\alpha}(r)$, we observe that Si-O and O-O correlations, having important weights, are eliminated. It appears then that the first layer of oxygen neighbors surrounding Ti can be deconvoluted into two distinct Ti-O distances at 1.68 and 1.96 Å,

which allows the unambiguous determination of the Ti site as a square-based pyramid. Contrary to EXAFS that shows a single distribution [130], the NDIS method is able to solve the two Ti-O distances, thanks to the wide available *Q*-range that gives a better real space resolution.

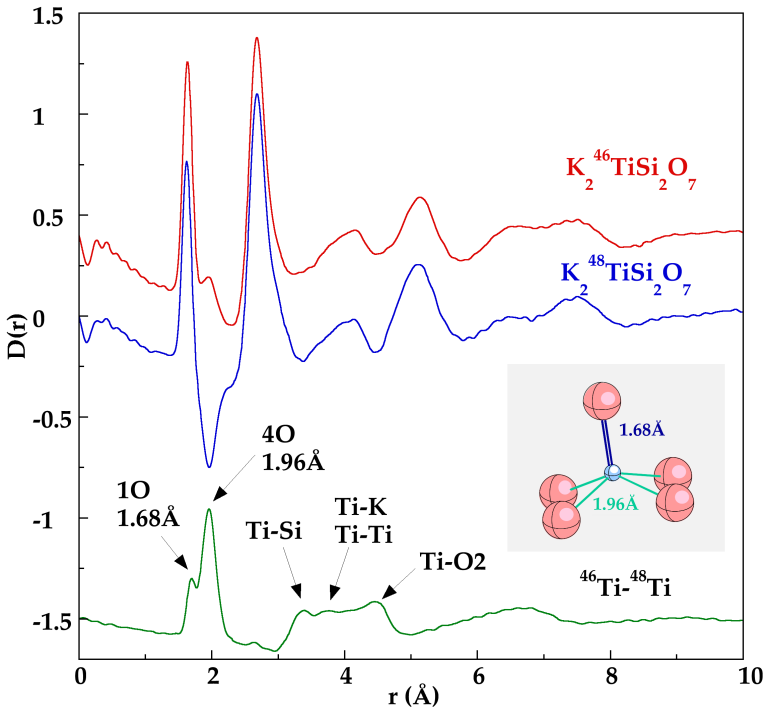

Figure 20: *Differential correlation functions obtained for a $K_2TiSi_2O_7$ glass containing ^{46}Ti isotopes (top curve) and ^{48}Ti isotopes (middle curve) compared with the first difference functions (^{46}Ti-^{48}Ti, lower curve) for Ti. Insert shows the TiO_5 site. The figure is adapted from [129].*

Some examples of first difference functions obtained by NDIS for cations in silicate and aluminosilicate glasses are presented in figure 21 [131]. Important similarities exist in these functions, regardless of the cation concentration (*e.g.*, 5.9 at.% for Ni in $Ca_2NiSi_3O_9$ [132] vs 14.3 at.% for Li in $LiAlSiO_4$ [133]) or the glassy matrix (*e.g.*, Li in a silicate, $Li_2Si_2O_5$ [134] or an aluminosilicate, $LiAlSiO_4$). Structural oscillations are discernible up to 10 Å in $G_{M\alpha}(r)$, functions, which indicates a cationic arrangement very well defined at medium range distances.

All $G_{M\alpha}(r)$ functions have a first sharp peak that results from the first shell of oxygen neighbors, indicating very well defined cationic sites in glasses. These sites present cation-oxygen distances and coordination numbers that may be similar to those observed in compositionally equivalent crystals, often with a low coordination number and a small radial disorder (Li at the center of a tetrahedral sites, Ti at the center of a pyramidal site). However, cations with higher field strength have lower coordination numbers in glasses compared to crystals. This is the case of Ca^{2+} (coordination number 8

in the $CaNiSi_2O_6$ crystal and coordination number 6 in the $Ca_2NiSi_3O_9$ glass) and Ni^{2+} (coordination number 6 in the $CaNiSi_2O_6$ crystal and coordination number 5 in the $Ca_2NiSi_3O_9$ glass).

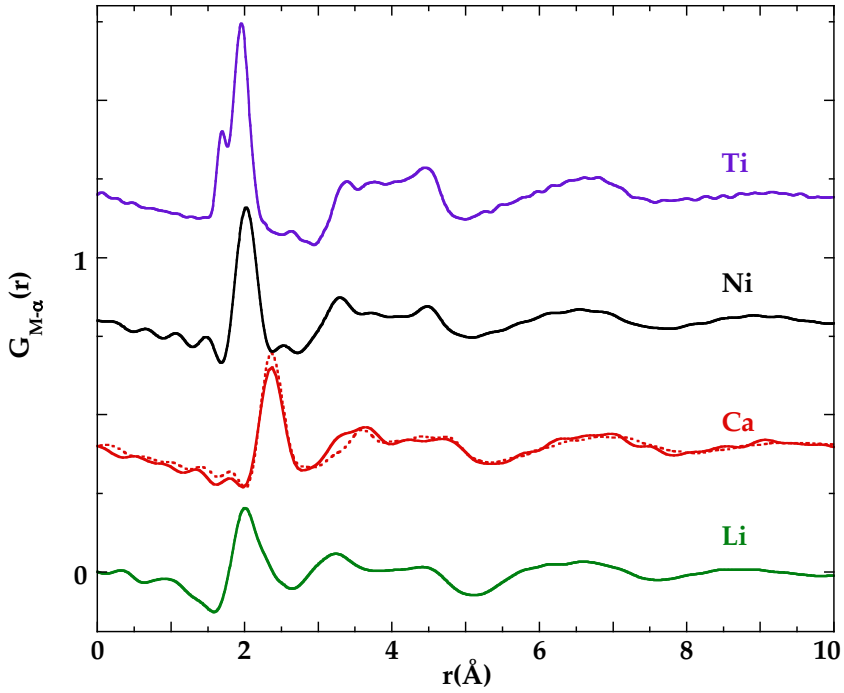

Figure 21: *Comparison of first difference functions, $G_{M-\alpha}(r)$ for Ti in $K_2TiSi_2O_7$, Ni and Ca in $Ca_2NiSi_3O_9$ (solid curve) and Ca in $CaSiO_3$ (dashed curve), Li in $LiAlSiO_4$ (from top to bottom). The figure is adapted from [131].*

The effects of radial disorder can also be quantified by NDIS. The main cation-oxygen correlations show standard deviations which are similar for all glasses, ~0.1 Å. Very well resolved site geometries are found by using extended *Q*-ranges. Good contrast of Ti isotopes allowed the deconvolution of two Ti-O distances separated by 0.3 Å in $K_2TiSi_2O_7$ glass [129]. Site distortions were also assessed in the case of Li [133] [134][135]. Lithium is always four-fold coordinated in the oxide glasses, but differences are observed. The local environment around Li in aluminosilicate glasses is strongly distorted (3 O at 2.02 Å and 1 O at 2.32 Å) with a stronger distortion and a larger average distance than for silicates. RMC modeling showed that the LiO_4 tetrahedra share edges with the AlO_4 tetrahedra in the $LiAlSiO_4$ glass, which involves short distances (Si, Al)- Li (~2.6-2.7 Å) and long Li-O distances. These distances and the Li site distortion in $LiAlSiO_4$ are related to the role of Li as charge compensator in aluminosilicates, unlike a network modifying role in silicates where LiO_4 and SiO_4 tetrahedra are sharing corners. These data replicate those observed in compositionally close crystals and show that the local geometry of the Li site reflects important differences in the structural organization at longer distance. Asymmetric

distribution also exists for Ca and Ni: the $G_{M\alpha}(r)$ function presents a broad contribution at large-*r* values, though an exact determination is difficult.

6.4 Cationic arrangement at medium range distances

Between 3 and 5 Å, all $G_{M\alpha}(r)$ functions present several contributions related to second and further neighbors (figure 21). These peaks are close to those observed in compositionally equivalent crystals, which indicate that the glass structure retains some structural features of crystals. However, the presence of contributions beyond 5 Å in crystals is contrary to a model of microcrystallites [136]. Contrary to crystals, there is a structural deficit around 5-6 Å for all the studied cations. Difference functions obtained by AXRD exhibit the same lack of correlations (*e.g*. for Sr in silicate glasses [137]).

Beyond 5 Å, large contributions centered at 7 and 9 Å are observed and are not comparable to the distances in crystals. The distance at 5 Å can therefore be regarded as the size limit of the structural organizations that are similar in crystals and glasses. However, a large order persists beyond 5 Å as can be found by calculating a second difference by NDIS or by MD calculations .

6.5 Non-homogeneous distribution of cations

Second-order difference functions (see section 4.1) have been obtained for Ti [129], Ni [132], Ca [138] and Li [134] in silicate glasses [139]. These functions reflect the distribution of cations in the glassy network and reveal significant similarities. Figure 22 shows the well-defined *M-M* correlation functions.

The presence of a first short cations-cation distance indicates a non homogenous distribution of these elements in the glass structure as a homogeneous distribution consisting of a compact arrangement of spheres would give a first cation-cation distance at ~6 Å ($R_{MM} = (6 \times 0.63 / \pi\rho_0 c_M)^{1/3}$). In $CaSiO_3$ glass, it was concluded that nearest neighbor Ca–Ca distances can be associated with edge-sharing six-fold coordinated Ca–O polyhedra [138]. In $Ca_2NiSi_3O_9$ glass, edge-sharing linkages are proposed between trigonal bipyramids for NiO_5 sites [132]. On the other hand, the nearest neighbor Ti-Ti distance indicates corner-sharing polyhedra, charge compensated by adjacent alkalis in $K_2TiSi_2O_7$ glass [129].

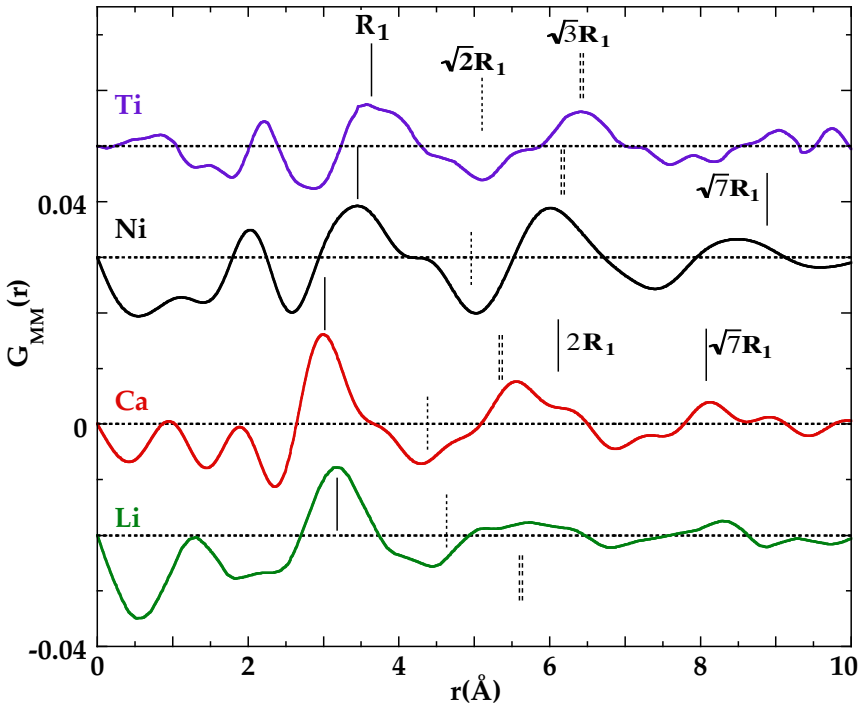

Figure 22: *Cation-cation distribution, $G_{MM}(r)$, in glasses obtained by Fourier transformation of the second difference functions for Ti in $K_2TiSi_2O_7$, Ni and Ca in $Ca_2NiSi_3O_9$ Ca, and Li in $LiAlSiO_4$ (From top to bottom). The figure is adapted from [139].*

The region extending up to 9-10 Å indicates a significant IRO. For all studied cations, if R_1 is the first *M-M* distance, the second one appears close to $\sqrt{3}\,R_1$ and the third close to $\sqrt{7}\,R_1$. In addition, the distance at $\sqrt{2}\,R_1$, which is characteristic of a tri-dimensional arrangement of polyhedra, is absent. These information reflect a cationic structural organization that has a strong bi-dimensional character in these glasses [138] and deviate from the completely random cationic arrangement as historically suggested by Warren [140]. Diffraction studies reveal a more ordered glass structure and the second difference function is the more convincing experimental evidence for clustering and percolation domains in silicate glass structure [141], consistent with the Modified Random Network model proposed by Greaves [142].

Similar *M-M* distances were observed by XRD in borate or silicate glasses containing heavy elements since the *M-M* pair dominates the experimental structure factors. These studies show correlations near 4.7 Å and 10 Å due to cation-cation pairs in silicate and borate glasses [143][144][145][146][147][148], on a very wide range of composition (3-65 mol% non-network former oxides). A study by AXRD at the Sr K-edge in silicate glasses has also shown Sr-Sr distances at 7 Å [137]. These heterogeneous structures are strengthened by numerical calculation such as MD [149] or RMC [150][151], which are able to reproduce cation-rich regions.

7. In situ high temperature / high pressure diffraction

Direct studies of the structure of glasses at high temperature and high pressure address important fundamental questions and are of great interest in different domains of research such as material science or geophysics.

Structural changes induced by temperature can govern important properties or phenomena: the glass transition occurs in the supercooled liquids and experimental and simulation studies are now consistent with subtle structural reorganization at intermediate range; nucleation/crystallization are events occurring into the supercooled state and *in situ* experiments can be useful to probe transient phases; glasses were studied as analogs for melts or liquids in industrial furnaces or for natural magmas, but significant structural differences can exist between glass and melt and a detailed understanding of such differences is important to understand the behavior and properties at high temperature. Since the first extensive diffraction studies of liquids by Waseda [152][153], important experimental developments have been obtained allowing investigation of very high temperature and increasing the accuracy of diffraction data.

The structure of liquid and amorphous materials at high pressure is crucial for geophysicist, interested in silicate melts relevant to earth and planetary sciences, but also to material scientists, wishing to obtain new materials having novel properties. *In situ* investigation is mandatory because pressure-induced modifications, such as coordination changes, are usually reversible.

7.1 High temperature experimental techniques

In a ND experiment, vanadium can be used as a resistive element since this material has mainly an incoherent scattering and gives negligible Bragg peaks. Using several sheets of vanadium as shielding, temperatures up to ~1200°C can be reached, just before softening of vanadium (figure 23.a). The advantage of such a furnace is that large sample volume can be used and measurements are carried out in high vacuum, minimizing statistical noise. Samples are contained in silica tube containers (e.g., for chalcogenide glasses) or in vanadium cells (e.g., for oxide glasses). Some commercial heating devices are available also in synchrotrons, providing controlled atmospheres. However, these furnaces give access to a limited range of temperature (<1500°C at best), which prevents the investigation of refractory materials or liquids melting at very high temperatures.

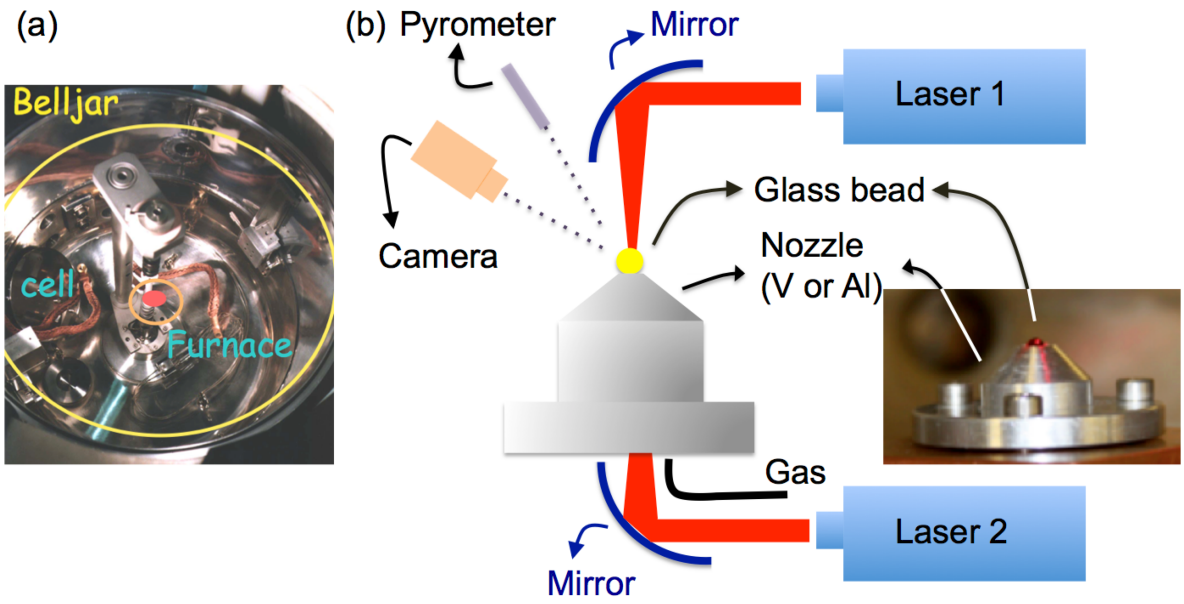

Figure 23: *(a) Picture of a vanadium furnace positioned inside the belljar of the 7C2 diffractometer at LLB (Saclay, France). (b) Schematic representation of an aerodynamic levitation setup used for diffraction experiments on a neutron source or a synchrotron. The glass sphere is levitated by a gas jet and heated using two lasers (from top and bottom to reduce thermal gradient) in a neutron source or a synchrotron.*

In large facilities (neutron sources or synchrotrons), levitation techniques became widely available during the past twenty years. Various experimental set-up to levitate a sample have been developed and were reviewed by Hennet [154]: electromagnetic levitation (EML) [155], electrostatic levitation [156], acoustic levitation [157] and gas flow either as gas film levitation [158] or aerodynamic levitation [159][160]. They are containerless methods useful to avoid heterogeneous nucleation from the cell walls or contamination between the sample and the container. The technique is also useful to extend the glass domain and explores the structure of glass compositions that are not quenchable in crucibles. The aerodynamic levitation (CNL, conical nozzle levitation) is the most popular tool [161] and consists in the levitation by a gas jet (usually argon) of a glass bead placed on a levitator composed of a water cooled conical nozzle (figure 23.b). Using a CO_2 or YAG laser heating, temperatures up to 3000 °C can be reached. Since nucleation is hindered due to the lack of interfaces with a container, supercooled liquids can be investigated few hundred degrees below the melting point. The sample bead is small (few mm in diameter) and only partially interacting with the incoming radiation, so a very low experimental and stable background is required. Using neutron sources, measurement times are typically several hours, requiring a good stability of the bead in the gas jet. Using synchrotrons, time resolved experiments are possible since diffractograms are acquired in a few ms with good counting statistics. A major drawback is the volatilization that can occur and experimenters must be attentive that the evaporation rate remains extremely low for the time scale of the experiment.

7.2 Case studies of temperature-induced modifications

7.2.1 Temperature evolution of the low-Q features

The FSDP (see section 6.1) in silica decreases in amplitude up to 1036 °C as expected [162][163] and as observed for the other peaks, with a normal Debye-Waller behavior. This is in contrast to the anomalous temperature dependence of the FSDP in oxide and chalcogenide glasses [98]. This normal behavior for silica is associated with the nearly zero thermal expansion coefficient and the dominant effect of thermal vibrations.

The position of the FSDP sometimes shifts to lower-Q values with increasing temperature as shown in figure 24a for a $15Na_2O$-$10CaO$-$75SiO_2$ glass (window glass composition) where the Q_1 peak position is shifted from 1.72 $Å^{-1}$ in the glass to ~1.62 $Å^{-1}$ in the liquid at 1000 °C [164]. But this does not necessarily imply an important change at intermediate range. Indeed, thermal expansion (decrease of the density) has a similar effect, since the third power of Q_1 scales inversely with the volume (see section 6.1.3).

The FSDP increases in intensity in glasses (*e.g.* As_2Se_3 up to the glass transition temperature, T_g [82]) and even persists in the liquid state. This is remarkably evident in alkali silicate melts. In $K_2Si_2O_5$, the first peak at Q_1 = 0.97 $Å^{-1}$ in the neutron structure factor presents drastic changes when temperature exceeds T_g (figure 24.b), with a marked increase in intensity [83]. RMC modeling indicates that this peak has important contributions from the partial functions involving oxygens (mainly BO-BO and Si-BO correlations while BO-NBO and Si-NBO have anti-phase contributions, where BO and NBO are bridging and non-bridging oxygen anions, respectively). This peak is related to the structural organization of the silicate network supporting the concept of cation channels.

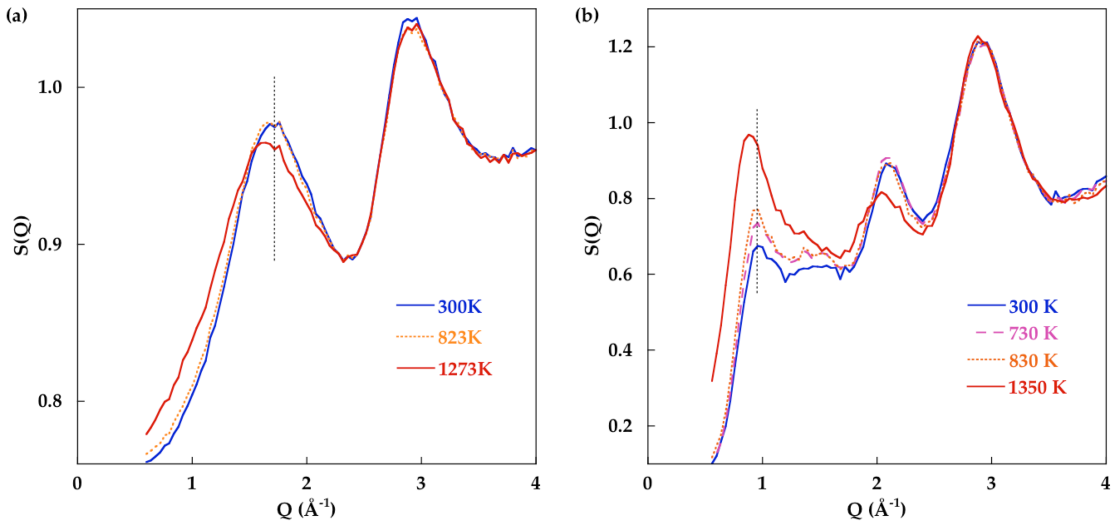

Figure 24: *(a) Evolution of the low-Q features in the neutron structure factors for a $15Na_2O$-10CaO-$75SiO_2$ glass/melt showing the shift of the first peak towards lower Q values. The figure is adapted from [164]. (b) Evolution of the low-Q features in the neutron structure factors for a $K_2Si_2O_5$ glass/melt showing the dramatic increase in the intensity of the first peak. Data were obtained using a Joule vanadium furnace on the 7C2 diffractometer at LLB (Saclay, france). The figure is adapted from [83].*

7.2.2 Evolution of short range order with temperature

The pioneering diffraction works using levitation were focused on investigation of refractory materials such as Al_2O_3 [165][160]. They revealed a decrease of the Al coordination number on melting. However the *Q*-range and counting statistics were very limited and the neutron/x-ray diffraction were recently revisited [29], taking advantage of the experimental advances and the development of new detectors. In this new study, they also combined their diffraction data with RMC modeling and they evidenced that AlO_4 and AlO_5 units dominate the melt, in an approximate ratio of 2:1. Al-O-Al connections are dominated by corner-sharing but a significant amount of edge-sharing exits (~16%).

The structure of $(CaO)_x(Al_2O_3)_{1-x}$ glasses and liquids have been widely studied by CNL [166][167][168][169]. Coupled with MD simulations [166][167], ND and XRD measurements indicate that Al is predominantly in tetrahedral position, with ~20% of fivefold coordinated Al at x=0.33 and fewer AlO_5 units as the CaO content decreases. Ca is predominantly sixfold coordinated in distorted octahedra but with a broad range of coordination environments (figure 25). Another study agrees with AlO_4 tetrahedra but found a lower coordination Ca-O number of ~5 in the melt [168]. This discrepancy results from different fitting criteria (cut-off distance for instance) and the difficulty in separating the Ca-O pair from the overlap of other contributions. It is also found that the structure for the eutectic liquid (64mol% CaO) does not change significantly with temperature between 1600 °C and 1970 °C.

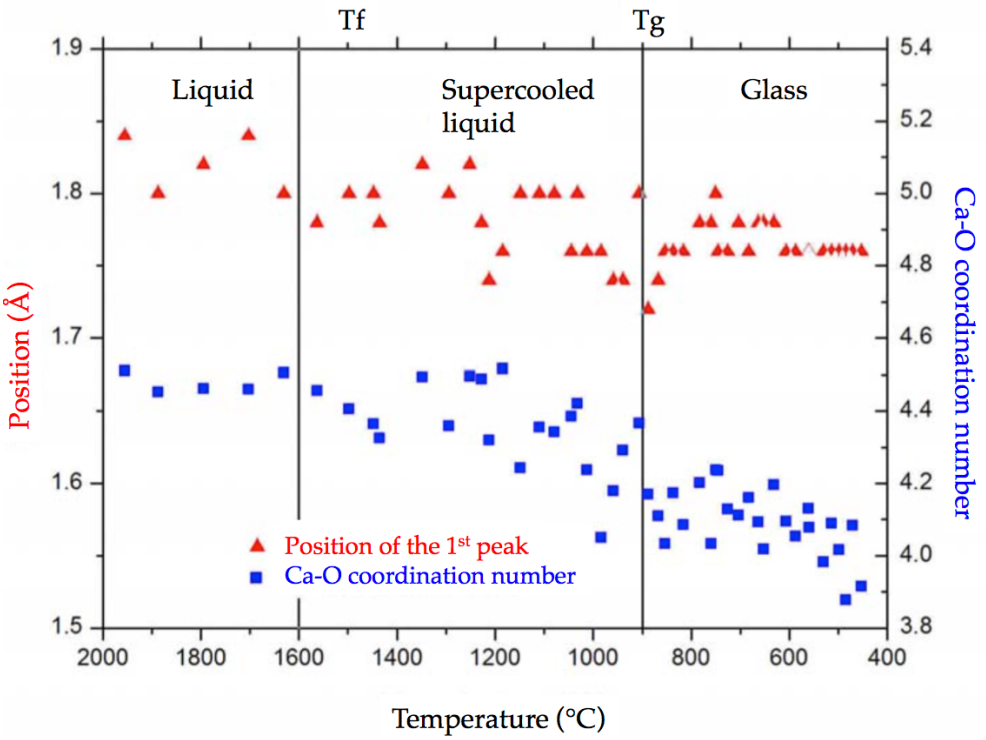

Figure 25: *Evolutions of the position of the Al-O peak in the pair distribution functions obtained by neutron and x-ray diffraction and the average Al-O coordination number upon cooling a liquid $CaAl_2O_4$ from 1900 °C. The figure is adapted from [169].*

HE-XRD has been used to investigate the liquid-liquid (L-L) transition between two forms of Y_2O_3-Al_2O_3 glass with low-density (LD) and high-density (HD) [170].They have associated structural changes with the onset of the L-L transformation that affects the Al and Y environment. The low and high density configurations calculated by MD simulations are shown in figure 26 and these models exhibit changes that match the difference in the experimental diffraction patterns. The main change in structure on liquid-liquid transition is not an Al coordination change but rather an increase in IRO seen as changes in the coordination polyhedra of Y^{3+} and in connectivity and arrangement of Al and Y polyhedra [171][172].

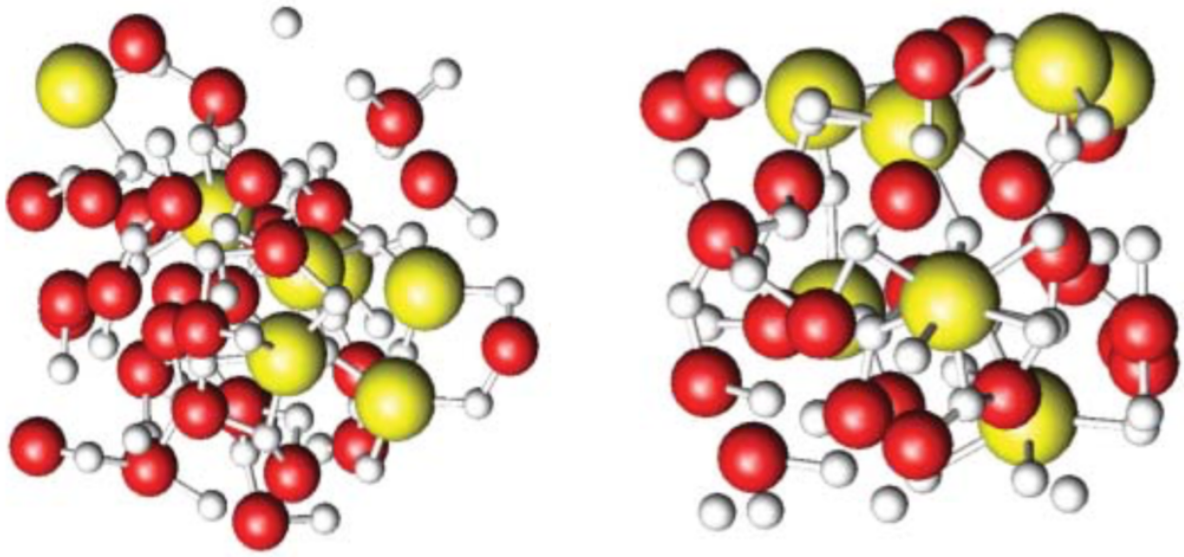

Figure 26: *Possible configurations for HD (left) and LD (right) glasses quenched from Y_2O_3–Al_2O_3 liquids obtained by RMC modeling of the neutron and x-ray diffraction data. Reprinted from [172], Copyright (2006), with permission from the Royal Society of Chemistry.*

AXRD has been rarely used to investigate glass/melt modifications. However, this technique has been combined with CNL to investigate the liquid structure of Y_2O_3 [173]. The Y-O coordination of 6-7 and the Y-Y coordination of ~12 imply the preservation of the close packing existing in the high-temperature polymporph. An unusually sharp main diffraction peak suggests a high degree of chemical order.

In alkali borate glasses, boron atoms can be present in triangular or tetrahedral sites. Using high resolution neutron diffraction, a detailed analysis of the first peak in real space reveals two different B-O nearest-neighbor distances at 1.37 Å and 1.47 Å, corresponding to BO_3 and BO_4 units, respectively (Swenson 1995). In pure B_2O_3 melt, the temperature-induced structural evolution has been described, using *in situ* neutron/x-ray diffraction, as a gradual opening of boroxol rings above T_g [174][121]. The structural changes of the local boron environment have also been quantified by ND in alkali borate glasses (figure 27), showing a partial conversion of BO_4 units present in the glass to BO_3 units in the melt [175][176]. This conversion implies the formation of non-bridging oxygens (NBOs) and the disappearance of bridging oxygens (BOs). Using NDIS (^{7}Li/^{6}Li isotopic substitution), the environment around the alkali atoms was also shown to vary (figure 28). The first Li-O distance in the $D_{Li\text{-}\alpha}(r)$ shortens by -0.02 Å in the liquid state, which is due to the shorter Li-NBO distance compared to the Li-BO ones. Therefore, a higher number of NBO is expected in the first coordination sphere of Li in liquids and the Li structural role evolves from charge compensator in the glass, associated with BO_4 units, to modifier in the melt, associated with NBOs [177].

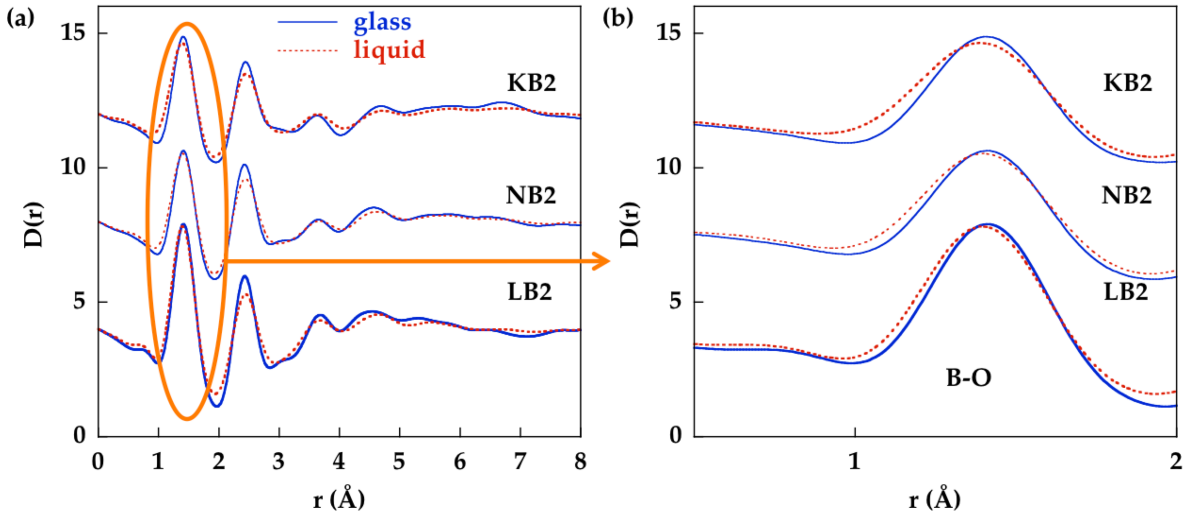

Figure 27: *(a) Differential correlation functions, D(r), for the glass (solid curves) and the liquid (dashed curves) for $K_2B_4O_7$ (KB2), $Na_2B_4O_7$ (NB2) and $Li_2B_4O_7$ (LB2), from top to bottom. (b) Low-r part of the D(r) functions showing the shit towards low-r values with increasing temperature. The figure is adapted from [175].*

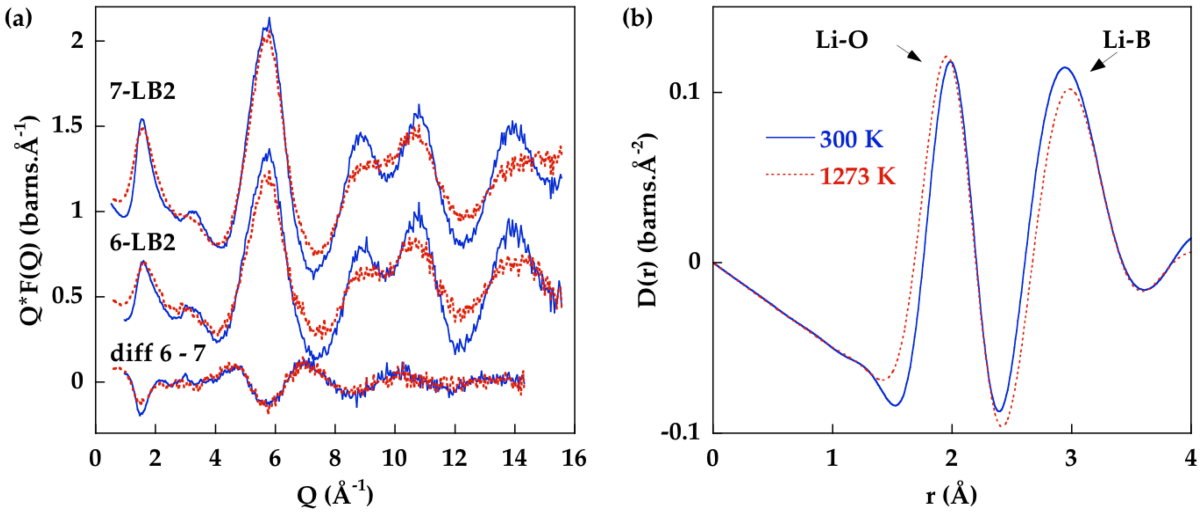

Figure 28: *(a) Interference functions, Q(S(Q) - 1), at 300K (solid curves) and at 1273K (dashed curves) for $Li_2B_4O_7$ containing 7Li isotopes (7LB2) and 6Li isotopes (6LB2) and first difference function (diff 6 – 7) extracting the Li-centered partial functions. (b) First difference function in real space showing the shift of the first Li-O bond distance towards lower r-values in the liquid state. The figure is adapted from [177].*

In SiO_2, the temperature has little effect on the SiO_4 tetrahedra that remain the main structural units in silicate melts, with a coefficient of thermal expansion of the Si-O bond estimated by ND at $(2.2 \pm 0.4) \times 10^{-6}$ K^{-1} [178]. The $D(r)$ function of silica shows a small decrease of the Si-O-Si mean bond angle and an expansion of the network between 5 and 9 Å (figure 29), but an important IRO persists in the liquid state [179].

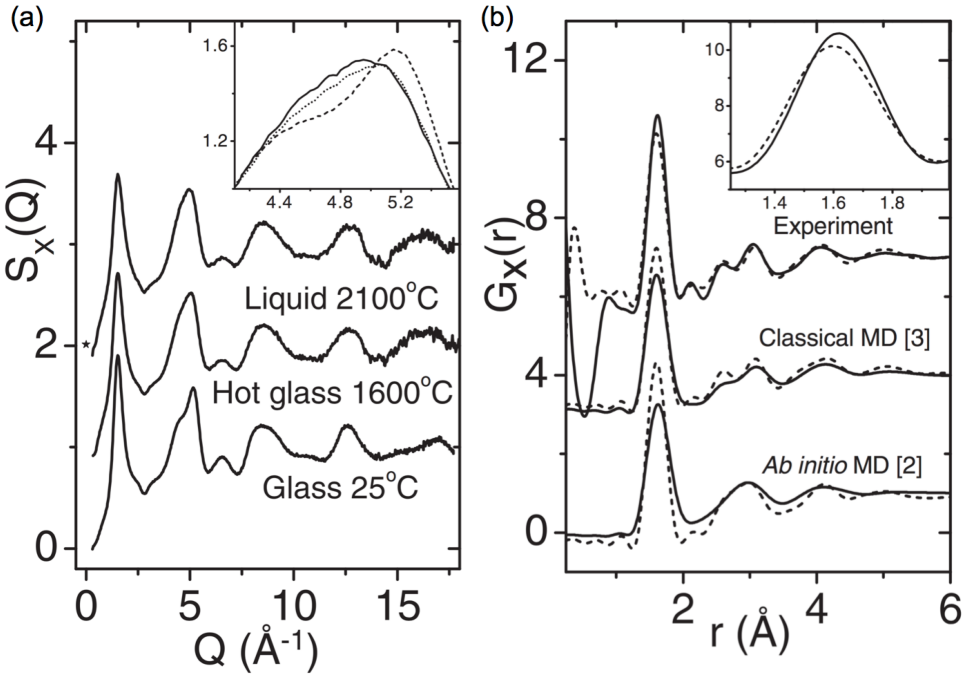

Figure 29: *(a) Experimental x-ray structure factors for SiO_2. Insert: second peak emphasizing the main changes between the glass (dotted curve) and the liquid (solid curve). (b) Top curves: experimental x-ray correlation functions for the glass (dashed curve) and the liquid (solid curve). Middle curves: classical MD simulations. Bottom curves: ab initio simulations. Insert: Shift in experimental data of the Si-O peak. Reprinted with permission from [179]. Copyright (2007) by the American Physical Society.*

In silicate glasses, substantial changes in cation coordination number are important in order to understand melt properties such as melt/crystal partitioning, transport, ionic conduction … In the binary MgO-SiO_2 system, the average Mg-O coordination numbers decrease on cooling from ~5.2 in the liquid to 4.5 in the glass, using *in situ* XRD and RMC fitting [180]. This change in structure allows the authors to conclude that the distorted magnesium percolation domains occur in liquids with lower MgO contents compared to glasses. The structure of iron-bearing silicates glasses was measured using HE-XRD combined with laser-heated aerodynamic levitation [181]. The technique is particularly well-suited to investigate such liquids as certain compositions (Fe_2SiO_4) are not quenchable and their structure can only be studied *in situ*. The Gaussian fit of the correlation function indicates two Fe-O distances at 1.93 Å and 2.20 Å (figure 30), corresponding to FeO_4 and FeO_6 polyhedra, respectively. The coexistence of these two states has important implications for the partitioning behavior of iron or transport of magmas.

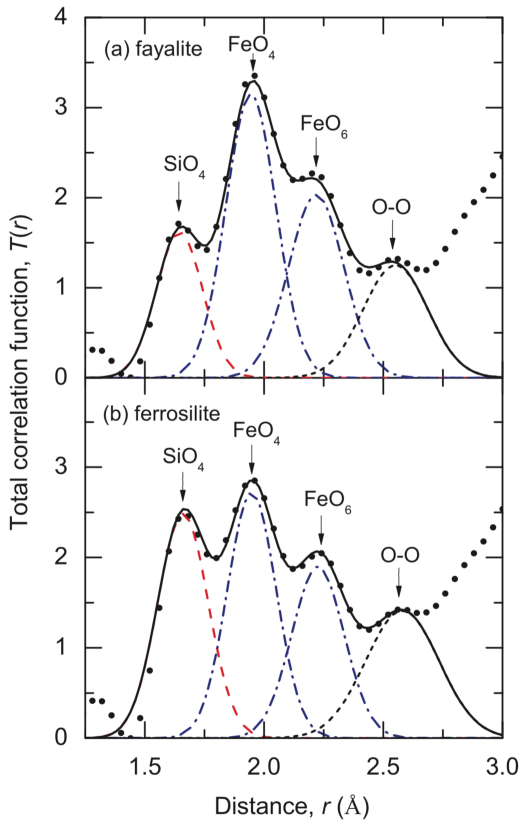

Figure 30: *Neutron total distribution functions, T(r) (black circles), for (a) liquid fayalite Fe_2SiO_4 and (b) liquid ferrosilite $FeSiO_3$ [181]. The long dashed curve is the Gaussian fit of the Si-O peak. The chained curves are the Gaussian fits of the first and second Fe-O peaks, due to FeO_4 tetrahedra and FeO_6 octahedra, respectively. The short dashed curve is the approximate contribution for the O-O pair correlation. The solid curve is the sum of the fitted Gaussians. Reprinted with permission from [181]. Copyright (2013) by the American Physical Society.*

7.2.3 Evolution of intermediate range order with temperature

XRD measurements were performed on aerodynamically levitated $CaSiO_3$ droplets [182]. When cooled, the presence of isobestic points is observed on the correlation functions (figure 31), reproduced by MD simulations, which are used to characterize the polymerization process. A linear behavior is evidenced in the melt while a rapid growth is observed just above T_g and near $1.2T_g$. The MD simulations show more edge-shared polyhedra and fewer corner-shared polyhedra in the glass model than the liquid one. Local structural information on the Ca environment has been extracted from NDIS experiments using CNL [183]. A decrease of the intensity of the first Ca-O bond peak at 2.42 Å is observed in the liquid compared to the glass, which is attributed to the distortion of polyhedra. There is also a decrease in the average coordination number for Ca or a redistribution of Ca-O bond lengths to longer distances in the melt.

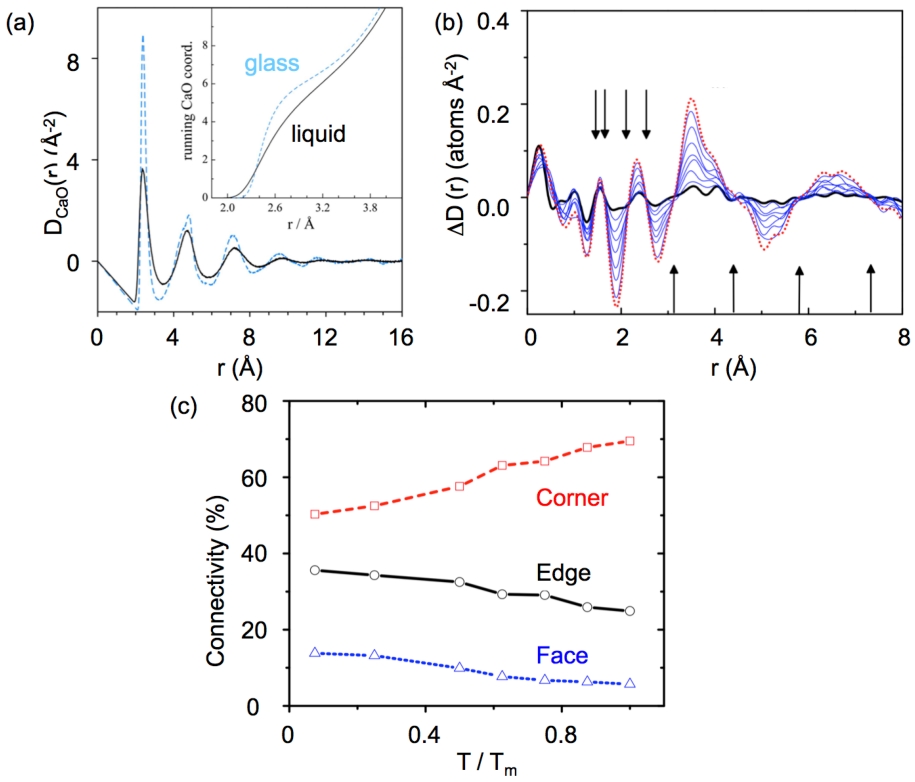

Figure 31: *(a) NDIS data showing the Ca-O partial distribution function, $D_{CaO}(r)$ (solid curve), for the liquid $CaSiO_3$ compared with the MD simulation for the glass (dashed curve) and liquid (solid curve). The insert presents the Ca-O running coordination number determined by MD simulations. Reprinted with permission from [183]. Copyright (2012) American Chemical Society. (b) Difference of the x-ray correlation function, $\Delta D(r) = D_T(r) - D_0(r)$, where the highest temperature $D_0(r)$ at 1900 °C has been subtracted. The isobestic points are marked with arrows. The figure is adapted from [182]. (c) Changes in the connectivity between Ca polyhedra for the liquid/glass MD models of $CaSiO_3$ as a function of temperature. Reprinted with permission from [182]. Copyright (2010) by the American Physical Society.*

The structure of metallic melts have been mainly studied using the EML environment, from the liquid state to a high undercooling [184]. In Ni, Zr and Fe metallic melts (figure 32), icosahedral short range order (ISRO) has been evidenced though larger polytetrahedral aggregates (such as dodecahedra) are prevalent in the liquid state. This ISRO appears as a split peak of the second peak in $S(Q)$. It is present already above the melting temperature and becomes more pronounced in the undercooled metastable state. NDIS experiments were carried out on $Ni_{36}Zr_{64}$ alloys using Ni isotopic substitution (figure 33), which allowed the extraction of all the partial functions [185]. The EML is advantageous in the case of NDIS since large samples can be levitated, improving good counting statistics. These partials indicate a preference of Ni-Zr nearest neighbors suggesting a pronounced chemical SRO. A high nearest-neighbor coordination number of 13.9 is determined. In contrast to most melts of pure metals or of metallic alloys, ISRO was not observed in the $Ni_{36}Zr_{64}$ melts, which could result from the large difference of the atomic radii (R_{Zr} / R_{Ni} = 1.29). The CNL technique was also employed to measure NDIS for NiSi and $NiSi_2$ alloys [186]. Both alloys exhibit a strong tendency to

hetero-coordination within the first coordination shell. In particular, the tendency to form Si-Si covalent bonds with somewhat greater distances influences the atomic structure of the NiSi melts. The structure of complex metallic alloys has been recently investigated showing the development of the ISRO upon cooling [187][188], with important consequences for glass stability.

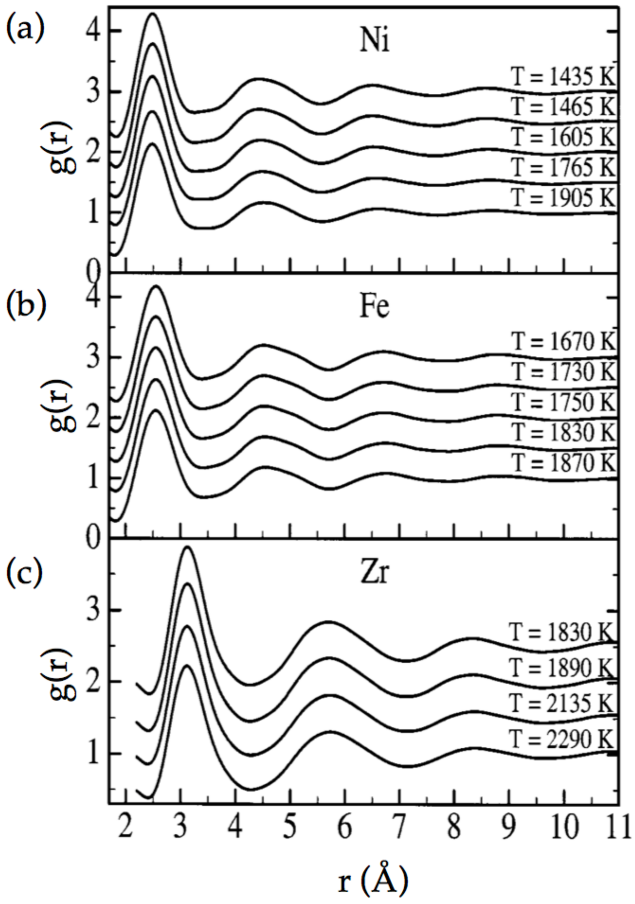

Figure 32: *Neutron diffraction structure factors at different temperatures for (a) Ni melts, (b) Fe melts and (c) Zr melts. The figure is adapted from [184].*

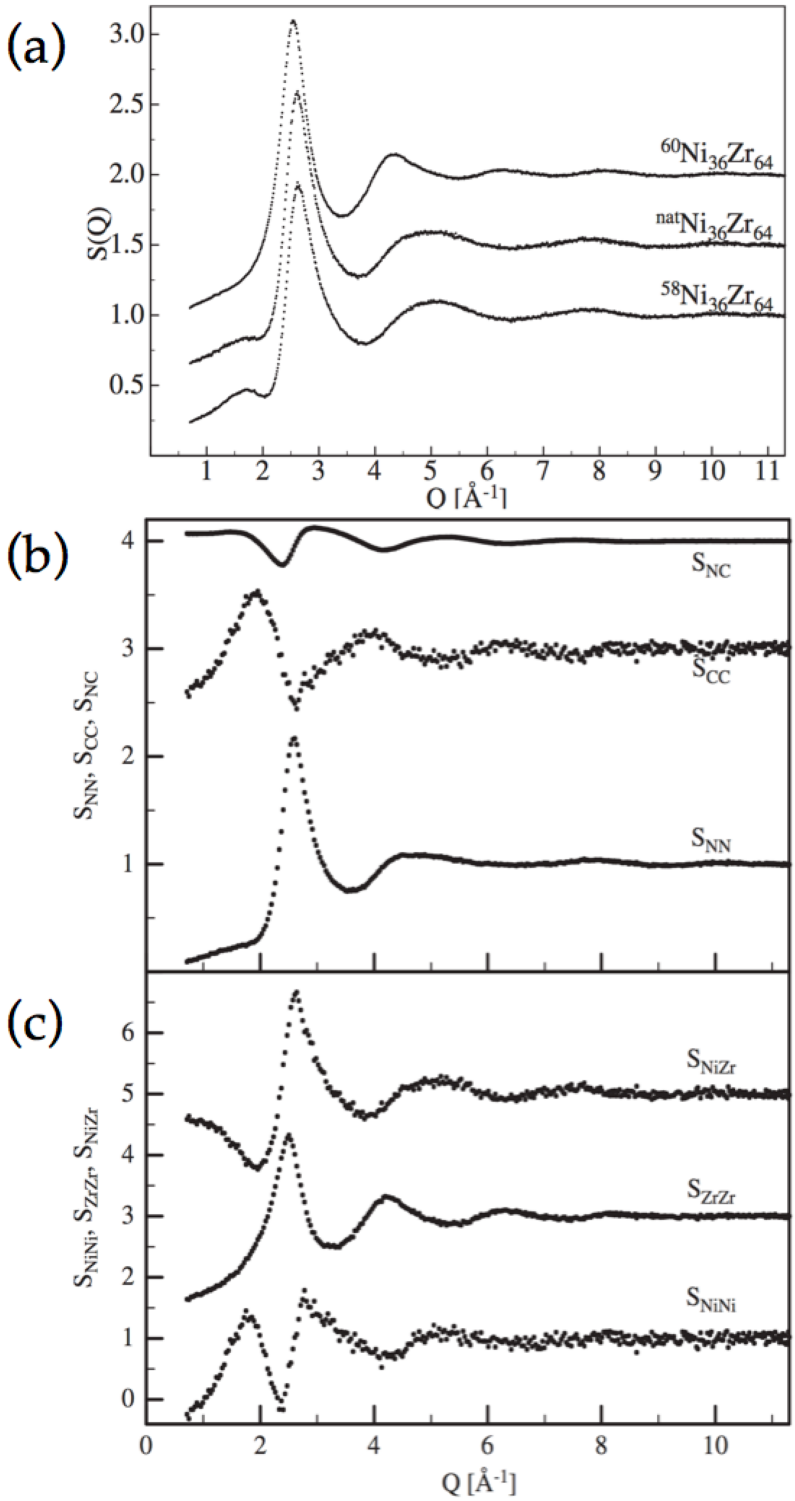

Figure 33: *(a) Neutron diffraction total structure factors for $^{58}Ni_{36}Zr_{64}$, $^{60}Ni_{36}Zr_{64}$, and $^{nat}Ni_{36}Zr_{64}$ at T = 1375 K. (b) Partial Bathia-Thornton and (c) partial Faber-Ziman structure factors. Reprinted with permission from [185]. Copyright (2009) by the American Physical Society.*

Rapid changes in the atomic structure of liquid tellurium has been shown by HE-XRD [189]. The structural evolution allows a better understanding of the density anomaly and the semiconductor-metal (SC-M) transition. Twofold and threefold local coordination coexist with a majority of the

formers which are slightly more present at lower temperature. The density maximum near the melting point reflects the temperature-dependent changes in chain lengths (longer chains at low *T*), ring distribution (larger rings at low *T*) and cavity volumes that are more abundant but with smaller sizes at low *T*. Cavities in the interchain regions at low temperatures explain the density minimum. The broadening of bond angle distribution at high temperatures is related to the SC-M transition.

ND and HE-XRD measurements have been carried out on TeX_4 (X=Cl, Br) liquids, in which chalcogens have covalent bonds and halide have ionic bonds [190]. Tellurium is present in tetrahedral coordination with Cl or Br. The intense FSDP suggest a pronounced intermediate range structure that consists of Te_2X_8 dimers, different to the monomeric gas and the tetrameric solid: Te_4X_{16} (solid) → Te_2X_8 (liquid) → TeX_4 (gas). A broader composition range of $Te_{1-x}Cl_x$ liquids, outside the glassy domains, has been investigated by ND [191]. Contrary to Cl-rich compositions, the ND structure factors of Te-rich liquid alloys exhibit a weak FSDP due to a chain network structure. As the Cl content increases, the structure progressively evolves from a chain network to a molecular-like behavior, the final member being Te_2Cl_8 dimers.

7.2.4 Thermodiffraction

Thermodiffraction is time-resolved diffraction acquisition at high temperatures. Diffractograms can be completed in up to 80° in 2.5 min acquisition times with ND [192] and in few ms with XRD. Such measurements are particularly useful to follow the real-time evolution of non-isothermal nucleation. In a bioactive glass $CaSiO_3$-$Ca_3(PO_4)_2$, the growth and disappearance of the successive phases can be easily visualized on a 2D map (figure 34.b), which is the projection of the 3D thermodiffractograms (figure 34.a). The crystallization sequence with the domains of the different crystalline phases is clearly identified.

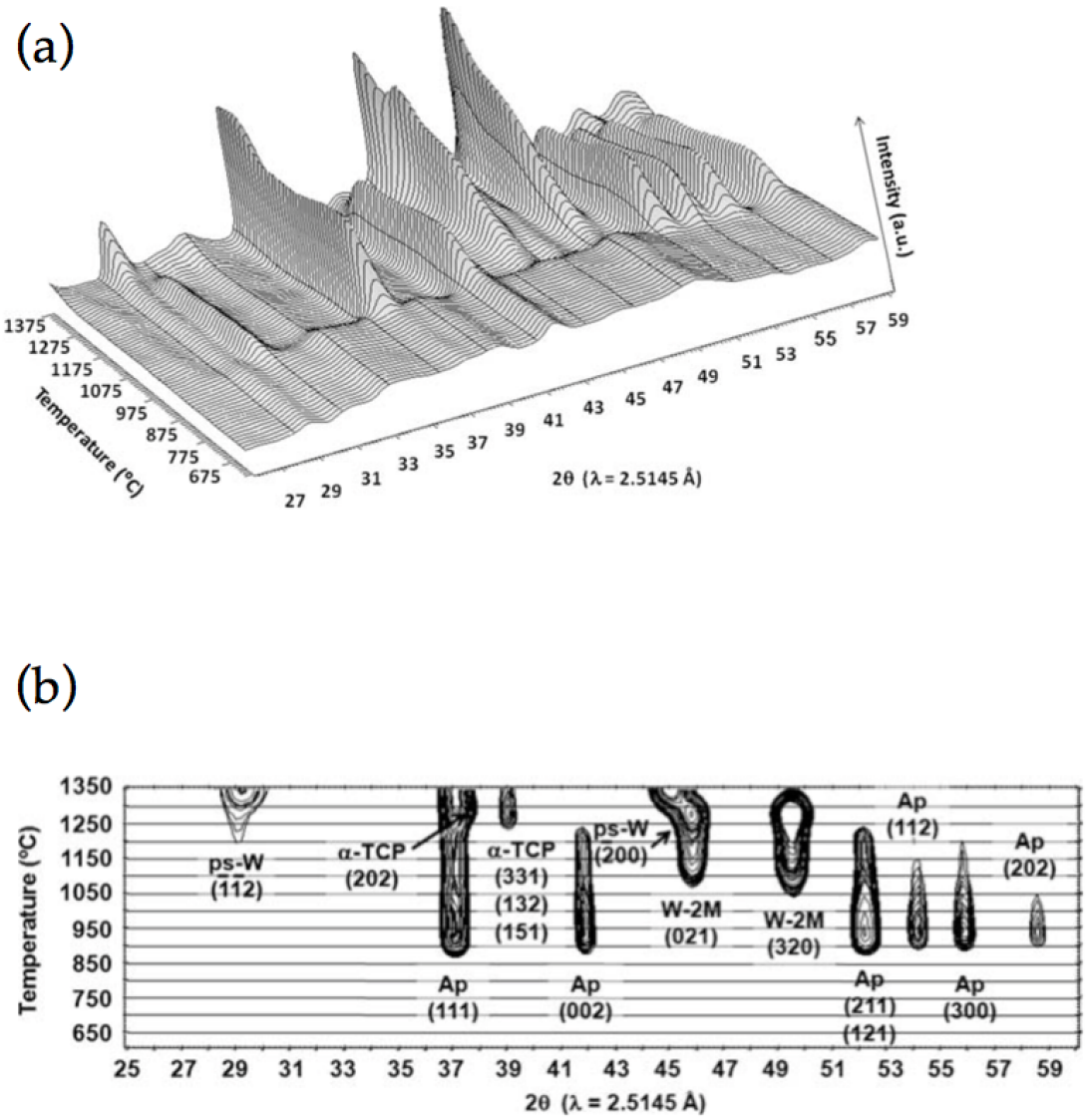

Figure 34: *(a) Evolution with time of non-isothermal crystallization of a $CaSiO_3$-$Ca_3(PO_4)_2$ glass showing neutron diffraction data collected from 600 to 1375 °C at 5 °C min^{-1}. (b) 2D projection of the thermodiffractograms in (a). The crystallization events (growth or collapse) are directly visualized (Ap, Ca-deficient apatite; W-2M, wollastonite-2M; ps-W, pseudowollastonite; α-TCP, α-tricalcium phosphate). Reprinted from [192], Copyright (2009), with permission from Elsevier.*

A complex crystallization sequence has been demonstrated by neutron thermodiffraction of the $Ag_x(Ge_{0.25}Se_{0.75})_{1-x}$ glasses with x = 15, 25 [193]. In agreement with the Ag-Ge-Se phase diagram, the primary crystals are the two stable phases, *i.e.*, Ag_8GeSe_6 and $GeSe_2$. However, *in situ* measurements highlight an additional phase (Ag_2GeSe_3), which is signaled by peaks located at 39° and 50.2° (figure 35). This phase is unstable and decomposes upon further heating, giving a new phase of $Ag_{10}Ge_3Se_{11}$ composition along with the stable $GeSe_2$ phase.

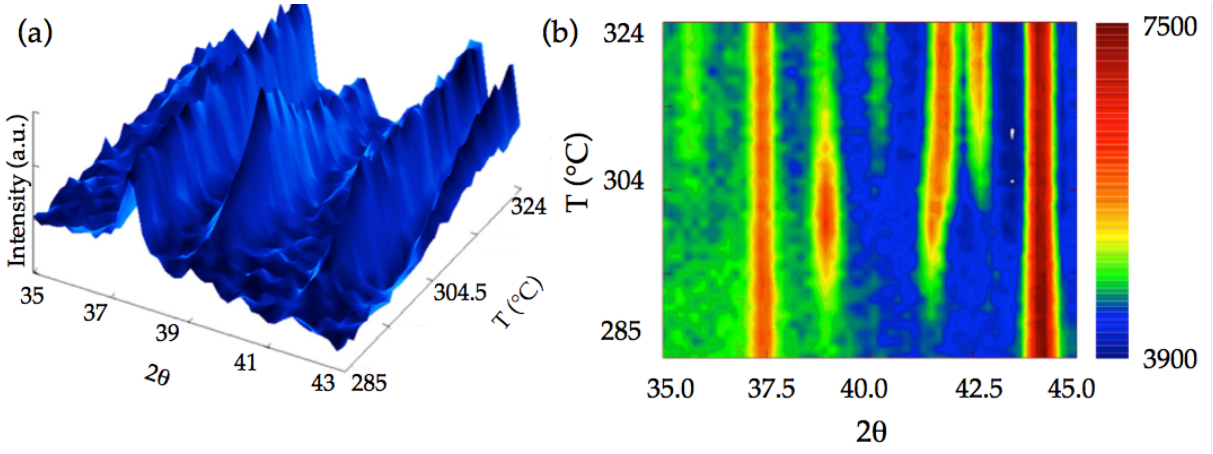

Figure 35: *(a) Neutron thermodiffractograms for the $Ag_{25}Ge_{18.75}Se_{56.25}$ glass. Graphs show a peak at 2θ = 39°, characteristic of the intermediate phase Ag_2GeSe_3, whose intensity appears at 285 °C and decreases above 320 °C. (b) 2D projection of the thermodiffractograms on (a) revealing the intermediate phase around 39°. The figure is adapted from [193].*

7.3 High pressure experimental techniques

Two general pressure cells are most currently used on large facilities: the diamond anvil cell (DAC) [194] and the large volume press [195].

In the DAC (figure 36.a), the sample is squeezed between the flat parallel culets of two opposed diamonds (single crystal, sometimes specially designed) and maintained between the diamond anvils by a hole drilled in a gasket. An inflated gas membrane transmits a mechanical force to the diamond table, pressing the diamonds together and increasing the pressure in the sample chamber. Resistance heating or laser heating can be used to generate high temperature. The advantage of DAC is that diamonds are transparent to x-rays. However, to achieve high pressure, the sample size is very small (~50 µm thick and <200 µm in diameter). Note that "large volume" DAC are currently developed on neutron source (SNPD beamline at Oak Ridge, USA) to investigate disordered materials.

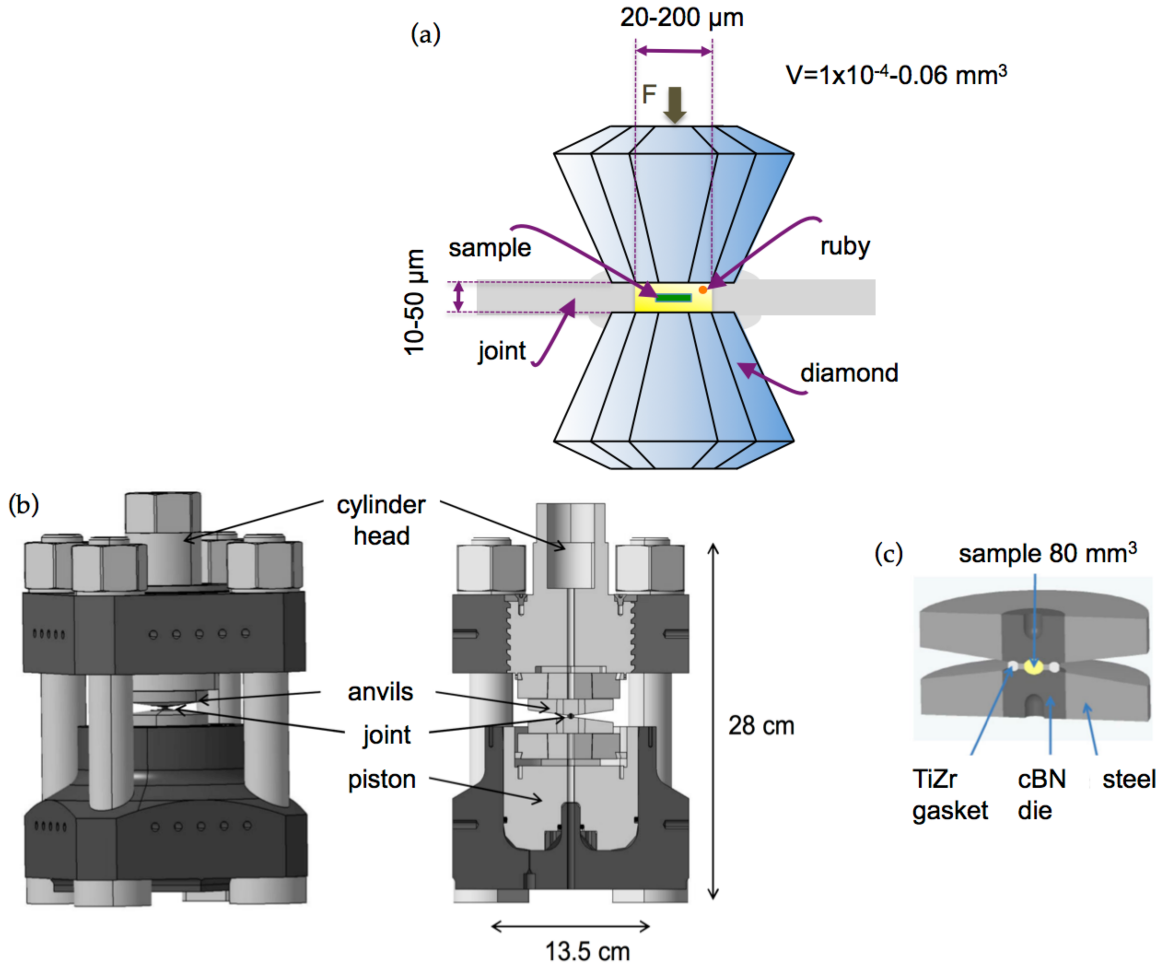

Figure 36: *(a) Illustration of diamond anvil cell. (b) Illustration of V4 large volume Paris-Edinburg press. On the cutting, the vertical access for the incident beam can be seen. The figure is adapted from [196]. (c) Cross-section of opposed anvils in the PE press. The figure is adapted from [197].*

Large volume apparatus (figure 36.b), Paris-Edinburgh (PE) press [198][199]), can be used for ND and XRD to achieve pressure up to 25 GPa. The PE press is composed of multi- or toroidal type anvils and a metal gasket, usually TiZr for ND as this alloy as almost null scattering (figure 36.c). A hydraulitic press connected to the piston by a capillary is used to generate the force. A major advantage of PE press is that large sample volume can be compressed compared to DAC: ~100 mm^3 for WC anvils, with pressure limited to ~10 GPa, and ~35 mm^3 for sintered diamond, achieving pressure up to 25 GPa [200]. As the incident beam passes through the cell assembly and the diffracted beam is usually detected in the gasket plane, the background scattering is important. Moreover, this background is pressure-dependent, resulting from the deformation of the gasket with pressure. The data correction is thus tedious as the background is hard to subtract, especially for weakly scattering samples. Another

limitation also existing for DAC is the angular exit aperture which can restrict the accessible maximum *Q*.

7.4 Case studies of pressure-induced modifications

A structural modification is usually the response to an applied pressure, modifying the properties of the material. Distinct amorphous states lead to the notion of polyamorphism or amorphous-amorphous (A-A) transition induced by pressure [201]. Considerable research using diffraction methods has been active in this topic in various glass systems, such as ice, oxides, chalcogenide or metallic alloys. The A-A transformation can be the viewable aspect of a liquid-liquid transition which could be present in the supercooled regime [202].

7.4.1 Amorphous forms of H_2O

The polyamorphism in water has been the subject of numerous *in situ* diffraction studies to investigate the apparent "first order-like" transition between the low density amorphous water (LDA) and the high density amorphous form (HDA). These two amorphous states have both a fully hydrogen-bonded tetrahedral network with HDA having a structure close to that of liquid water at high pressure and LDA a structure close to ice 1h (figure 13) [73]. The different structures are particularly evidenced in the $g_{OO}(r)$ partial function determined by NDIS and combined with EPSR (figure 37.a) [73]. The O-O coordination number increases from 3.7 in LDA to 5 in HDA indicating an additional fifth interstitial water molecule in HDA in the first neighbor shell, which gives a less ordered HDA structure compared to LDA. The pressure applied to transform LDA to HDA results in the collapse of the second neighbor shell of water molecules that eventually become interstitial, as demonstrated by spatial density functions obtained from EPSR models based on the diffraction data (figure 37.b) [203]. The interpenetrating network of water molecules stabilizes the HDA structure as this state can be recovered to ambient pressure.

A third denser amorphous form of water (Very High-Density Amorphous, VHDA) has been discovered and can be differentiated from HDA by its diffraction pattern: its structure factor has a sharp first peak shifted to higher *Q* values compared to *S*(*Q*) for HDA. This increase in the IRO is associated with a second interstitial water molecule [204], which is confirmed in the $g_{OO}(r)$ partial function [205].

As *in situ* studies are possible, neutron diffraction has been also used to follow the LDA → HDA transition using the PE pressure cell [206][207]. The structure factors exhibit a decreasing peak at

1.71 $Å^{-1}$ and a growing peak at 2.25 $Å^{-1}$, attributed to LDA and HDA, respectively. During the transition, changes in the position and height of the FSDP and in the position of the interstitial water molecule indicate distinct structural relaxation processes. A continuous series of metastable forms change the IRO during the transition and then structural relaxation in the second coordination shell of the LDA form appears [208][209].

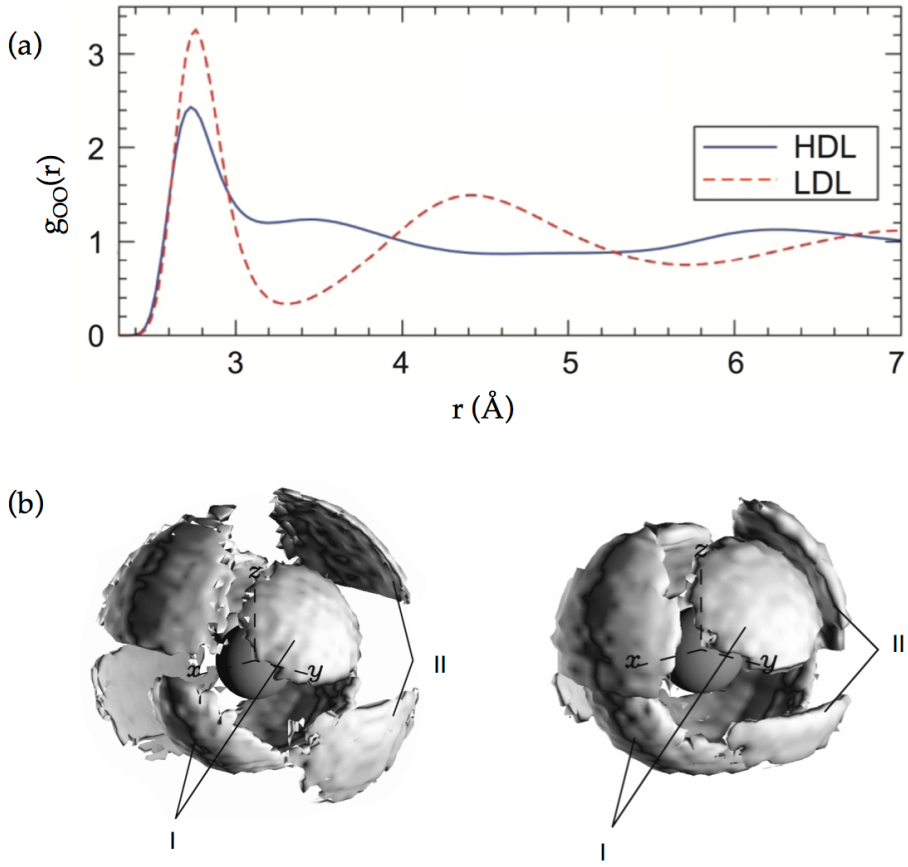

Figure 37: *(a) $g_{OO}(r)$ pair distribution functions for HDA and LDA as obtained by EPSR. The figure is adapted from [210]. (b) Three dimensional arrangements of the oxygen atoms around a water molecule (spatial distribution functions) for HDA and LDA. The pronounced lobes render the spatial density functions for the first (I) and second (II) shells of water molecules. showing the collapse of the second O-O shell in HAD (lobes II). Reprinted from [203], Copyright (2000), with permission from the American Physical Society.*

7.4.2 Density driven transformation in B_2O_3

B_2O_3 glass has been investigated by XRD up to 9.5 GPa [211] and by ND up to 17.5 GPa [212]. The position of the first peak in $S(Q)$ is linearly shifted towards high-Q values upon compression. This change indicates a reorganization of the IRO, interpreted as the break of boroxol rings below 3.5 GPa. Above 3.5 GPa, the real space function shows a change in boron coordination where BO_3 units are converted to BO_4 units. At 11-14 GPa, the decomposition of boroxol rings is achieved as seen in the

disappearance of the third peak in the distribution function and only the local boron conversion to BO_4 takes place at higher pressure.

7.4.3 Polyamorphism in SiO_2 and GeO_2

SiO_2 and GeO_2 are typical examples of 'strong', tetrahedral network glass-forming systems. The polyamorphim of these glasses correspond to an A-A transition from an open network structure based on corner-linked tetrahedra at low pressure, to a network dominated by SiO_6 or GeO_6 octahedra at high pressure.

These glasses were initially studied after decompression from high pressure allowing a permanent densification of the structure to be maintained [213][214][215]. Such permanently densified glasses show mainly structural changes at IRO with a decrease in the A-O and O-O distances (A=Si, Ge) due to rotation of the A-O-A bond angles and distortion of the AO_4 tetrahedra [213].

Coordination changes can only be addressed by *in situ* measurements as first demonstrated by x-ray absorption experiments [216]. The first *in situ* diffraction study has been reported using x-rays on SiO_2 up to 42 GPa and has revealed a gradual increase of the mean coordination number around Si, n_{Si}, from four to six above 10 GPa [217]. In the last decade, XRD and ND were widely used to investigated the pressure-induced structural modifications in SiO_2 (using XRD [218][219][220][221][222] and ND [223]) and GeO_2 (using XRD [76][224][225][226] and ND [76][227][228] including isotopic substitution of Ge ($^{nat}Ge/^{70}Ge/^{73}Ge$) [229]).

The structure factors for SiO_2 and GeO_2 are modified as the pressure is increased: the FSDP moves to higher-Q values and the principal peak becomes sharper in $S^N(Q)$ and more discernible in $S^X(Q)$. These changes indicate a decrease in IRO through the shrinkage and collapse of the open network structures.

The analysis of the distribution functions allows more information on the local order to be obtained. At low pressure, the tetrahedral structure is preserved and densification proceeds via an increase in the packing of AO_4 tetrahedra. The n_{Si} increases above four at $P > 10$ GPa while the Si-O bond length does not increase initially but present the appearance of a shoulder on its high-r side. The domain of coordination change is still debated but occurs mainly in the range 10-40 GPa. The tetrahedral-octahedral change occurs at lower pressure in GeO_2 by comparison with SiO_2 [216][230], with a n_{Ge} increase when $P > 5$ GPa [231]. The complete partial functions extracted from NDIS allowed the determination of the pressure dependence of the Ge-O-Ge bond angle [229]. As high coordinated AO_6 species are formed, the mean coordination number for O, n_O, also increases.

The transition domain is not necessarily a simple mixture of four- and six-fold coordinated sites and intermediate AO_5 species can coexist. However, the experimental evidence of such AO_5 species has not been unambiguously proven by diffraction methods, though MD simulations consistent with experimental data advocate, for instance, for SiO_5 units over the window P~20-45 GPa while SiO_6 units dominate when P $\gtrsim$ 32GPa [231]. Therefore, AO_5 units should play a key role in the mechanism of polyamorphism.

The oxygen-packing fraction η_o has been proposed to rationalize the changes in the coordination number [232][233]. The mean A–O coordination number $\bar{n}_A^O$ shows an interesting dependence with η_o for a large number of glassy and liquid network-forming materials (figure 38). BO_3 triangles and AO_4 tetrahedra show a plateau of stability ending at $\eta_o \simeq 0.44$ and at $\eta_o \simeq 0.59$, respectively. At higher packing fraction, the conversion to BO_4 or AlO_6 takes place. We can also note that SiO_2 and GeO_2 increase coordination at the same η_o. The upper limit of stability for AO_4 tetrahedra corresponds to the packing fraction for a random loose packing (RLP) of hard spheres, *i.e.* η_{RLP} = 0.55–0.60, and $\bar{n}_A^O$ increases rapidly as η_o approaches the expected packing fraction for a random close packing (RCP) of hard spheres, *i.e.* $\eta_{RCP} = 0.64$. At the latter packing, the transformation to an octahedral network is largely completed. Therefore network-forming motifs govern the topological ordering and can be predicted based on η_o behavior. The evolution of Q_1 position with pressure has a common behavior with η_o [74].

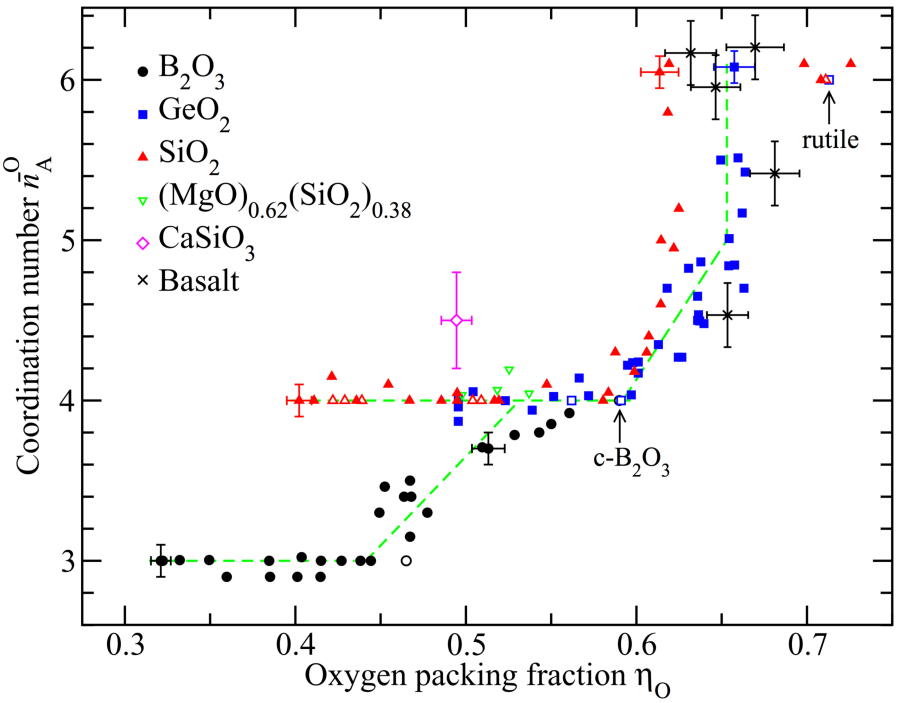

Figure 38: *Variation of the mean A–O coordination number as function of the oxygen-packing fraction η_o for oxide glasses and liquids under high pressure conditions [231].*

7.4.4 Chalcogenide glass $GeSe_2$

$GeSe_2$ is representative of chalcogenide glass in which the mechanism of pressure-driven network collapse can differ to that in oxide glasses due to the presence of edge-sharing $GeSe_4$ tetrahedra and homopolar bonds. This glass was investigated by *in situ* XRD [234] and NDIS [235][236]. NDIS is particularly useful since neutron and x-ray diffraction methods give essentially the same information due to similar scattering amplitudes for Ge and Se.

The FSDP is shifted to a larger-*Q* value upon compression and almost vanishes at 9.3 GPa. The principal peak also moves to a larger-*Q* value but its height increases, as the pressure dependence for GeO_2. These changes were interpreted as a loss of the IRO associated with the FSDP and a dominant extended-range ordering associated with the principal peak with increasing pressure, corresponding to the transformation from a 'strong' low-density to a 'fragile' high-density glass [231].

The first average peak in the pair distribution function, $\bar{r}$, slightly decreases with increasing density up to $P \sim 12.8$ GPa, while the average coordination number, $\bar{n}$, remains at 2.67. At higher densities, $\bar{r}$ and $\bar{n}$ increase to accommodate a larger number of nearest-neighbors. MD simulations indicate that, up to 8.2 GPa, the proportion of corner-sharing tetrahedra increases at the expense of edge-sharing tetrahedra, with a ratio from 1.3 to 1.7. According to MD simulations, homopolar bonds are largely present on the high coordinated Ge and Se atoms and play a key role in the density-driven structural transformations.

The pressure-induced structural modifications are continuous and occur on a broad pressure range, suggesting that densification is not an A-A transition. According to diffraction results, $GeSe_2$ glass keeps a semi-conducting behavior.

The structure of liquid $GeSe_2$ has also been studied under pressure [237], showing changes in the IRO, as reflected by changes in the FSDP on a narrow pressure range between 4.1 and 5.1 GPa. These modifications were interpreted as a continuous evolution from a two-dimensional to a three dimensional network.

7.4.5 Polyamorphism in metallic glasses

The coordination change associated with bond lengthening observed in oxide glasses (part 7.4.2 and 7.4.3) are not expected in non-directional, densely packed metallic glasses (MGs). Indeed, these materials have already a high coordination number (12-14) and are spatially compact. An *in situ* high-pressure XRD study on a $La_{75}Al_{25}$ MG shows a gradual and completely reversible compression (figure

39) [238]. Based on *ab initio* MD simulations and RMC fitting, changes in atomic size ratio and coordination number were identified as a conversion of prism-type coordination to icosahedral short-range order.

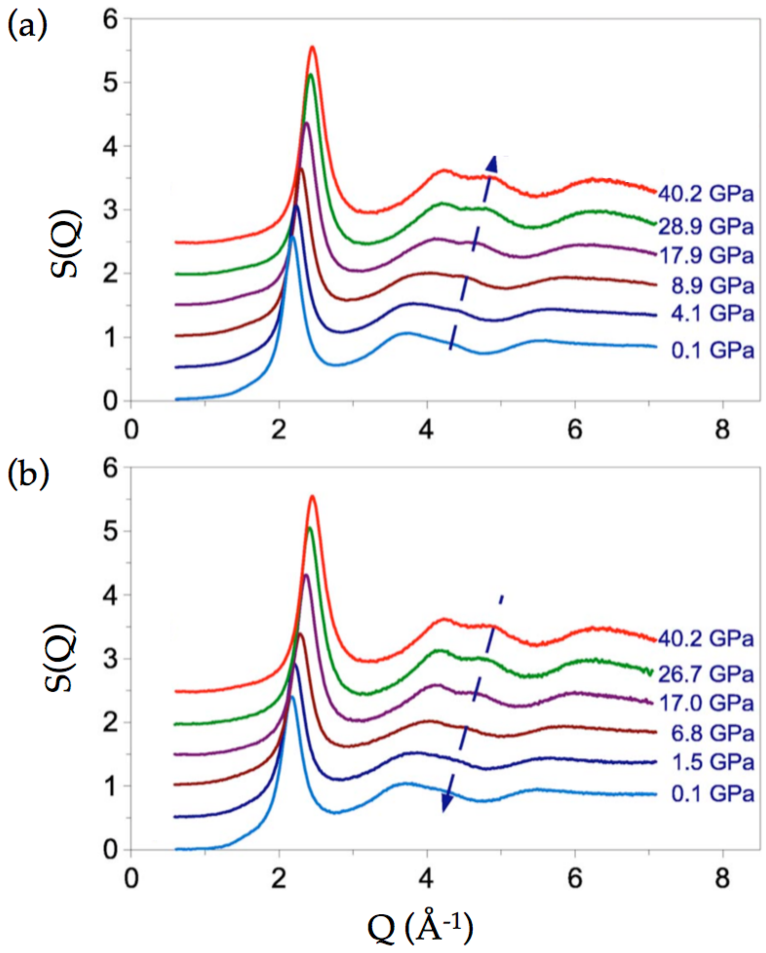

Figure 39: *x-ray structure factors for a $La_{75}Al_{25}$ metallic glass at different pressures upon (a) compression and (b) decompression showing the reversibility of the changes. The dashed arrow emphasizes a shoulder that becomes more apparent with increasing pressure. The figure is adapted from [238].*

However, evidences of pressure-induced polyamorphism were recently reported in various MGs mainly based on Ce-Al alloys (Ce_{32} $La_{32}Al_{16}Ni_5Cu_{15}$ [239], $Ce_{55}Al_{45}$ [240], $Ce_{75}Al_{25}$ [241], $Ce_{75}Al_{23}Si_2$ [241] and $Ce_{70}Al_{10}Ni_{10}Cu_{10}$ [84].), mostly using *in situ* high-pressure XRD measurements carried out on synchrotrons.

The position of the main peak Q_3 in the structure factors tracks with increasing pressure, showing significant shift towards high-Q values in some narrow pressure range (Figure 40). Similar to oxide or chalcogenide glasses, these changes are reversible when the pressure is released with an important hysteresis.

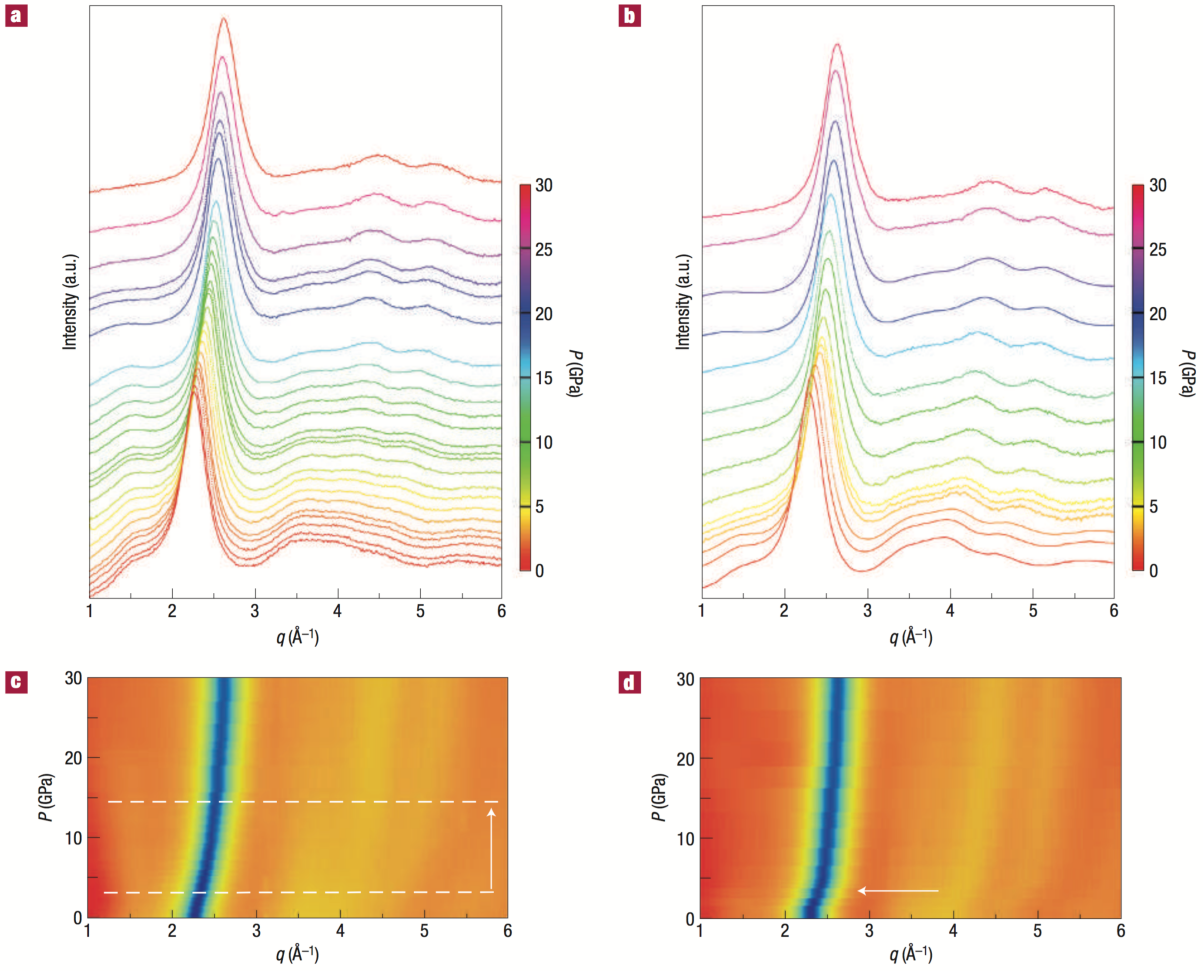

Figure 40: *Evolution of XRD patterns of a $Ce_{55}Al_{45}$ metallic glass in a diamond anvil cell upon (a) compression and (b) decompression. (c) The XRD intensity peak gradually shifts to high-Q values during compression in the pressure range 2.0-13.5 GPa. (d) During decompression, the arrow at ~2 GPa marks an abrupt shift towards low-Q values. Reprinted by permission from Macmillan Publishers Ltd: Nature [240], copyright (2007).*

The inverse position of the main diffraction peak, $2\pi/Q_3$, can be estimated using a Voigt line profile after subtracting baseline. As seen previously (part 6.1.3), $2\pi/Q_3$ can be correlated to the relative volume (density) change as a function of pressure. The plot of $2\pi/Q_3$ over pressure allows the observation of a clear transition between 1.5 and 5 GPa from a low-density state to a high-density state (figure 41). The transition starts from a LDA at low pressure, and goes through continuous densification ending with a HDA at high pressure. A large density difference is observed between the two polyamorphs. In figure 41, the volume collapse can be estimated with the 1/3 power law function giving about 8.6% volume reduction (2.9% in $2\pi/Q_3$).

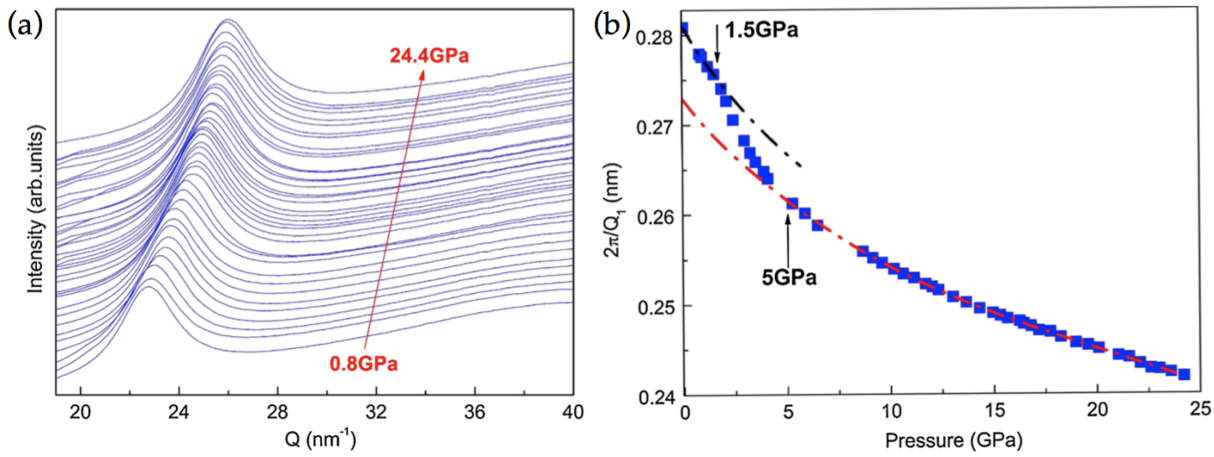

Figure 41: *(a) Evolution of XRD patterns of a $Ce_{75}Al_{45}$ metallic glass. (b) Inverse Q_3 positions as a function of pressure. The dashed black and red curves correspond to LDA and HDA, respectively. Reprinted with permission from [242]. Copyright (2010) by the American Physical Society.*

The suggested mechanism is an increase in Ce-Ce interactions leading to delocalization of some electrons in the 4f shells (from localized state $4f^1$ to delocalized state $4f^0$) under high pressure [240]. *Ab initio* MD simulations confirm this scenario which causes a splitting of the Ce-Ce nearest neighbor distance with one position having a significant bond shortening. Unlike the structural transition in ordinary amorphous materials [201], MGs exhibit and electronic polyamorphism. This large electronic configuration change has also been observed in other bulk metallic glasses (lanthanide-based MGs [86]) indicating that this mechanism is common. The A-A configuration change is not restricted to MGS having *f* electron: in Ca-Al MGs [79], a transfer of *s* electrons into *d* orbitals under pressure has been proposed to explain the A-A transition.

A liquid-liquid phase transition in the monatomic liquid metal cerium has also been reported using *in situ* high-*P*/high-*T* XRD experiments [243]. At a given pressure, a high-density liquid transforms to a low-density liquid with increasing temperature. Again, the origin of this transition is due to delocalization of *f* electrons. It was proposed that this transition reflects the liquid-liquid critical point in the Ce phase diagrams.

8. Conclusion and perspectives

In this chapter, we have introduced the fundamental concepts of the neutron and x-ray diffraction methods, emphasizing the difference and complementarity of the two techniques, the possibility to extract more structural information using contrast methods (neutron diffraction with isotopic substitution or anomalous diffraction) or the clear contribution of refinement methods (RMC, EPSR) or MD simulations. The synergism between diffraction data and simulation/modeling techniques is

now a routine procedure, beneficial for both tools and improving our current representation of the three-dimensional atomic arrangements in glasses. Oxide, chalcogenide or metallic glasses, among others, have been the subject of a tremendous number of investigation using neutron/x-ray diffraction and we have thus chosen some representative examples to illustrate the invaluable information that can be determined from diffraction data, leading to a deeper understanding of the glass structure in many amorphous systems. The structural response to pressure and temperature is often an experimental challenge, which has been successfully met by diffraction. Results using *in situ* high pressure/temperature set-ups hold great promise for elucidating the structural behavior in glasses, and thus the changes in their physico-chemical properties. Diffraction will continue to provide an excellent choice for future *in situ* high pressure/temperature studies by still pushing the experimental limits.

References

1. Zachariasen WH (1932) The atomic arrangement in glass. J Am Ceram Soc 54:3841–3851.
2. Warren BE (1934) The diffraction of x-rays in glass. Phys Rev B 45:657–661.
3. Warren BE Biscoe, J (1938) Fourier analysis of x-ray patterns of soda-silica glass. J Am Ceram Soc 21:259–265.
4. Fischer HE Barnes, AC.Salmon, PS (2006) Neutron and x-ray diffraction studies of liquids and glasses. Rep Prog Phys 69:233–299.
5. Chieux P (1978) Liquid structure investigation by neutron scattering. Neutron Diffr.
6. Squires GL (1978) Introduction to the theory of thermal neutron scattering. Cambridge University Press, Cambridge
7. Wright AC (1974) The structure of amorphous solids by x-ray and neutron diffraction. In: Adv. Struct. Res. Diffr. Methods. Pergamon Press, pp 1–84
8. Placzek G (1952) The scattering of neutrons by systems of heavy nuclei. Phys Rev 86:377–387.
9. Enderby JE (1968) Structure by neutrons. In: Phys. Simple Liq. North-Holland, Amsterdam, pp 612–644
10. Faber TE Ziman, JM (1965) A theory of the elctrical properties of liquid metals III. The resistivity of binary alloys. Phil Mag 11:153–157.
11. Sears VF (1992) Neutron scattering lengths and cross sections. Neutron News 3:26–37.
12. Dianoux AJ, Lander G (2003) Neutron data booklet, Old City Publishing. Philadelphia

13. Thompson A, Attwood D, Gullikson E, Howells M, Kim K-J, Kirz, Kortright J, Lindau I, Liu Y, Pianetta P, Robinson A, Scofield J, Underwood J, Willams G, Winick H (2009) x-ray data booklet, Lawrence Berkeley National Laboratory). Thompson, A.C., Berkeley

14. Waasmaier D, Kirfel A (1995) New analytical scattering-factor functions for free atoms and ions. Acta Crystallogr A 51:416–431. doi: 10.1107/S0108767394013292

15. Wilding MC, Benmore CJ (2006) Structure of Glasses and Melts. Rev Mineral Geochem 63:275–311. doi: 10.2138/rmg.2006.63.12

16. Bhatia AB, Thornton DE (1970) Structural Aspects of the Electrical Resistivity of Binary Alloys. Phys Rev B 2:3004–3012. doi: 10.1103/PhysRevB.2.3004

17. Salmon PS (2007) The structure of tetrahedral network glass forming systems at intermediate and extended length scales. J Phys Condens Matter 19:455208. doi: 10.1088/0953-8984/19/45/455208

18. Salmon PS, Martin RA, Mason PE, Cuello GJ (2005) Topological versus chemical order in network glasses at intermediate and extended length scales. Nature 435:75–78.

19. Salmon PS, Barnes AC, Martin RA, Cuello GJ (2007) Structure of glassy GeO2. J Phys Condens Matter 19:415110.

20. Debye P (1915) Zerstreuung von Röntgenstrahlen. Ann Phys 351:809–823. doi: 10.1002/andp.19153510606

21. Gaskell PH Saeed, A.Chieux, P.McKenzie, DR (1991) Neutron-scattering studies of the structure of highly tetrahedral amorphous diamondlike carbon. Phys Rev Lett 67:1286–1289.

22. Keen DA (2001) A comparison of various commonly used correlation functions for desribing total scattering. J Appl Cryst 34:172–175.

23. Cormier L Neuville, DR.Calas, G (2000) Structure and properties of low-silica calcium aluminosilicate glasses. J Non-Cryst Solids 274:110–114.

24. Petkov V Billinge, SJL.Shastri, SD.Himmel, B (2000) Polyhedral units and network connectivity in calcium aluminosilicate glasses from high-energy x-ray diffraction. Phys Rev Lett 85:3436–3439.

25. Hoppe U Walter, G.Kranold, R.Stachel, D (2000) Structural specifics of phosphate glasses probed by diffraction methods: a review. J Non-Cryst Solids 263&264:29–47.

26. Waser J, Schomaker V (1953) The Fourier Inversion of Diffraction Data. Rev Mod Phys 25:671–690. doi: 10.1103/RevModPhys.25.671

27. Lorch E (1969) Neutron diffraction by germania, silica and radiation-damaged silica glasses. J Phys C Solid St Phys 2:229–237.

28. Soper AK, Barney ER (2011) Extracting the pair distribution function from white-beam x-ray total scattering data. J Appl Cryst 44:714–726. doi: 10.1107/S0021889811021455

29. Skinner LB, Barnes AC, Salmon PS, Hennet L, Fischer HE, Benmore CJ, Kohara S, Weber JKR, Bytchkov A, Wilding MC, Parise JB, Farmer TO, Pozdnyakova I, Tumber SK, Ohara K (2013)

Joint diffraction and modeling approach to the structure of liquid alumina. Phys Rev B 87:24201.

30. Toby BH, Egami T (1992) Accuracy of pair distribution function analysis applied to crystalline and non-crystalline materials. Acta Crystallogr A 48:336–346. doi: 10.1107/S0108767391011327

31. Proffen T (2006) Analysis of Disordered Materials Using Total Scattering and the Atomic Pair Distribution Function. Rev Mineral Geochem 63:255–274. doi: 10.2138/rmg.2006.63.11

32. Hannon AC Howells, WS.Soper, AK (1990) ATLAS: a suite of programs for the analysis of time-of-flight neutron diffraction data from liquid and amorphous samples. Inst Phys Conf Ser 107:193–211.

33. Krogh-Moe J (1956) A method for converting experimental x-ray intensities to an absolute scale. Acta Crystallogr 9:951–953. doi: 10.1107/S0365110X56002655

34. Benmore CJ, Soper AK (1998) The SANDALS Manual : a Guide to Performing Experiments on the Small Angle Neutron Diffractometer for Amorphous and Liquid Samples at ISIS. Version 1.0.

35. Howe MA, McGreevy RL, Zetterström P (1996) CORRECT: A correction program for neutron diffraction data.

36. Juhás P, Davis T, Farrow CL, Billinge SJL (2013) *PDFgetX3* : a rapid and highly automatable program for processing powder diffraction data into total scattering pair distribution functions. J Appl Crystallogr 46:560–566. doi: 10.1107/S0021889813005190

37. Swenson J, Matic A, Karlsson C, Börjesson L, Meneghini C, Howells WS (2001) Random ion distribution model: A structural approach to the mixed-alkali effect in glasses. Phys Rev B. doi: 10.1103/PhysRevB.63.132202

38. Swenson J Matic, A.Gejke, C.Börjesson, L.Howells, WS.Capitan, MJ (1999) Conductivity enhancement in PbI2-AgI-AgPO3 glasses by diffraction experiments and reverse Monte Carlo modeling. Phys Rev B 60:12023–12032.

39. Swenson J Börjesson, L.Howells, WS (1995) Structure of borate glasses from neutron-diffraction experiments. Phys Rev B 52:9310–9319.

40. Swenson J Börjesson, L.Howells, WS (1998) Structure of fast-ion conducting lithium and sodium borate glasses by neutron diffraction and reverse Monte Carlo simulations. Phys Rev B 57:13514–13526.

41. Cormier L, Calas G, Creux S, Gaskell PH, Bouchet-Fabre B, Hannon AC (1999) Environment around strontium in silicate and aluminosilicate glasses. Phys Rev B 59:13517–13520. doi: 10.1103/PhysRevB.59.13517

42. Wright AC (1994) Neutron scattering from vitreous silica. V. The structure of vitreous silica: What have we learned from 60 years of diffraction studies? J Non-Crsyt Solids 179:84–115.

43. Wright AC Leadbetter, AJ (1976) Diffraction studies of glass structure. Phys. Chem. Glas. 17:

44. Guignard M, Cormier L, Montouillout V, Menguy N, Massiot D, Hannon AC (2009) Environment of titanium and aluminum in a magnesium alumino-silicate glass. J Phys Condens Matter 21:375107. doi: 10.1088/0953-8984/21/37/375107

45. Martin RA Salmon, PS.Fischer, HE.Cuello, GJ (2003) Structure of dysprosium and holmium phosphate glasses by the method of isomorphic substitution in neutron diffraction. J Phys Condens Matter 15:8235–8252.

46. Enderby JE, North DM, Egelstaff PA (1966) The partial structure factors of liquid Cu-Sn. Philos Mag 14:961–970. doi: 10.1080/14786436608244767

47. Zeidler A, Salmon PS, Fischer HE, Neuefeind JC, Simonson JM, Lemmel H, Rauch H, Markland TE (2011) Oxygen as a Site Specific Probe of the Structure of Water and Oxide Materials. Phys Rev Lett. doi: 10.1103/PhysRevLett.107.145501

48. Wright AC, Hannon AC, Sinclair RN, Johnson WL, Atzmon M (1984) The neutron diffraction double-null isotopic substitution technique. J Phys F Met Phys 14:L201–L205.

49. Enderby JE, Barnes AC (1990) Liquid semiconductors. Rep Prog Phys 53:85–179.

50. Fuoss PH, Bienenstock A (1981) x-ray anomalous scattering factors - measurements and applications. In: Inn.-Shell x-ray Phys. At. Solids, Plenum. D.J. Fabian, A. Kleinpoppen, L.M. Watson, New-York, pp 875–884

51. Kohara S, Tajiri H, Song CH, Ohara K, Temleitner L, Sugimito K, Fujiwara A, Pusztai L, Usuki T, Hosokawa S, Benino Y, Kitamura N, Fukumi K (2014) Anomalous x-ray scattering studies of functional disordered materials. J Phys Conf Ser 502:12014. doi: 10.1088/1742-6596/502/1/012014

52. Schlenz H Kirfel, A.Schulmeister, K.Wartner, N.Mader, W.Raberg, W.Wandelt, K.Oligschleger, C.Bender, S.Franke, R.Hormes, J.Hoffbauer, W.Lansmann, V.Jansen, M.zotov, N.Marian, C.Putz, H.Neuefeind, J (2001) Structure analyses of Ba-silicate glasses. J Non-Cryst Solids 297:37–54.

53. Wright AC, Cole JM, Newport RJ, Fisher CE, Clarke SJ, Sinclair RN, Fischer HE, Cuello GJ (2007) The neutron diffraction anomalous dispersion technique and its application to vitreous Sm2O3·4P2O5. Nucl Instrum Methods Phys Res Sect Accel Spectrometers Detect Assoc Equip 571:622–635. doi: 10.1016/j.nima.2006.11.045

54. Hosokawa S, Oh I, Sakurai M, Pilgrim W-C, Boudet N, Bérar J-F, Kohara S (2011) Anomalous x-ray scattering study of Gex Se1−x glassy alloys across the stiffness transition composition. Phys Rev B. doi: 10.1103/PhysRevB.84.014201

55. Poole PH McMillan, PF.Wolf, GH (1995) Computer simulations of silicate melts. Struct. Dyn. Prop. Silic. Melts 32:

56. Jahn S, Kowalski PM (2014) Theoretical Approaches to Structure and Spectroscopy of Earth Materials. Rev Mineral Geochem 78:691–743. doi: 10.2138/rmg.2014.78.17

57. Vollmayr K Kob, W.Binder, K (1996) Cooling-rate in amorphous silica: a computer-simulation study. Phys Rev B 54:15808–15827.

58. Schiff VK (1990) Computation simulation of ionic liquid transition into vitreous state by the Monte Carlo method. J Non-Cryst Solids 123:36–41.

59. Wright AC (1993) The comparison of molecular dynamics simulations with diffraction experiments. J Non-Cryst Solids 159:264–268.

60. McGreevy RL (1995) RMC - Progress, problems and prospects. Nucl Inst Meth Phys Res A 354:1–16.

61. Mc Greevy RL Zetterström, P (2001) Reverse Monte Carlo modelling of network glasses: useful or useless ? J Non-Cryst Solids 293–295:297–303.

62. Guignard M Cormier, L (2008) Environments of Mg and Al in MgO-Al2O3-SiO2 glasses: a study coupling neutron and x-ray diffraction and Reverse Monte Carlo modeling. Chem Geol 256:111–118.

63. Cormier L, Cuello GJ (2011) Mg coordination in a MgSiO3 glass using neutron diffraction coupled with isotopic substitution. Phys Rev B 83:224204. doi: 10.1103/PhysRevB.83.224204

64. Gereben O, Jovari P, Temleitner L, Pustzai LT (2007) A new version of the RMC++ Reverse Monte Carlo programme, aimed at investigating the structure of covalent glasses. J Optoelectron Adv Mater 9:3021–3027.

65. Gereben O, Pusztai L (2012) RMC_POT: A computer code for reverse monte carlo modeling the structure of disordered systems containing molecules of arbitrary complexity. J Comput Chem 33:2285–2291. doi: 10.1002/jcc.23058

66. Dove MT, Tucker MG, Keen DA (2002) Neutron total scattering method: simultaneous determination of long-range and short-range order in disordered materials. Eur J Mineral 14:331–348. doi: 10.1127/0935-1221/2002/0014-0331

67. Delaye J-M Cormier, L.Ghaleb, D.Calas, G (2001) Investigation of multicomponent silicate glasses by coupling WAXS and molecular dynamics. J Non-Cryst Solids 293–295:290–296.

68. Cormier L Ghaleb, D.Neuville, DR.Delaye, JM.Calas, G (2003) Chemical dependence of network topology of calcium aluminosilicate glasses: a Molecular Dynamics and Reverse Monte Carlo study. J Non-Cryst Solids 332:255–270.

69. Miracle D (2004) A structural model for metallic glasses. Nat Mater 3:697–702.

70. Sheng HW Luo, WK.Alamgir, FM.Bai, JM.Ma, E (2006) Atomic packing and short-to-medium-range order in metallic glasses. Nature 439:

71. Hwang J, Melgarejo ZH, Kalay YE, Kalay I, Kramer MJ, Stone DS, Voyles PM (2012) Nanoscale Structure and Structural Relaxation in Zr50Cu45Al5 Bulk Metallic Glass. Phys Rev Lett 108:195505.

72. Soper AK (2005) Partial structure factors from disordered materials diffraction data: an approach using empirical potential structure refinement. Phys Rev B 72:104204.

73. Finney JL, Hallbrucker A, Kohl I, Soper AK, Bowron DT (2002) Structures of High and Low Density Amorphous Ice by Neutron Diffraction. Phys Rev Lett. doi: 10.1103/PhysRevLett.88.225503

74. Zeidler A, Salmon PS (2016) Pressure-driven transformation of the ordering in amorphous network-forming materials. Phys Rev B. doi: 10.1103/PhysRevB.93.214204

75. Shatnawi MTM (2016) The First Sharp Diffraction Peak in the Total Structure Function of Amorphous Chalcogenide Glasses: Anomalous Characteristics and Controversial Views. New J Glass Ceram 6:37–46. doi: 10.4236/njgc.2016.63005

76. Guthrie M, Tulk CA, Benmore CJ, Xu J, Yarger JL, Klug DD, Tse JS, Mao H, Hemley RJ (2004) Formation and Structure of a Dense Octahedral Glass. Phys Rev Lett. doi: 10.1103/PhysRevLett.93.115502

77. Tanaka K (1988) Pressure dependence of the first sharp diffraction peak in chalcogenide and oxide glasses. Phil Mag Lett 57:183–187.

78. Tsutsu H Tamura, K.Endo, H (1984) Photodarkening in glassy As2S3 under pressure. Solid State Commun 52:877–879.

79. Lou HB, Fang YK, Zeng QS, Lu YH, Wang XD, Cao QP, Yang K, Yu XH, Zheng L, Zhao YD, Chu WS, Hu TD, Wu ZY, Ahuja R, Jiang JZ (2012) Pressure-induced amorphous-to-amorphous configuration change in Ca-Al metallic glasses. Sci Rep 2:376. doi: 10.1038/srep00376

80. Susman S Volin, KJ.Montague, DG.Price, DL (1991) Temperature dependence of the first sharp diffraction peak in vitreous silica. Phys Rev B 43:11076–11081.

81. Busse LE (1984) Temperature dependence of the structure of As2Se3 and AsxS1-x glasses near the glass transition. Phys Rev B 29:3639–3651.

82. Busse LE Nagel, SR (1981) Temperature dependence of the structure factor of As2Se3 glass up to the glass transition. Phys Rev Lett 47:1848–1851.

83. Majérus O Cormier, L.Calas, G.Beuneu, B (2004) A neutron diffraction study of temperature-induced structural changes in potassium disilicate glass and melt. Chem Geol 213:89–102.

84. Duarte MJ, Bruna P, Pineda E, Crespo D, Garbarino G, Verbeni R, Zhao K, Wang WH, Romero AH, Serrano J (2011) Polyamorphic transitions in Ce-based metallic glasses by synchrotron radiation. Phys Rev B 84:224116.

85. Kang J, Zhu J, Wei S-H, Schwegler E, Kim Y-H (2012) Persistent Medium-Range Order and Anomalous Liquid Properties of Al1-xCux Alloys. Phys Rev Lett 108:115901.

86. Li G, Wang YY, Liaw PK, Li YC, Liu RP (2012) Electronic Structure Inheritance and Pressure-Induced Polyamorphism in Lanthanide-Based Metallic Glasses. Phys Rev Lett 109:125501.

87. Misawa M Price, DL.Suzuki, K (1980) The short range order structure of alkali disilicate glasses by pulsed neutron total scattering. J Non-Cryst Solids 37:85–97.

88. Hannon AC Di Martino, D.Santos, LF.Almeida, RM (2007) Ge-O coordination in cesium germanate glasses. J Phys Chem B 111:3324–354.

89. Bychkov E Benmore, CJ.Price, DL (2005) Compositional changes of the first sharp diffraction peak in binary selenide glasses. Phys Rev B 72:172107.

90. Chechetkina EA (1995) Is there a relation between glass-forming ability and first sharp diffraction peak. J Phys Condens Matter 7:3099–3114.

91. Du J Corrales, LR (2006) Compositional dependence of the first sharp diffraction peaks in alkali silicate glasses: a molecular dynamics study. J Non-Cryst Solids 352:3255–3269.

92. Shatnawi MTM, Farrow CL, Chen P, Boolchand P, Sartbaeva A, Thorpe MF, Billinge SJL (2008) Search for a structural response to the intermediate phase in GexSe1−x glasses. Phys Rev B. doi: 10.1103/PhysRevB.77.094134

93. Wilson M Salmon, PS (2009) Network topology and the fragility of tetrahedral glass-forming liquids. Phys Rev Lett 103:157801.

94. Petri I, Salmon PS, Fischer HE (2000) Defects in a Disordered World: The Structure of Glassy GeSe2. Phys Rev Lett 84:2413–2416. doi: 10.1103/PhysRevLett.84.2413

95. Penfold IT Salmon, PS (1991) Structure of covalently bonded glass-forming melts: a full partial-structure-factor analysis of liquid GeSe2. Phys Rev Lett 67:97–101.

96. Soper AK (2010) Network structure and concentration fluctuations in a series of elemental, binary, and tertiary liquids and glasses. J Phys Condens Matter 22:404210.

97. Price DL Moss, SC.Reijers, R.Saboungi, ML.Susman, S (1988) Intermediate-range order in glasses and liquids. J Phys C Solid State Phys 21:L1069–L1072.

98. Elliott SR (1992) The origin of the first sharp peak in the structure factor of covalent glasses and liquids. J PhysCond Matter 4:7661–7678.

99. Chechetkina EA (1994) Medium-range order in amorphous substances: a modified layer model. Solid Stat Comm 91:101–104.

100. Gaskell PH Wallis, DJ (1996) Medium range order in silica, the canonical network glass. Phys Rev Lett 76:66–69.

101. Phillips JC (1981) Topology of caovalent non-crystalline solids II. MRO in chalcogenide alloys and a-Si(Ge). J Non-Cryst Solids 43:37–77.

102. Phillips JC Arnold Beevers, C.Gould, SEB (1980) Molecular structure of As2Se3glass. Phys Rev B 21:5274–5731.

103. Cervinka L (1987) Medium range ordering in non-crystalline solids. J Non-Cryst Solids 90:371–382.

104. Uchino T Harrop, JD.Taraskin, SN.Elliott, SR (2005) Real and reciprocal space structural correlations contributing to the first sharp diffraction peak in silica glass. Phys Rev B 71:14202-1–5.

105. Le Bail A (1995) Modelling the silica glass structure by the Rietveld method. J Non-Cryst Solids 183:39–42. doi: 10.1016/0022-3093(94)00664-4

106. Wilson M Madden, PA (1994) “Prepeaks” and “first sharp diffraction peaks” in computer simulations of strong and fragile ionic liquids. Phys Rev Lett 72:3033–3036.

107. Fayos R Bermejo, FJ.Dawidowski, J.Fischer, HE.González, MA (1996) Direct experimental evidence of the relationship between intermediate-range order in topologically disordered matter and discernible features in the static structure factor. Phys Rev Lett 77:3823–3826.

108. Gaskell PH (2000) Relationships between the medium-range structure of glasses and crystals. Min Mag 64:425–434.

109. Misawa M (1990) Structure factor of X4 tetrahedral molecular liquids: compettiomn between intramolecular and intermolecular atomic spacings. J Chem Phys 93:6774–6778.

110. Dixmier J (1992) Hole generation of prepeaks in diffraction patterns of glasses. J Phys I 2:1011–1027. doi: 10.1051/jp1:1992188

111. Elliott SR (1995) Second sharp diffraction peak in the structure factor of binary covalent network glasses. Phys Rev B 51:8599–8601.

112. Blétry J (1990) Sphere and distance models for binary disordered systems. Philos Mag Part B 62:469–508. doi: 10.1080/13642819008215248

113. Elliott SR (1991) Origin of the first sharp diffraction peak in the structure factor of covalent glasses. Phys Rev Lett 67:711–714.

114. Veprek S Beyeler, HU (1981) On the interpretation of the first, sharp maximum in the x-ray scattering of non-crystalline solids and liquids. Phil Mag 44:557–567.

115. Elliott SR (1991) Medium-range structural order in covalent amorphous solids. Nature 354:445–452.

116. Guinier A (1994) x-ray Diffraction in Crystals, Imperfect Crystals, and Amorphous Bodies. Dover Publications, New York

117. Ehrenfest P (2015) On interference phenomena to be expected when Röntgen rays pass through a di-atomic gas. Proc R Acad Sci Amst 17:1184–1190.

118. Yavari AR, Moulec AL, Inoue A, Nishiyama N, Lupu N, Matsubara E, Botta WJ, Vaughan G, Michiel MD, Kvick Å (2005) Excess free volume in metallic glasses measured by x-ray diffraction. Acta Mater 53:1611–1619. doi: 10.1016/j.actamat.2004.12.011

119. Ma D, Stoica AD, Wang X-L (2009) Power-law scaling and fractal nature of medium-range order in metallic glasses. Nat Mater 8:30–34. doi: 10.1038/nmat2340

120. Hannon AC Grimley, DI.Hulme, RA.Wright, AC.Sinclair, RN (1994) Boroxol groups in vitreous boron oxide: new evidence from neutron diffraction and inelastic neutron scattering studies. J Non-Cryst Solids 177:299–316.

121. Misawa M (1990) Structure of vitreous and molten B2O3 measured by pulsed neutron total scattering. J Non-Cryst Solids 122:33–40.

122. Swenson J, Matic A, Gejke C, Börjesson L, Howells WS, Capitan MJ (1999) Conductivity enhancement in PbI2−AgI−AgPO3 glasses by diffraction experiments and reverse Monte Carlo modeling. Phys Rev B 60:12023–12032. doi: 10.1103/PhysRevB.60.12023

123. Salmon PS, Petri I (2003) Structure of glassy and liquid GeSe2. J Phys Condens Matter 15:S1509.

124. Benmore CJ, Salmon PS (1994) Structure of Fast Ion Conducting and Semiconducting Glassy Chalcogenide Alloys. Phys Rev Lett 73:264–267. doi: 10.1103/PhysRevLett.73.264

125. Liu J, Salmon PS (1997) Structural ordering in Ag-based ternary chalcogenide glasses. EPL Europhys Lett 39:521.

126. Salmon PS Xin, S (2002) Chalcogenide glasses: the effect of covalent versus ionic bonding in (CuI)0.6(Sb2Se3)0.4. Phys Rev B 65:64202-1-64202–4.

127. Lee JH, Pradel A, Taillades G, Ribes M, Elliott SR (1997) Structural studies of glassy (Li2S)0.5(SiS2)0.5 by isotopic-substitution neutron diffraction. Phys Rev B 56:10934–10941. doi: 10.1103/PhysRevB.56.10934

128. Cormier L, Creux S, Galoisy L, Calas G, Gaskell PH (1996) Mediun range order around cations in silicate glasses. Chem Geol 128:77–91.

129. Cormier L Gaskell, PH.Calas, G.Soper, AK (1998) Medium range order around titanium in a silicate glass studied by neutron diffraction with isotopic substitution. Phys Rev B 58:11322–11330.

130. Farges F Brown, Jr .GE.Navrotsky, A.Gan, H.Rehr, JJ (1996) Coordination chemistry of Ti(IV) in silicate glasses and melts. II. Glasses at ambient temperature and pressure. Geochim Cosmochim Acta 60:3039–3053.

131. Cormier L, Calas G, Gaskell PH (2001) Cationic environment in silicate glasses studied by neutron diffraction with isotopic substitution. Chem Geol 174:349–363. doi: 10.1016/S0009-2541(00)00325-9

132. Gaskell PH Zhao; Z.Calas, G.Galoisy, L (1992) The structure of mixed cation oxide glasses. In: Pye LD LaCourse, WC.Stevens, HJ (ed) Phys. Non-Cryst. Solids. Taylor & Francis, London, pp 53–58

133. Cormier L, Gaskell PH, Calas G, Zhao J, Soper AK (1998) Environment around Li in the LiAlSiO 4 ionic conductor glass: A neutron-scattering and reverse Monte Carlo study. Phys Rev B 57:R8067–R8070. doi: 10.1103/PhysRevB.57.R8067

134. Zhao J Gaskell, PH.Cluckie, MM.Soper, AK (1998) A neutron diffraction, isotopic substitution study of the structure of Li2O.2SiO2 glass. J Non-Cryst Solids 234:721–727.

135. Uhlig H Hoffmann, MJ.Lamparter, HP.Aldinger, F.Bellissent, R.Steeb, S (1996) Short-range order and medium-range order in lithium silicate glasses, Part I: Diffraction experiments and results. J Amer Ceram Soc 79:2833–2838.

136. Eckersley MC Gaskell, PH.Barnes, AC.Chieux, P (1988) Structural ordering in a calcium silicate glass. Nature 335:525–527.

137. Creux S Bouchet-Fabre, B.Gaskell, PH (1995) Anomalous wide angle x-ray scattering study of strontium silicate and aluminosilicate glasses. J Non-Cryst Solids 192 & 193:360–363.

138. Gaskell PH, Eckersley MC, Barnes AC, Chieux P (1991) Medium-Range Order in the Cation Distribution of a Calcium Silicate Glass. Nature 350:675–677.

139. Cormier L Galoisy, L.Delaye, JM.Ghaleb, D.Calas, G (2001) Short- and medium-range structural order around cations in glasses: a multidisciplinary approach. CR Acad Sci Sér IV 2:249–262.

140. Warren BE, Pincus AG (1940) Atomic consideration of immiscibility in glass system. J Am Ceram Soc 23:301–304. doi: 10.1111/j.1151-2916.1940.tb14194.x

141. Greaves GN Sen, S (2007) Inorganic glasses, glass-forming liquids and amorphizing solids. Adv Phys 56:1–166.

142. Greaves GN (1989) EXAFS, glass structure and diffusion. Phil Mag B 60:793–800.

143. Block S Piermarini, GJ (1964) Alkaline earth cation distribution in vitreous borates. Phys Chem Glas 5:138–144.

144. Yasui I Hasegawa, H.Suito, Y (1988) Structure of borate glasses containing Tl and Ba oxide. J Non-Cryst Solids 106:30–33.

145. Yasui I Hasegawa, H.Saito, Y.Akasaka, Y (1990) Structure of borate glasses containing heavy metal ions. J Non-Cryst Solids 123:71–74.

146. Brosset C (1963) x-ray investigation of the distribution of heavy atoms in glass. Phys Chem Glas 4:99–102.

147. Hanson CD Egami, T (1986) Distribution of Cs+ ions in single and mixed alkali silicate glasses from energy dispersive x-ray diffraction. J Non-Cryst Solids 87:171–184.

148. Krogh-Moe J (1962) An x-ray study of barium borate glasses. Phys Chem Glas 3:208–212.

149. Abramo MC Caccamo, C.Pizzimenti, G (1992) Structural properties and medium-range order in calcium-metasilicate (CaSiO3) glass: a molecular dynamics study. J Chem Phys 96:9083–9091.

150. Cormier L Calas, G.Gaskell, PH (1997) A reverse Monte Carlo study of a titanosilicate glass. J Phys Cond Mat 9:10129–10136.

151. Cormier L Calas, G.Creux, S.Gaskell, PH.Bouchet-Fabre, B.Hannon, AC (1999) Environment around strontium in silicate and aluminosilicate glasses. Phys Rev B 59:13517–13520.

152. Waseda Y Suito, H (1977) The structure of molten alkali metal silicates. Trans ISIJ 17:82–91.

153. Waseda Y (1980) The structure of non-crystalline materials. Mc Graw-Hill, New York

154. Hennet L, Cristiglio V, Kozaily J, Pozdnyakova I, Fischer HE, Bytchkov A, Drewitt JWE, Leydier M, Thiaudière D, Gruner S, Brassamin S, Zanghi D, Cuello GJ, Koza M, Magazù S, Greaves GN, Price DL (2011) Aerodynamic levitation and laser heating:: Applications at synchrotron and neutron sources. Eur Phys J Spec Top 196:151–165. doi: 10.1140/epjst/e2011-01425-0

155. Jacobs G, Egry I, Maier K, Platzek D, Reske J, Frahm R (1996) Extended x-ray-absorption fine structure studies of levitated undercooled metallic melts. Rev Sci Instrum 67:3683. doi: 10.1063/1.1146855

156. Paradis P-F, Ishikawa T, Yu J, Yoda S (2001) Hybrid electrostatic–aerodynamic levitation furnace for the high-temperature processing of oxide materials on the ground. Rev Sci Instrum 72:2811. doi: 10.1063/1.1368860

157. Trinh EH (1985) Compact acoustic levitation device for studies in fluid dynamics and material science in the laboratory and microgravity. Rev Sci Instrum 56:2059. doi: 10.1063/1.1138419

158. Haumesser PH, Garandet JP, Brancillon J, Daniel M, Campbell I, Jackson P (2002) High Temperature Viscosity Measurements by the Gas Film Levitation Technique: Application to Various Types of Materials. Int J Termophys 23:1217–1228.

159. Landron C, Hennet L, Coutures JP, Gailhanou M, Gramond M, Berar JF (1998) Contactless investigation on laser-heated oxides by synchrotron radiation. Europhys Lett EPL 44:429–435. doi: 10.1209/epl/i1998-00490-0

160. Landron C Hennet, L.Jenkins, TE.Greaves, GN.Coutures, JP.Soper, AK (2001) Liquid alumina: detailed atomic coordination determined from neutron diffraction data using empirical potential structure refinement. Phys Rev Lett 86:4839–4842.

161. Price DL (2010) High-temperature levitated materials. Cambridge Univ. Press, Cambridge

162. Susman S Volin, KJ.Montague, DG.Price, DL (1991) Temperature dependence of the first sharp diffraction peak in vitreous silica. Phys Rev B 43:11076–11081.

163. Skinner LB, Benmore CJ, Weber JKR, Wilding MC, Tumber SK, Parise JB (2013) A time resolved high energy x-ray diffraction study of cooling liquid SiO2. Phys Chem Chem Phys 15:8566–8572. doi: 10.1039/C3CP44347G

164. Cormier L, Calas G, Beuneu B (2011) Structural changes between soda-lime silicate glass and melt. J Non-Cryst Solids 357:926–931. doi: 10.1016/j.jnoncrysol.2010.10.014

165. Ansell S Krishnan, S.Weber, JK.Felten, JF.Nordine, PC.Beno, MA.Price, DL.Saboungi, ML (1997) Structure of liquid aluminium oxide. Phys Rev Lett 78:464–466.

166. Drewitt JWE, Jahn S, Cristiglio V, Bytchkov A, Leydier M, Brassamin S, Fischer HE, Hennet L (2011) The structure of liquid calcium aluminates as investigated using neutron and high energy x-ray diffraction in combination with molecular dynamics simulation methods. J Phys Condens Matter 23:155101.

167. Cristiglio V, Cuello GJ, Hennet L, Pozdnyakova I, Leydier M, Kozaily J, Fischer HE, Johnson MR, Price DL (2010) Neutron diffraction study of molten calcium aluminates. J Non-Cryst Solids 356:2492–2496. doi: 10.1016/j.jnoncrysol.2010.03.027

168. Mei Q, Benmore CJ, Weber JKR, Wilding M, Kim J, Rix J (2008) Diffraction study of calcium aluminate glasses and melts: II. High energy x-ray diffraction on melts. J Phys Condens Matter 20:245107. doi: 10.1088/0953-8984/20/24/245107

169. Bytchkov A (2006) Structure et dynamique d'aluminates fondus et de verres Phosphore - Sélénium. Complémentarité de la résonance magnétique nucléaire et de la diffusion des rayons X et des neutrons. PhD Thesis, Orléans

170. Wilding MC, Wilson M, Benmore CJ, Weber JKR, McMillan PF (2013) Structural changes in supercooled Al2O3–Y2O3 liquids. Phys Chem Chem Phys 15:8589. doi: 10.1039/c3cp51209f

171. Wilding MC, McMillan PF (2002) Liquid polymorphism in yttrium-aluminate liquids. In: New Kinds Phase Transit. Transform. Disord. Subst., Kluwer Academic Publishers. V. V. Brazhkin, S. V. Buldyrev, V. N. Rhzhov and H. E. Stanley, Dordrecht, Boston, pp 57–73

172. Wilding MC Wilson, M.McMillan, PF (2006) Structural studies and polyamorphism in amorphous solids and liquids at high pressure. Chem Soc Rev 35:964–986.

173. Hennet L, Thiaudière D, Landron C, Melin P, Price DL, Coutures J-P, Bérar J-F, Saboungi M-L (2003) Melting behavior of levitated Y2O3. Appl Phys Lett 83:3305. doi: 10.1063/1.1621090

174. Sakowski J Herms, G (2001) The structure of vitreous and molten B2O3. J Non-Cryst Solids 293–295:304–311.

175. Majérus O Cormier, L.Calas, G.Beuneu, B (2003) Temperature-induced boron coordination change in alkali borate glasses and melts. Phys Rev B 67:24210-1-24210–7.

176. Cormier L Majérus, O.Neuville, DR.Calas, G (2006) Temperature-induced structural modifications between alkali borate glasses and melts. J Am Ceram Soc 89:13–19.

177. Majérus O Cormier, L.Calas, G.Beuneu, B (2003) Modification of the structural role of lithium between lithium-diborate glasses and melts: implications for transport properties and melt fragility. J Phys Chem B 107:13044–13050.

178. Tucker MG Dove, MT.Keen, DA (2000) Direct measurement of the thermal expansion of the SiO2 bond by neutron total scattering. J Phys Condens Matter 12:L425–L430.

179. Mei Q Benmore, CJ.Weber, JKR (2007) Structure of liquid SiO2: a measurment by high-energy x-ray diffraction. Phys Rev Lett 98:57802.

180. Wilding MC, Benmore CJ, Weber JKR (2010) Changes in the local environment surrounding magnesium ions in fragile MgO-SiO2 liquids. Eur Lett 89:26005. doi: 10.1209/0295-5075/89/26005

181. Drewitt JWE, Sanloup C, Bytchkov A, Brassamin S, Hennet L (2013) Structure of (FexCa1-xO)y(SiO2)1-y liquids and glasses from high-energy x-ray diffraction: Implications for the structure of natural basaltic magmas. Phys Rev B 87:224201. doi: 10.1103/PhysRevB.87.224201

182. Benmore CJ, Weber JKR, Wilding MC, Du J, Parise JB (2010) Temperature-dependent structural heterogeneity in calcium silicate liquids. Phys Rev B 82:224202. doi: 10.1103/PhysRevB.82.224202

183. Skinner LB, Benmore CJ, Weber JKR, Tumber S, Lazareva L, Neuefeind J, Santodonato L, Du J, Parise JB (2012) Structure of Molten CaSiO3: Neutron Diffraction Isotope Substitution with Aerodynamic Levitation and Molecular Dynamics Study. J Phys Chem B 116:13439–13447. doi: 10.1021/jp3066019

184. Schenk T, Holland-Moritz D, Simonet V, Bellissent R, Herlach DM (2002) Icosahedral Short-Range Order in Deeply Undercooled Metallic Melts. Phys Rev Lett. doi: 10.1103/PhysRevLett.89.075507

185. Holland-Moritz D, Stüber S, Hartmann H, Unruh T, Hansen T, Meyer A (2009) Structure and dynamics of liquid Ni36Zr64 studied by neutron scattering. Phys Rev B. doi: 10.1103/PhysRevB.79.064204

186. Gruner S, Marczinke J, Hennet L, Hoyer W, Cuello GJ (2009) On the atomic structure of liquid Ni–Si alloys: a neutron diffraction study. J Phys Condens Matter 21:385403. doi: 10.1088/0953-8984/21/38/385403

187. Georgarakis K, Hennet L, Evangelakis GA, Antonowicz J, Bokas GB, Honkimaki V, Bytchkov A, Chen MW, Yavari AR (2015) Probing the structure of a liquid metal during vitrification. Acta Mater 87:174–186. doi: 10.1016/j.actamat.2015.01.005

188. Kelton KF, Lee GW, Gangopadhyay AK, Hyers RW, Rathz TJ, Rogers JR, Robinson MB, Robinson DS (2003) First x-ray Scattering Studies on Electrostatically Levitated Metallic Liquids: Demonstrated Influence of Local Icosahedral Order on the Nucleation Barrier. Phys Rev Lett 90:195504.

189. Akola J, Jones RO, Kohara S, Usuki T, Bychkov E (2010) Density variations in liquid tellurium: Roles of rings, chains, and cavities. Phys Rev B. doi: 10.1103/PhysRevB.81.094202

190. Le Coq D, Bytchkov A, Honkimäki V, Beuneu B, Bychkov E (2008) Neutron and x-ray diffraction studies of TeCl4 and TeBr4 liquids. J Non-Cryst Solids 354:259–262. doi: 10.1016/j.jnoncrysol.2007.07.099

191. Le Coq D, Beuneu B, Bychkov E, Tokuyama M, Oppenheim I, Nishiyama H (2008) Structure of Te1−xClx Liquids. AIP, pp 712–716

192. Magallanes-Perdomo M, Pena P, De Aza PN, Carrodeguas RG, Rodríguez MA, Turrillas X, De Aza S, De Aza AH (2009) Devitrification studies of wollastonite–tricalcium phosphate eutectic glass. Acta Biomater 5:3057–3066. doi: 10.1016/j.actbio.2009.04.026

193. Piarristeguy AA, Cuello GJ, Yot PG, Ribes M, Pradel A (2008) Neutron thermodiffraction study of the crystallization of Ag–Ge–Se glasses: evidence of a new phase. J Phys Condens Matter 20:155106.

194. Soignard E, McMillan PF (2004) An Introduction to Diamond Anvil Cells and Loading Techniques. In: Katrusiak A, McMillan P (eds) High-Press. Crystallogr. Springer Netherlands, Dordrecht, pp 81–100

195. Klotz S (2013) Techniques in high pressure neutron scattering. CRC Press, Boca Raton, Fla.

196. Rey N (2006) Matériaux carbonés sp2/sp3 intercalés sous pression : le cas du graphite et des clathrates. PhD Thesis, Claude Bernard

197. Klotz S (2014) Neutron diffraction studies on “simple” iron oxides under pressure: Fe3O4, α-Fe2O3, and FeO. Chin Sci Bull 59:5241–5250. doi: 10.1007/s11434-014-0587-9

198. Besson JM, Hamel G, Grima T, Nelmes RJ, Loveday JS, Hull S, Häusermann D (1992) A large volume pressure cell for high temperatures. High Press Res 8:625–630. doi: 10.1080/08957959208206312

199. Mezouar M, Faure P, Crichton W, Rambert N, Sitaud B, Bauchau S, Blattmann G (2002) Multichannel collimator for structural investigation of liquids and amorphous materials at high pressures and temperatures. Rev Sci Instrum 73:3570. doi: 10.1063/1.1505104

200. Binns J, Kamenev KV, McIntyre GJ, Moggach SA, Parsons S (2016) Use of a miniature diamond-anvil cell in high-pressure single-crystal neutron Laue diffraction. IUCrJ 3:168–179.

201. McMillan PF Wilson, M.Wilding, MC.Daisenberger, D.Mezouar, M.Greaves, GN (2007) Polyamorphism and liquid-liquid phase transitions: challenges for experiment and theory. J Phys Condens Matter 19:415101.

202. Poole PH, Grande T, Angell CA, McMillan PF (1997) Polymorphic phase transitions in liquids and glasses. Science 275:322–323. doi: 10.1126/science.275.5298.322

203. Soper AK, Ricci MA (2000) Structures of High-Density and Low-Density Water. Phys Rev Lett 84:2881–2884. doi: 10.1103/PhysRevLett.84.2881

204. Guthrie M, Tulk CA, Benmore CJ, Klug DD (2004) A structural study of very high-density amorphous ice. Chem Phys Lett 397:335–339. doi: 10.1016/j.cplett.2004.07.116

205. Finney JL, Bowron DT, Soper AK, Loerting T, Mayer E, Hallbrucker A (2002) Structure of a New Dense Amorphous Ice. Phys Rev Lett. doi: 10.1103/PhysRevLett.89.205503

206. Klotz S, Hamel G, Loveday JS, Nelmes RJ, Guthrie M, Soper AK (2002) Structure of High-Density Amorphous Ice under Pressure. Phys Rev Lett. doi: 10.1103/PhysRevLett.89.285502

207. Klotz S, Strässle T, Saitta AM, Rousse G, Hamel G, Nelmes RJ, Loveday JS, Guthrie M (2005) In situ neutron diffraction studies of high density amorphous ice under pressure. J Phys Condens Matter 17:S967.

208. Tulk CA (2002) Structural Studies of Several Distinct Metastable Forms of Amorphous Ice. Science 297:1320–1323. doi: 10.1126/science.1074178

209. Guthrie M, Urquidi J, Tulk CA, Benmore CJ, Klug DD, Neuefeind J (2003) Direct structural measurements of relaxation processes during transformations in amorphous ice. Phys Rev B. doi: 10.1103/PhysRevB.68.184110

210. Sun Z, Sun G, Chen Y, Xu L (2014) Liquid-liquid phase transition in water. Sci China Phys Mech Astron 57:810–818. doi: 10.1007/s11433-014-5451-z

211. Brazhkin VV, Katayama Y, Trachenko K, Tsiok OB, Lyapin AG, Artacho E, Dove M, Ferlat G, Inamura Y, Saitoh H (2008) Nature of the Structural Transformations in B2O3 Glass under High Pressure. Phys Rev Lett 101:35702.

212. Zeidler A, Wezka K, Whittaker DAJ, Salmon PS, Baroni A, Klotz S, Fischer HE, Wilding MC, Bull CL, Tucker MG, Salanne M, Ferlat G, Micoulaut M (2014) Density-driven structural transformations in B2O3 glass. Phys Rev B. doi: 10.1103/PhysRevB.90.024206

213. Sampath S, Benmore CJ, Lantzky KM, Neuefeind J, Leinenweber K, Price DL, Yarger JL (2003) Intermediate-Range Order in Permanently Densified GeO2 Glass. Phys Rev Lett. doi: 10.1103/PhysRevLett.90.115502

214. Sugai S, Onodera A (1996) Medium-Range Order in Permanently Densified SiO2 and GeO2 Glass. Phys Rev Lett 77:4210–4213. doi: 10.1103/PhysRevLett.77.4210

215. Inamura Y Arai, M.Nakamura, M.Otomo, T.Kitamura, N.Bennington, SM.Hannon, AC.Buchenau, U (2001) Intermediate range structure and low-energy dynamics of densified vitreous silica. J Non-Cryst Solids 293–295:389–393.

216. Itié JP Polian, Calas, G.Petiau, J.Fontaine, A.Tolentino, H (1989) Pressure-induced coordination changes in crystalline and vitreous GeO2. Phys Rev Lett 63:398–401.

217. Meade C Hemley, RJ.Mao, HK (1992) High-pressure x-ray diffraction of SiO2 glass. Phys Rev Lett 69:1387–1390.

218. Sato T, Funamori N (2008) Sixfold-Coordinated Amorphous Polymorph of SiO2 under High Pressure. Phys Rev Lett. doi: 10.1103/PhysRevLett.101.255502

219. Brazhkin VV (2009) Comments on “Sixfold-coordinated amorphous polymorph of SiO2 under high pressure.” Phys Rev Lett 102:209603.

220. Benmore CJ, Soignard E, Amin SA, Guthrie M, Shastri SD, Lee PL, Yarger JL (2010) Structural and topological changes in silica glass at pressure. Phys Rev B. doi: 10.1103/PhysRevB.81.054105

221. Inamura Y Katayama, Y.Utsumi, W.Funakoshi, K (2004) Transformations in the intermediate-range structure of SiO2 glass under high pressure and temperature. Phys Rev Lett 93:15501.

222. Sato T, Funamori N (2010) High-pressure structural transformation of SiO2 glass up to 100 GPa. Phys Rev B 82:184102.

223. Zeidler A, Wezka K, Rowlands RF, Whittaker DAJ, Salmon PS, Polidori A, Drewitt JWE, Klotz S, Fischer HE, Wilding MC, Bull CL, Tucker MG, Wilson M (2014) High-Pressure Transformation of SiO2 Glass from a Tetrahedral to an Octahedral Network: A Joint Approach Using Neutron Diffraction and Molecular Dynamics. Phys Rev Lett. doi: 10.1103/PhysRevLett.113.135501

224. Hong X Shen, G.Prakapenka, VB.Newville, M.Rivers, ML.Sutton, SR (2007) Intermediate states of GeO2 glass under pressures up to 35GPa. Phys Rev B 75:104201.

225. Mei Q, Sinogeikin S, Shen G, Amin S, Benmore CJ, Ding K (2010) High-pressure x-ray diffraction measurements on vitreous GeO 2 under hydrostatic conditions. Phys Rev B. doi: 10.1103/PhysRevB.81.174113

226. Hong X, Ehm L, Duffy TS (2014) Polyhedral units and network connectivity in GeO2 glass at high pressure: An x-ray total scattering investigation. Appl Phys Lett 105:81904. doi: 10.1063/1.4894103

227. Drewitt JWE Salmon, PS.Barnes, AC.Klotz, S.Fischer, HE.Crichton, WA (2010) Structure of GeO2 glass at pressures up to 8.6 GPa. Phys Rev B 81:14202.

228. Salmon PS, Drewitt JWE, Whittaker DAJ, Zeidler A, Wezka K, Bull CL, Tucker MG, Wilding MC, Guthrie M, Marrocchelli D (2012) Density-driven structural transformations in network forming glasses: a high-pressure neutron diffraction study of GeO2 glass up to 17.5 GPa. J Phys Condens Matter 24:415102. doi: 10.1088/0953-8984/24/41/415102

229. Wezka K, Salmon PS, Zeidler A, Whittaker DAJ, Drewitt JWE, Klotz S, Fischer HE, Marrocchelli D (2012) Mechanisms of network collapse in GeO2 glass: high-pressure neutron diffraction with isotope substitution as arbitrator of competing models. J Phys Condens Matter 24:502101.

230. Micoulaut M Cormier, L.Henderson, GS (2006) The structure of amorphous, crystalline and liquid GeO2. J Phys Condens Matter 18:R1–R32.

231. Salmon PS, Zeidler A (2015) Networks under pressure: the development of in situ high-pressure neutron diffraction for glassy and liquid materials. J Phys Condens Matter 27:133201. doi: 10.1088/0953-8984/27/13/133201

232. Zeidler A, Salmon PS, Skinner LB (2014) Packing and the structural transformations in liquid and amorphous oxides from ambient to extreme conditions. Proc Natl Acad Sci 111:10045–10048. doi: 10.1073/pnas.1405660111

233. Wang Y, Sakamaki T, Skinner LB, Jing Z, Yu T, Kono Y, Park C, Shen G, Rivers ML, Sutton SR (2014) Atomistic insight into viscosity and density of silicate melts under pressure. Nat Commun 5:3241. doi: 10.1038/ncomms4241

234. Mei Q Benmore, CJ.Hart, RT.Bychkov, E.Salmon, PS.Martin, CD.Michel, FM.Antao, SM.Chupas, PJ.Lee, P..Shastri, SD.Parise, SD.Leinenweber, K.Amin, S.Yarger, JL (2006) Topological changes in glassy GeSe2 at pressures up to 9.3 GPa dtermined by high-energy x-ray and neutron diffraction measurements. Phys Rev B 74:14203.

235. Wezka K, Bouzid A, Pizzey KJ, Salmon PS, Zeidler A, Klotz S, Fischer HE, Bull CL, Tucker MG, Boero M, Le Roux S, Tugène C, Massobrio C (2014) Density-driven defect-mediated network collapse of GeSe2 glass. Phys Rev B. doi: 10.1103/PhysRevB.90.054206

236. Zeidler A Drewitt, JWE.Salmon, PS.Barnes, AC.Crichton, WA.Klotz, S.Fischer, HE.Benmore, CJ.Ramos, S.Hannon, AC (2009) Establishing the structure of GeS2 at high pressures and temperatures: a combined approach using x-ray and neutron diffraction. J Phys C Condens Matter 21:474217.

237. Crichton WA, Mezouar M, Grande T, Stølen S, Grzechnik A (2001) Breakdown of intermediate-range order in liquid GeSe2 at high pressure. Nature 414:622–625. doi: 10.1038/414622a

238. Sheng HW, Ma E, Liu HZ, Wen J (2006) Pressure tunes atomic packing in metallic glass. Appl Phys Lett 88:171906–3.

239. Zeng QS, Li YC, Feng CM, Liermann P, Somayazulu M, Shen GY, Mao H -k., Yang R, Liu J, Hu TD, Jiang JZ (2007) Anomalous compression behavior in lanthanum/cerium-based metallic glass under high pressure. PNAS 104:13565–13568. doi: 10.1073/pnas.0705999104

240. Sheng HW, Liu HZ, Cheng YQ, Wen J, Lee PL, Luo WK, Shastri SD, Ma E (2007) Polyamorphism in a metallic glass. Nat Mater 6:192–197. doi: 10.1038/nmat1839

241. Zeng QS, Fang YZ, Lou HB, Gong Y, Wang XD, Yang K, Li AG, Yan S, Lathe C, Wu FM, Yu XH, Jiang JZ (2010) Low-density to high-density transition in $Ce_{75}Al_{23}Si_2$ metallic glass. J Phys Condens Matter 22:375404. doi: 10.1088/0953-8984/22/37/375404

242. Zeng Q, Ding Y, Mao WL, Yang W, Sinogeikin SV, Shu J, Mao H, Jiang JZ (2010) Origin of Pressure-Induced Polyamorphism in Ce 75 Al 25 Metallic Glass. Phys Rev Lett. doi: 10.1103/PhysRevLett.104.105702

243. Cadien A, Hu QY, Meng Y, Cheng YQ, Chen MW, Shu JF, Mao HK, Sheng HW (2013) First-order liquid-liquid phase transition in cerium. Phys Rev Lett 110:125503.